

DRAG ON AN OSCILLATING AIRFOIL IN A  
FLUCTUATING FREE STREAM

A THESIS

Presented to

The Faculty of the Division  
of Graduate Studies

By

Sesi Bhushan Rao Kottapalli

In Partial Fulfillment  
of the Requirements for the Degree  
Doctor of Philosophy  
in the School of Aerospace Engineering

Georgia Institute of Technology

August, 1977

DRAG ON AN OSCILLATING AIRFOIL IN A  
FLUCTUATING FREE STREAM

Approved:

G. Alvin Pierce, Chairman

Louis H. Bangert

Robin B. Gray

Date approved by Chairman: 8-10-77

## ACKNOWLEDGMENTS

I wish to express my appreciation to Dr. G. Alvin Pierce, my teacher and advisor, for his suggestion of the thesis topic and for providing most of the wisdom necessary for the completion of this study. His guidance and assistance throughout my graduate academic career have been invaluable and are sincerely appreciated.

I would also like to thank Drs. Robin B. Gray and Louis H. Bangert, members of the Reading Committee, for their valuable advice and useful suggestions.

Special thanks are extended to my parents for their constant encouragement and support.

Finally, I wish to thank Ms. Pilar Girona for her expeditious typing of the thesis.

## TABLE OF CONTENTS

	Page
ACKNOWLEDGMENTS. . . . .	ii
LIST OF TABLES. . . . .	v
LIST OF ILLUSTRATIONS. . . . .	vi
NOMENCLATURE . . . . .	ix
SUMMARY. . . . .	xv
 Chapter	
I. INTRODUCTION. . . . .	1
II. POTENTIAL FLOW DEVELOPMENT. . . . .	7
Governing Relations	
Boundary Conditions	
Solution Procedure	
Oscillating Flat Plate	
Camber Line at Constant Angle of Attack	
Thickness Distribution at Zero Incidence	
Equations for a Symmetrical Airfoil	
Computational Details	
III. BOUNDARY LAYER ANALYSIS . . . . .	38
General Considerations	
Method of Solution	
Finite Difference Scheme	
Procedural Outline	
Detailed Considerations	
Stagnation Point Profiles	
Details-Laminar Region	
Determination of Transition Point	
Profile at First Turbulent Station	
Details-Turbulent Region	
IV. RESULTS AND DISCUSSION. . . . .	56
Potential Flow	
Comparison with Windsor's Results	
Extension of Present Approach to the case of	
Different Airfoil and Free Stream Frequencies	
Comparison with Greenberg's Analysis	



## TABLE OF CONTENTS (Continued)

Chapter	Page
Laminar Flow Results	
Comparison with Experimental Data	
Effects due to the Amplitude of Free Stream	
Fluctuations	
Reduced Frequency Effects	
Effects due to Phase Difference Between Stream	
Fluctuations and Airfoil Oscillations	
Superposition of Drag	
Reynolds Number Dependency	
Turbulent Flow Results	
Preliminary Discussion	
Reduced Frequency Effects	
Effects due to the Amplitude of Free Stream	
Fluctuations	
Effects due to Phase Difference Between Stream	
Fluctuations and Airfoil Oscillations	
Remarks about Drag Superposition	
Reynolds Number Dependency	
V. CONCLUSIONS AND RECOMMENDATIONS . . . . .	126
Conclusions	
Recommendations	
APPENDIX	
A. FINITE DIFFERENCE REPRESENTATIONS AND	
DIFFERENCE EQUATIONS. . . . .	131
Difference Representations	
Difference Equations	
Continuity Equation	
B. STAGNATION POINT FINITE DIFFERENCE	
EQUATIONS . . . . .	136
REFERENCES . . . . .	138
VITA . . . . .	143

## LIST OF TABLES

Table	Page
1. Lift and Moment Comparisons . . . . .	62
2. Drag Dependency on Reynolds Number . . . . .	125

## LIST OF ILLUSTRATIONS

Figure	Page
1. Definition of Axes. . . . .	9
2. Comparison of Calculated and Measured Pressure Coefficient . . . . .	58
3. Skin Friction Comparison for NACA 0012 Airfoil . . . . .	63
4. Turbulent Skin Friction for a Flat Plate. . . . .	64
5. Turbulent Skin Friction Comparison-Newman Airfoil. . . . .	65
6. Example of a Computed Drag Curve. . . . .	71
7. Comparison of Computed and Measured Drags-I . . . . .	74
8. Comparison of Computed and Measured Drags-II. . . . .	75
9. Comparison of Computed and Measured Drags-III . . . . .	76
10. Variation of Drag with Time, $\alpha = 2^\circ$ , Effect of $\sigma$ . . . . .	78
11a. Variation of Drag with Time, $\alpha = 2^\circ + 2^\circ \cos(\omega t)$ , Effect of $\sigma$ . . . . .	79
11b. Variation of Drag with Time, $\alpha = 2^\circ + 2^\circ \cos(\omega t)$ , $k = 0.00$ , $\sigma = 0.00$ . . . . .	80
12. Variation of Phase, $\phi$ , with $\sigma$ . . . . .	81
13. Variation of Amplitude Ratio, $\left(\frac{A_c}{A_o}\right)$ , with $\sigma$ . . . . .	82
14. Variation of Drag with Time-Effect of Reduced Frequency, $k$ . . . . .	86
15. Variation of Phase, $\phi$ , with Reduced Frequency, $k$ . . . . .	87

## LIST OF ILLUSTRATIONS (Continued)

Figure		Page
16.	Variation of Amplitude Ratio, $\left(\frac{A_c}{A_o}\right)$ , with Reduced Frequency, $k$ . . . . .	88
17.	Variation of Phase, $\phi$ , with Phase Difference, $\psi$ , and Reduced Frequency, $k$ . . . . .	92
18.	Variation of Amplitude Ratio, $\left(\frac{A_c}{A_o}\right)$ , with Phase Difference, $\psi$ , and Reduced Frequency, $k$ . . . . .	93
19.	Variation of Phase, $\phi$ , with Phase Difference, $\psi$ , and $\sigma$ . . . . .	96
20.	Variation of Amplitude Ratio, $\left(\frac{A_c}{A_o}\right)$ , with Phase Difference, $\psi$ , and $\sigma$ . . . . .	97
21.	Variation of Drag with Time, $k = 0.00$ . . . . .	102
22.	Variation of Drag with Time, $k = 0.20$ . . . . .	103
23.	Transition Point Variations-Upper Surface . . . . .	104
24.	Transition Point Variations-Lower Surface . . . . .	105
25.	Variation of Drag with Time, Effect of Reduced Frequency, $k$ . . . . .	107
26.	Variation of Phase, $\phi$ , with Reduced Frequency, $k$ . . . . .	108
27.	Variation of Amplitude Ratio, $\left(\frac{A_c}{A_o}\right)$ , with Reduced Frequency, $k$ . . . . .	109
28.	Variation of Drag with Time, Effect of $\sigma$ . . . . .	112
29.	Variation of Phase, $\phi$ , with $\sigma$ . . . . .	113
30.	Variation of Amplitude Ratio, $\left(\frac{A_c}{A_o}\right)$ , with $\sigma$ . . . . .	114
31.	Variation of Phase, $\phi$ , with Phase Difference, $\psi$ , and Reduced Frequency, $k$ . . . . .	118

## LIST OF ILLUSTRATIONS (Continued)

Figure		Page
32.	Variation of Amplitude Ratio, $\left(\frac{A}{A_0}\right)$ , with Phase Difference, $\psi$ , and Reduced Frequency, $k$ . . . . .	119
33.	Variation of Phase, $\varphi$ , with Phase Difference, $\psi$ , and $\sigma$ . . . . .	121
34.	Variation of Amplitude Ratio, $\left(\frac{A}{A_0}\right)$ , with Phase Difference, $\psi$ , and $\sigma$ . . . . .	122

## NOMENCLATURE

Roman Symbols

$A$	a constant, see Equation (74)
$A_o$	mean drag coefficient as obtained by the least squares fit, see Equation (82)
$A_1, A_2$	constants in the expression for $\gamma_w$ , see Equation (27)
$A_c$	amplitude of drag fluctuations, obtained by the least squares fit, see Equation (82)
$a$	$x^* = ab$ is the point about which the airfoil rotates, $a$ is non-dimensional
$B(x^*, z^*, t)$	body surface function, see Equations (6) and (8)
$B_1(x^*), B_2(x^*)$	downwash functions, defined by Equation (22b)
$B_c(x^*)$	downwash function, defined by Equation (44)
$b$	airfoil semi-chord
$b_1, b_2, b_4, b_6, b_8$	constants required in the definition of the thickness function, Equation (60)
$C(k), C(2k)$	Theodorsen's function with arguments $k$ and $2k$ , respectively, see Equation (42)
$C(x^*)$	camber function
$C_1(x), C_2(x)$	functions associated with bound vorticity, $\gamma_a$ , see Equations (26), (32) and (33)
$C_{oc}(x), C_{1e}(x)$	functions associated with bound vorticity, $\gamma_a$ , see Equations (46)-(48)
$C_d$	drag coefficient, $D/\rho V_o^2 b$
$C_{do}$	steady drag coefficient
$C_f$	skin friction coefficient, wall shear stress divided by $\frac{1}{2} \rho V_o^2$

$C_l$	lift coefficient, $l/\rho V_o^2 b$
$C_{l_o}, C_{l_1}, C_{l_2}$	lift coefficients, defined by Equation (65a)
$C_m$	moment coefficient, $m/2\rho V_o^2 b^2$
$C_{m_o}, C_{m_1}, C_{m_2}$	moment coefficients, defined by Equation (65b)
$C_p$	pressure coefficient, $(p - p_\infty)/(\rho V_o^2/2)$
D	skin friction drag
d	distance from leading edge
$\bar{d}$	see Equation (83)
g	non-dimensional boundary layer velocity, see Equation (72a), $u/U_e$
H	shape factor, $\delta^*/\theta$
$H_v^{(2)}$	Hankel function of second kind, order $\nu$
h	non-dimensional translatory displacement, $h^*/b$ , also transformed boundary layer velocity, see Equation (72b)
$\bar{h}$	amplitude function for h, $h = \bar{h}e^{i\omega t}$ , Equation (56b)
$h^*$	represents translatory motion of the airfoil, $z_a^* = -h^*$
$\dot{h}^*$	translation velocity, $dh^*/dt$
$I(t)$	integral occurring in solution for wake vorticity, $\int V(\tau)d\tau$
$I_1, I_2, I_4, I_6, I_8$	functions defined by Equations (62b) and (62c)
i	index for the streamwise coordinate $\xi$ , also $\sqrt{-1}$
$J_o$	Bessel function, first kind
j	index for the vertical coordinate $\eta$
k	reduced frequency, $\omega b/V_o$
$k_n$	constant appearing in solution for $\gamma_w$ , see Equation (24)

$\ell$	lift, positive upwards, also non-dimensional turbulent viscosity, $1 + \epsilon/\nu$
$M$	number of data points in least square fit, $M = 20$ for laminar flow, $M = 40$ for turbulent flow
$m$	pitching moment about $x = x_m$ , positive leading edge up, also index for $\tau$
$n$	exponent in power law profile, $u/U_e = (y/\delta)^{\frac{1}{n}}$
$P_1(x), P_2(x)$	pressure functions, see Equations (41) and (63)
$P_{o_c}(x), P_{1_c}(x)$	pressure functions, see Equations (50) and (64)
$P_{o_t}(x), P_{1_t}(x)$	pressure functions, see Equations (54), (61) and (62)
$p$	local pressure
$\vec{q}, q$	velocity vector and magnitude respectively, see Equation (1)
$Re$	Reynolds number based on the semi-chord, $V_o b/\nu$
$Re_\theta$	Reynolds number based on $U_e$ and $\theta$ , $\theta U_e Re$
$Re_\xi$	Reynolds number based on $U_e$ and $\xi$ , $\xi U_e Re$
$r$	ratio of adjacent step sizes in $\eta$ direction, $\Delta\eta_{j+1}/\Delta\eta_j$
$S(x^*)$	source strength distribution
$s$	distance from leading edge, non-dimensionalized by chord
$T$	time, space-fixed frame
$T(x^*), T^1(x^*)$	thickness function and derivative, respectively
$t$	time, body-fixed frame
$U_e$	total streamwise potential flow velocity at surface, non-dimensionalized by $V_o$ , see Equation (66)
$u$	disturbance velocity, $\frac{\partial \phi}{\partial x}$ , also non-dimensional stream-wise velocity in boundary layer



$u_s$	perturbation velocity due to thickness function, see Equation (53)
$u_\tau$	friction velocity, $\sqrt{\frac{C_f}{2}}$
$V(t)$	free stream velocity, see Equation (21) also
$V_o$	constant part of $V$
$v$	vertical velocity in the boundary layer, non-dimensionalized by $V_o$
$w$	downwash velocity, $\frac{\partial \phi}{\partial z}^*$
$X$	streamwise coordinate, space-fixed frame
$x$	$x^*/b$
$x^*$	streamwise coordinate in body-fixed frame, origin at midchord, positive aft
$y$	normal boundary layer coordinate, non-dimensionalized by semi-chord $b$
$Z$	vertical coordinate, space-fixed frame
$z$	$z^*/b$
$z^*$	vertical coordinate, body-fixed frame
$z_a^*$	amplitude function for $z_a^*$ , see Equation (20)

### Greek Symbols

$\alpha$	in Chapter II varying part of total angle of attack, in Chapter IV total angle of attack, positive leading edge up
$\bar{\alpha}$	amplitude for varying angle of attack, see Equation (56a)
$\alpha_o$	constant part of total angle of attack, positive leading edge up
$\beta_x$	longitudinal pressure gradient parameter, $\frac{\xi}{U_e} \frac{\partial U_e}{\partial \xi}$
$\beta_t$	unsteady pressure gradient parameter, $\frac{k\xi}{U_e^2} \frac{\partial U_e}{\partial \tau}$

$\Gamma_a$	airfoil circulation, see Equation (17)
$\gamma_a$	bound vorticity
$\gamma_w$	wake vorticity
$\delta$	boundary layer thickness, non-dimensionalized by the semi-chord $b$
$\bar{\delta}$	transformed boundary layer thickness, $\left(\frac{Re U_e}{2\xi}\right)^{\frac{1}{2}} \delta$
$\delta^*$	boundary layer displacement thickness, non-dimensionalized by the semi-chord $b$
$\epsilon$	eddy viscosity
$\eta$	transformed vertical boundary layer coordinate, $\sqrt{Re} \left(\frac{U_e}{2\xi}\right)^{\frac{1}{2}} y$
$\Delta\eta_j$	$\eta_j - \eta_{j-1}$
$\theta$	boundary layer momentum thickness, non-dimensionalized by the semi-chord $b$
$\Lambda$	Karman-Pohlhausen parameter, $Re\delta^2 dU_e/dx$
$\Lambda_1, \Lambda_2$	defined by Equations (40a) and (40b)
$\nu$	kinematic viscosity
$\xi$	in Chapter II streamwise dummy variable, $\xi^*/b$ , in Chapter III non-dimensional streamwise coordinate ( $\xi = 0$ is the stagnation point)
$\Delta\xi_i$	$\xi_{i+1} - \xi_i$
$\rho$	density
$\sigma$	amplitude of free stream fluctuations, $V(t) = V_0(1 + \sigma e^{i\omega t})$
$\tau$	thickness ratio of airfoil, non-dimensionalized by chord, also dimensionless time, $\omega t$
$\Delta\tau_m$	$\tau_m - \tau_{m-1}$

$\Phi$	disturbance velocity potential in space-fixed frame, see Equations (1) and (2)
$\varphi$	in Chapter II disturbance velocity potential in body-fixed frame, see Equation (4); in Chapter IV phase difference between drag and free stream, see Equation (82)
$\psi$	phase difference between free stream, $(V/V_0) = 1 + \sigma \cos(\omega t)$ , and airfoil oscillations, $\alpha = \alpha_0 + \alpha_r \cos(\omega t + \psi)$
$\Omega_1, \Omega_2$	defined in Equation (28)
$\Omega_2^1$	$\Omega_2 = \sigma \Omega_2^1$
$\Omega_{1c}$	defined in Equation (49)
$\omega$	frequency

### Subscripts

a	refers to the airfoil
u	upper surface
l	lower surface
w	refers to the wake
$\infty$	refers to the far upstream conditions

## SUMMARY

An analytical study is presented regarding the unsteady skin friction drag of an oscillating airfoil exposed to a fluctuating free stream speed. One application of the results from such an investigation is in aeroelastic stability analyses of helicopter rotor blades undergoing pitching, flapping, and lead-lag (in-plane) types of oscillation. The flow, which of course is time-dependent, is considered to be incompressible and two-dimensional. Both laminar and turbulent conditions are covered in the analysis.

The unsteady potential flow pressure and velocity distributions required for the subsequent boundary layer analysis are obtained by an approximate development. In this potential flow analysis the airfoil oscillations and the free stream fluctuations are regarded to be simple harmonic in time and to have the same frequency. In addition, the disturbances due to the airfoil motion and the amplitude of the free stream fluctuations are assumed to be small. Vortices are distributed along the airfoil chord and wake to account for the lifting effects while the nonlifting (thickness) effect is represented by sources, also distributed along the chord. A simplifying approximation for the wake, based on the assumption of small free stream fluctuations, leads to the final expressions for the unsteady surface pressure and velocity distributions.

This pressure distribution is impressed on the time dependent boundary layer which is solved by the method of finite differences. The unsteady boundary layer analysis covers both laminar and turbulent

conditions, and, the turbulent region is represented by an appropriate existing eddy viscosity model.

Various aspects of the flow problem are investigated by a systematic variation of several important parameters. The influences, on the unsteady drag, of the amplitude of free stream fluctuations, reduced frequency, and phase difference between stream fluctuations and airfoil oscillations are studied. Some of these effects are interpreted, in the laminar case, by a consideration of the movement of the zero wall shear location; for the turbulent condition it is the transition point movements that are examined. The possibility of the superposition of drag is studied and finally, the dependency on the Reynolds number is considered.

It was found that the introduction of fluctuations in the free stream alters the skin friction drag considerably by causing significant fluctuations in the drag. There is a considerable difference between the drag behaviors of an airfoil at constant incidence and one undergoing oscillations about a mean angle of attack, both subjected to identical fluctuating free streams. The results also show that for an airfoil undergoing oscillations about a mean angle of attack in a fluctuating free stream, the phase (with respect to the free stream) and amplitude of the drag fluctuations are strongly dependent on the phase difference between the free stream fluctuations and airfoil oscillations. Depending on the values of the phase difference between free stream fluctuations and airfoil oscillations, reduced frequency, and amplitude of free stream fluctuations, the drag can either lead or lag the free stream. Whereas one particular type of drag superposition

was successful under laminar conditions, the same type of operation led to large errors in the laminar-turbulent case.

## CHAPTER I

### INTRODUCTION

Helicopter rotor blades have a much lower in-plane stiffness as compared to fixed wings of conventional aircraft. This difference forces the consideration of an additional degree of freedom in aeroelastic analyses of rotor systems, namely, the lead-lag or in-plane type of motion. Such a motion may occur by itself or can be coupled with the flapping and/or torsional degrees of freedom. In addition to the blade properties and rotor operating conditions the degree of coupling depends on the particular type of rotor system in use. The majority of existing rotor systems may be classified into two categories: the articulated and hingeless rotors. In the first system, which is more widely used, flap and lead-lag hinges are employed to attach the blade to the hub. The improved control power and the relative simplicity of construction of the hingeless rotor have made it an attractive alternative to the articulated rotor, thus leading to its general acceptance in recent years. In practice, for the hingeless rotor the flap, torsion, and lead-lag degrees of freedom are strongly coupled due to the constructional nature of the blade and hub assembly. It has generally been concluded that for a comprehensive modeling of the rotor system, it is necessary to include the flap, torsion, and lead-lag degrees of freedom, references [1-5].

The flap and torsion types of motion generate and, are primarily influenced by the lift and pitching moment, respectively. Similarly,

the lead-lag oscillations and the drag are strongly affected by each other. The time-dependent nature of the rotor environment requires that the forces and moments acting on the blade be considered as unsteady. While there exist several analytical and experimental studies regarding the unsteady lift and moment of an oscillating airfoil, a comprehensive treatment of the unsteady drag is not available.

This deficiency is reflected in the efforts of the helicopter industry as well as in research studies. Ormiston [6] has surveyed the methods used by six major helicopter companies and three other organizations to predict rotor dynamic loads. For drag, the approximations employed below stall were based on either steady state data or a constant friction drag coefficient. In the stall regime the methods used either the steady state drag or the approximation presented by Harris et al. [7]. Harris et al. attempted to incorporate, empirically, unsteady effects by introducing a "reference" angle of attack which was a function of the reduced frequency, Mach number, airfoil shape, and the azimuthal variation in blade angle of attack. This "reference" angle of attack was then used to calculate the drag from static drag curves. Regarding research efforts, most rotor analyses assume the drag coefficient to be a constant, for example, references [1], [8], and [9]. In addition to the approximation of Harris et al. [7] there have been a few other attempts to represent, empirically, the unsteady drag of the rotor blade, [10], [11], and [12]. Bellinger [12] proceeds on the interesting assumption that the unsteady lift and drag are related in a manner similar to the relationship between steady lift and drag. In this case and in other empirical approaches it is



not possible to ascertain the accuracy of the various representations for unsteady drag since there exists very little reliable experimental data for comparison.

The few available experimental results for unsteady drag are limited in scope. Philippe and Sagner [13] have made drag measurements of an oscillating airfoil in a constant free stream but present a very limited amount of data. The effect of lead-lag oscillations on the drag of an airfoil at constant incidence has been the subject of two independent experimental studies, those of Valensi and Rebont [14] and Kunz [15]. Reference [14] employed in-plane oscillations of the model while the results of reference [15] were obtained for the case of a stationary model in a fluctuating free stream.

It is well known that the introduction of unsteadiness in the flow can significantly alter the amplitude and phase characteristics of the lift and moment. Whether this is also true for airfoil drag is not known at present. As is evident from the preceding review of the existing literature a thorough investigation of the effects of unsteadiness on airfoil drag is needed. The primary objective of the present effort is to provide, analytically, comprehensive and detailed results regarding the unsteady skin friction drag of an airfoil undergoing flapping, torsional and lead-lag types of oscillation. The unsteady potential flow pressure distribution induced by these oscillations will influence the skin friction distribution. In cases where the laminar boundary layer becomes turbulent, the time-dependent pressure distribution will affect not only the skin friction distributions of both regimes but also the location of the transition point. The resulting

unsteady drag will thus be a function, basically, of the airfoil oscillations. The manner in which the aforementioned objective is achieved is described below.

Note that the unique feature of the present flow problem is the apparent speed fluctuations in the free stream that are associated with the lead-lag oscillations of the airfoil.

The unsteady potential flow around an oscillating flat plate in a fluctuating free stream has been considered by several investigators in the past. Isaacs [16], [17] has employed a series expansion for the vorticity distribution and evaluates the unknown coefficients in the expansion by satisfying the flow tangency condition at the surface and the Kutta condition at the trailing edge. Greenberg [18] has extended the constant free stream analysis of Theodorsen [19] which itself is based on the conformal transformation technique. Randall's [20] analysis employs the acceleration potential instead of the velocity potential and is based on the development presented in reference [21]. In the above studies the emphasis has been on obtaining the unsteady lift and moment and consequently, the results consist of these quantities only. The analysis of the boundary layer requires, however, the streamwise pressure gradient distribution.

In the present study the unsteady potential flow pressure distribution for an oscillating airfoil in a fluctuating free stream is obtained through an approximate analysis that is an extension of the Schwarz-Söhngen procedure [22]. The flow is considered to be incompressible and two-dimensional. The airfoil oscillations and free stream fluctuations are assumed to be small, simple harmonic in time

and, to have the same frequency. The lifting effects are represented by a distribution of vortices along the chord and wake while the non-lifting (thickness) effects are taken into account by a source distribution also along the chord. The assumption of small free stream fluctuations permits a simplifying approximation for the wake thus leading to the final expressions for the surface velocity and pressure distributions.

The unsteady boundary layer analysis is performed by the method of finite differences. The differencing scheme of Dwyer [23], [24] is used because it is simple and permits the rapid solution of the boundary layer equations. The scheme allows for variable step sizes. Backward differencing is employed for the streamwise and time derivatives while the normal derivatives in the transformed coordinates are represented by central differences. For the laminar case the Crank-Nicolson [25] method of differencing is used. The turbulent boundary, modeled by the Cebeci-Smith eddy viscosity formulation [26], is analyzed an implicit scheme. In both cases the resulting sets of simultaneous algebraic equations are in a tridiagonal matrix form. Iterations on the transport properties are required at each turbulent station. The locations of the transition points are determined by Michel's method [27]. It is pertinent to note that there exist several studies of the response of special classes of boundary layers to fluctuations in the free stream velocity. Of these, the laminar studies of Lighthill [28], Nickerson [29], and McCroskey and Philippe [30], and the measurements of Hill and Stenning [31] are of considerable interest to the present investigation. The turbulent computations of McCroskey

and Philippe [30] for a flat plate at zero incidence in a fluctuating free stream are also relevant to the present effort. The results from these four studies are discussed in detail in the chapter on results and discussion.

In the results and discussion chapter several aspects of the flow problem are investigated. Some comments regarding the extension of the present potential flow development to the case of different airfoil and free stream frequencies are made. After performing a detailed comparison of the present potential flow analysis with that of Greenberg [18], the results for unsteady drag are considered. Comparisons of present results with the experimental drag data of Valensi and Rebont [14] and Kunz [15] are made. These are followed by consideration of the effects of several important parameters on the unsteady drag variations for both completely laminar and laminar-turbulent conditions. The influences of the amplitude of free stream fluctuations, reduced frequency, and phase difference between stream fluctuations and airfoil oscillations are investigated. Some of these effects are interpreted, in the laminar case, by a consideration of the movements of the zero wall shear locations; for the turbulent condition it is the transition point movements that are studied. The possibility of the superposition of drag is examined and finally, the dependency on the Reynolds number is considered.

## CHAPTER II

### POTENTIAL FLOW DEVELOPMENT

In this chapter the unsteady potential flow development for an oscillating airfoil in a fluctuating free stream is presented. The flow is considered to be incompressible, irrotational, and two-dimensional. The airfoil oscillations and the free stream fluctuations are assumed to be simple harmonic in time. In addition, the disturbances due to the airfoil motion and the amplitude of the free stream fluctuations are assumed to be small. Vortices are distributed along the airfoil chord and wake to account for the lifting effects while the nonlifting effect is represented by sources, also distributed along the chord. A simplifying approximation for the wake, based on the assumption of small free stream fluctuations, leads to the final expressions for the various flow quantities.

#### Governing Relations

Consider an irrotational flow around a two-dimensional body. The velocity vector,  $\vec{q}$ , can be expressed as

$$\vec{q}(X,Z,T) = \nabla\phi \quad (1)$$

where  $X, Z$  are space-fixed rectangular Cartesian coordinates,  $T$  is time and  $\phi(X,Z,T)$  is the velocity potential. Since the flow is assumed to be incompressible, the continuity equation simplifies to Laplace's equation

$$\nabla^2 \Phi = 0 \quad (2)$$

For a flow that is incompressible the momentum equation can be integrated, giving the unsteady Bernoulli's equation as

$$\frac{p-p_\infty}{\rho} = \frac{q^2}{2} - \frac{\partial \Phi}{\partial T} \quad (3)$$

where

$p(X,Z,T)$  = local pressure

$p_\infty$  = pressure at infinity where the presence of the body  
is not felt by the fluid

$\rho$  = fluid density

$q$  = magnitude of  $\vec{q}$

Note that Equation (3) is expressed in an inertial reference frame.

Now consider an airfoil of infinite span translating in the negative X direction with speed  $V(t)$ . Let  $x^*$  and  $z^*$  be rectangular Cartesian coordinates fixed to the airfoil (Figure 1);  $t$  denotes time in the body-fixed system. Also, let  $\varphi(x^*, z^*, t)$  be the velocity potential in the body-fixed system. Equation (2), in terms of  $\varphi$ , becomes

$$\nabla^2 \varphi = 0 \quad (4)$$

The airfoil thickness, oscillations and fluctuations in the free stream are assumed to be sufficiently small such that

$$\frac{\partial \varphi}{\partial x^*}, \frac{\partial \varphi}{\partial z^*} \ll V$$

allowing  $\left(\frac{1}{V} \frac{\partial \varphi}{\partial x^*}\right)^2$ ,  $\left(\frac{1}{V} \frac{\partial \varphi}{\partial z^*}\right)^2$  to be neglected in comparison with  $\left(\frac{1}{V} \frac{\partial \varphi}{\partial x^*}\right)$ .

Then, Equation (3), expressed in body-fixed coordinates gives

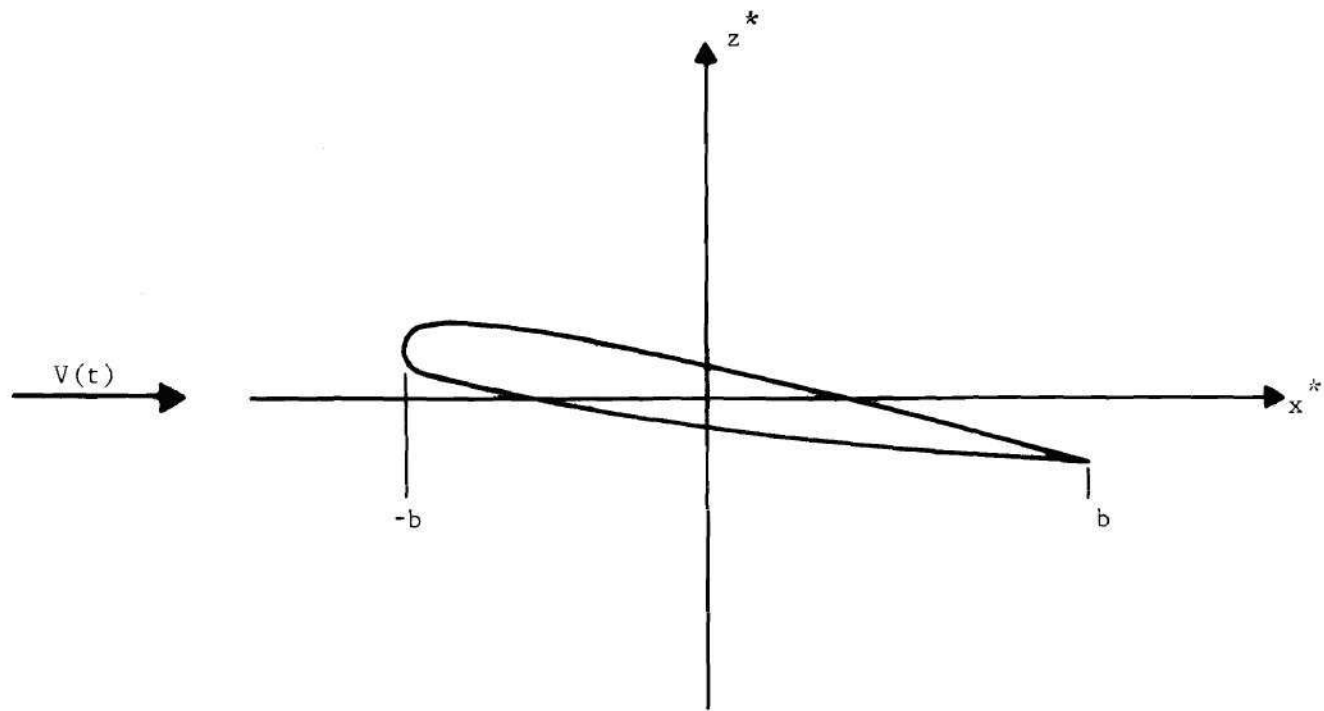


Figure 1. Definition of Axes

$$\frac{p-p_\infty}{\rho} = - \frac{\partial \phi}{\partial t} - V(t) \frac{\partial \phi}{\partial x^*} \quad (5)$$

The velocities in the  $x^*$  and  $z^*$  directions are given, respectively, by

$$V(t) + \frac{\partial \phi}{\partial x^*} = V(t) + u(x^*, z^*, t)$$

$$\frac{\partial \phi}{\partial z^*} = w(x^*, z^*, t)$$

### Boundary Conditions

At infinity, the presence of the airfoil is not felt by the fluid and free stream conditions prevail, hence,  $u$  and  $w$  must vanish.

The second boundary condition is specified at the airfoil surface. If the equation of the surface is given by

$$B(x^*, z^*, t) = 0 \quad (6)$$

this condition requires that for all points on the surface, at every instant of time,

$$\frac{\partial B}{\partial t} + (V+u) \frac{\partial B}{\partial x^*} + w \frac{\partial B}{\partial z^*} = 0 \quad (7)$$

(The velocity component normal to the surface must be zero; for further details see Lamb [32].)

It has previously been assumed that the airfoil creates small disturbances in the free stream, hence, in Equation (7)  $u$  may be neglected in comparison with  $V$ . Further, following thin airfoil theory, it is assumed that the surface boundary condition (7) can be applied in the vicinity of the plane  $z^* = 0$ . If the airfoil motion is prescribed by



$$B(x^*, z^*, t) = z^* - z_a^*(x^*, t) = 0 \quad (8)$$

than Equation (7) may be linearized as

$$w(x^*, 0, t) = \frac{\partial z_a^*}{\partial t} + V(t) \frac{\partial z_a^*}{\partial x} \quad (9)$$

A third condition (Kutta condition) applicable to airfoils with sharp trailing edges requires that there be zero pressure discontinuity between the upper and lower surfaces at the trailing edge and in the wake; further details can be found in Bisplinghoff et al. [22].

To summarize, the unknowns at the surface, velocity  $u$  and pressure  $p$ , have to be determined from Equations (4), (5) and (9), the Kutta condition, and the condition at infinity.

#### Solution Procedure

Since the governing equations are linear the problem of an oscillating airfoil in a fluctuating free stream can be split up into three parts:

- i) an oscillating flat plate
- ii) a camber line at constant angle of attack
- iii) a thickness (symmetrical) form at zero angle of attack

All three contributions are subjected to the same fluctuating free stream.

#### Oscillating Flat Plate

Consider a flat plate airfoil that is pitching and translating vertically. It can be shown, [22], that Laplace's equation (4) and the condition at infinity can be satisfied by a distribution of elementary

two-dimensional vortices along the  $x^*$ -axis. Then the potential  $\varphi$  is given as

$$\varphi(x^*, z^*, t) = -\frac{1}{2\pi} \int \gamma(\xi^*, t) \tan^{-1} \left( \frac{z^*}{x^* - \xi^*} \right) d\xi^* \quad (10)$$

where  $\gamma(\xi^*, t)$  is the circulation per unit distance, positive clockwise.

The unsteady character of the flow necessitates the distribution of vortices not only along the chord but also in the wake, which extends from the trailing edge to infinity. The wake vortices are also assumed to lie along the  $x^*$ -axis. Let the circulation per unit distance on the airfoil be  $\gamma_a$  (bound vorticity) and in the wake,  $\gamma_w$  (wake vorticity). Also, let the origin of the  $x^*, z^*$  axes be located at the mid-chord of the airfoil so that  $x^* = -b$  and  $x^* = b$  refer to the leading and trailing edges respectively. Then the downwash at  $z^* = 0$ , derived from the above equation is, [22]

$$w(x^*, 0, t) = -\frac{1}{2\pi} \oint_{-b}^b \frac{\gamma_a(\xi^*, t)}{x^* - \xi^*} d\xi^* - \frac{1}{2\pi} \int_b^\infty \frac{\gamma_w(\xi^*, t)}{x^* - \xi^*} d\xi^* \quad (11)$$

where  $\oint$  is the Cauchy principal value.

Next, the Kutta condition, which specifies zero pressure discontinuity at the trailing edge and in the wake, is considered. Stated mathematically the condition is

$$p_\ell - p_u = 0 \quad (x^* \geq b) \quad (12)$$

where the subscripts  $\ell$  and  $u$  refer to the lower and upper surfaces respectively. Using (5) the above equation is expressed as

$$\frac{\partial}{\partial t} (\varphi_u - \varphi_\ell) + v(t) \left( \frac{\partial \varphi_u}{\partial x^*} - \frac{\partial \varphi_\ell}{\partial x^*} \right) = 0 \quad (x^* \geq b) \quad (13)$$

From the definitions of  $\gamma_a$  and  $\gamma_w$  it can be shown that

$$\gamma_a = \frac{\partial \varphi_u}{\partial x^*} - \frac{\partial \varphi_b}{\partial x^*} \quad (-b \leq x^* \leq b) \quad (14)$$

and, for the wake region

$$\gamma_w = \frac{\partial \varphi_u}{\partial x^*} - \frac{\partial \varphi_b}{\partial x^*} \quad (x^* \geq b) \quad (15)$$

Using the above two relations and the fact that there are no velocity discontinuities upstream of the leading edge, Equation (13) is expressed as

$$\frac{d\Gamma_a}{dt} + \frac{\partial}{\partial t} \int_b^{x^*} \gamma_w(\xi^*, t) d\xi^* + V(t) \gamma_w(x^*, t) = 0 \quad (16)$$

where  $\Gamma_a(t)$  is the total bound circulation defined by

$$\Gamma_a(t) = \int_{-b}^b \gamma_a(\xi^*, t) d\xi^* \quad (17)$$

From Equation (16) the following can be derived

$$\frac{\partial \gamma_w}{\partial t} + V(t) \frac{\partial \gamma_w}{\partial x^*} = 0 \quad (18a)$$

$$\gamma_w(b, t) = - \frac{1}{V(t)} \frac{d\Gamma_a}{dt} \quad (18b)$$

Equation (18a) is obtained by differentiating (16) with respect to  $x^*$ ; setting  $x^* = b$  in (16) gives  $\gamma_w$  at the trailing edge, (18b). In addition to Equation (14), the following can also be derived from the definition of  $\gamma_a$

$$u_u = \frac{\partial \phi_u}{\partial x} = \frac{1}{2} \gamma_a \quad (19)$$

$$u_l = \frac{\partial \phi_l}{\partial x} = -\frac{1}{2} \gamma_a$$

It is not possible at this stage to completely determine  $\gamma_w$  from Equation (18a). However, the following form, obtained from the theory of first order partial differential equations [35], satisfies Equation (18a)

$$\gamma_w \sim f[k_n (I(t) - x^*)]$$

where  $k_n$  is a constant,  $f$  is an unknown function and

$$I(t) = \int V(\tau) d\tau$$

Note that to this point in the analysis the downwash,  $w$ , at the surface and the free stream velocity,  $V(t)$ , have not been specified, thus, the preceding relations are quite general. The time dependency of the airfoil oscillations and free stream fluctuations will be prescribed to be simple harmonic.

$$z_a^*(x^*, t) = z_a^*(x^*) e^{i\omega t} \quad (20)$$

$$V(t) = V_0 (1 + \sigma e^{i\omega t}) \quad (21)$$

where

$z_a^*(x^*)$  = amplitude function for the oscillations

$\omega$  = frequency

$V_0$  = constant mean free stream

$\sigma$  = amplitude of free stream fluctuations

It has been assumed in Equations (20) and (21) that the free stream is fluctuating with the same frequency as the airfoil oscillations. Substituting these functions into Equations (9) and (11) yields

$$B_1(x^*)e^{i\omega t} + \sigma B_2(x^*)e^{i2\omega t} = -\frac{1}{2\pi} \oint_{-b}^b \frac{\gamma_a(\xi^*, t)}{x^* - \xi^*} d\xi^* - \frac{1}{2\pi} \int_b^\infty \frac{\gamma_w(\xi^*, t)}{x^* - \xi^*} d\xi^* \quad (22a)$$

where

$$B_1(x^*) = i\omega z_a^{-*} + V_o \frac{dz_a^{-*}}{dx^*} \quad (22b)$$

$$B_2(x^*) = V_o \frac{dz_a^{-*}}{dx^*}$$

Similarly, (18a) and (18b) become

$$\frac{\partial \gamma_w}{\partial t} + V_o (1 + \sigma e^{i\omega t}) \frac{\partial \gamma_w}{\partial x^*} = 0 \quad (23a)$$

$$\gamma_w(b, t) = -\frac{1}{V_o (1 + \sigma e^{i\omega t})} \frac{d\Gamma_a}{dt} \quad (23b)$$

Note that the  $(2\omega t)$  term is a direct consequence of the fact that the free stream is fluctuating ( $\sigma \neq 0$ ).

The determination of  $\gamma_w$  will now be considered. First, it should be noted that in (22a)  $\gamma_w$  appears on the right hand side and, in each of the terms on the left hand side the spatial and temporal dependencies are separated. Secondly, for the constant free stream ( $\sigma = 0$ ) case the solution of (23a) is given by [22],

$$\gamma_w \sim e^{\frac{i\omega}{V_0} [I(t) - x^*]}$$

where  $I(t)$  in this case is

$$I(t) = V_0 t$$

These observations suggest that the unknown function,  $f$ , in the expression for  $\gamma_w$  given earlier is an exponential function. For the fluctuating free stream case then

$$\gamma_w \sim e^{k_n [I(t) - x^*]}$$

where  $k_n$  is a constant and

$$I(t) = \int V(\tau) d\tau = V_0 t + \frac{\sigma V_0}{i\omega} e^{i\omega t}$$

Note that (23a) is satisfied exactly by the above expression for  $\gamma_w$ .

The general solution being

$$\gamma_w(x^*, t) = \sum_n A_n e^{k_n [I(t) - x^*]}$$

where  $n$  is the summation index and the  $A_n$ 's are constants. If, for each term in the series, the quantity  $\left| \frac{k_n \sigma V_0}{i\omega} \right|$  is sufficiently small then

$$e^{k_n I(t)} \approx e^{k_n V_0 t} \left[ 1 + \left( \frac{k_n \sigma V_0}{i\omega} \right) e^{i\omega t} \right]$$

giving

$$\gamma_w(x^*, t) \approx \sum_n A_n e^{k_n (V_0 t - x^*)} \left[ 1 + \left( \frac{k_n \sigma V_0}{i\omega} \right) e^{i\omega t} \right] \quad (24)$$

In order to recover the  $\sigma = 0$  case (i.e. only the  $(i\omega t)$  term would be

present in (22a)) from the above solution

$$k_1 = \frac{i\omega}{V_0}$$

and all  $A_n$ 's except  $A_1$  should be zero. A non-zero  $\sigma$  introduces the  $(i2\omega t)$  term in (22a), and, by analogy

$$k_2 = \frac{i2\omega}{V_0}$$

giving

$$k_1 V_0 t = i\omega t \quad ; \quad \frac{k_1 \sigma V_0}{i\omega} = \sigma$$

and

$$k_2 V_0 t = i2\omega t \quad ; \quad \frac{k_2 \sigma V_0}{i\omega} = 2\sigma$$

Consider (22a) where the functional form of the bound vorticity,  $\gamma_a$ , is still unknown. If  $\gamma_a$  is assumed to be

$$\gamma_a(x^*, t) = C_1(x^*)e^{i\omega t} + C_2(x^*)e^{i2\omega t}$$

where  $C_1(x^*)$  and  $C_2(x^*)$  are unknown functions, and if  $k_1, k_2$  are taken as the values given earlier, then, only the first two terms of (24) are required for a term by term matching of the  $(i\omega t)$  and  $(i2\omega t)$  terms on both the sides of (22a). Taking only the first two terms in (24) and substituting for  $k_1, k_2$

$$\gamma_w(x^*, t) = \sum_{n=1}^2 A_n e^{(in\omega t - \frac{in\omega x^*}{V_0})} \left[ 1 + n\sigma e^{i\omega t} \right] \quad (25)$$

The above is valid only for sufficiently small values of  $\left| \frac{k_n \sigma V_0}{i\omega} \right|$  which, for  $k_n = \left( \frac{i n \omega}{V_0} \right)$   $n = 1, 2$ , reduces to  $n\sigma$ . Hence,  $\gamma_w$  can be approximated by (25) only for those values of  $\sigma$  that are small compared to unity.

Note however, that for  $n = 2$  in (25) there is present a  $(i3\omega t)$  term with coefficient  $(\sigma A_2)$ . This term has to be neglected, for consistency, since there is no  $(i3\omega t)$  term in (22a). As noted earlier, for  $\sigma = 0$   $A_2$  must be zero (which has yet to be shown). This implies  $A_2 \sim \sigma^\epsilon$  where  $\epsilon > 0$ , giving  $\sigma A_2 \sim \sigma^{1+\epsilon}$  thus making the neglected term  $\sim \sigma^{1+\epsilon}$ . Actually, as will be seen later  $\epsilon = 1$  making  $\sigma A_2 \sim \sigma^2$ . If after neglecting the  $(i3\omega t)$  term in (25) the expression for  $\gamma_w$  is substituted in (23a) it can be shown that the error (residue)  $\sim \sigma^2$ .

The final expressions for  $\gamma_a$  and  $\gamma_w$  are then

$$\gamma_a(x, t) = C_1(x)e^{i\omega t} + C_2(x)e^{i2\omega t} \quad (26)$$

$$\begin{aligned} \gamma_w(x, t) = & A_1 e^{-ikx} e^{i\omega t} \\ & + (\sigma A_1 e^{-ikx} + A_2 e^{-i2kx}) e^{i2\omega t} \end{aligned} \quad (27)$$

where

$$x = \frac{x^*}{b}$$

$$k = \frac{\omega b}{v_0} \quad (\text{reduced frequency})$$

Also, let

$$\xi = \frac{\xi^*}{b}$$

and define

$$\Omega_1 = \int_{-1}^1 C_1(\xi) d\xi \quad ; \quad \Omega_2 = \int_{-1}^1 C_2(\xi) d\xi \quad (28)$$

The constants  $A_1$  and  $A_2$  are now found from the condition at the trailing edge, (23b). Using (26) the total bound circulation  $\Gamma_a(t)$ , (17), is



$$\Gamma_a(t) = b\Omega_1 e^{i\omega t} + be^{i2\omega t}\Omega_2$$

giving

$$\dot{\Gamma}_a(t) = \frac{d\Gamma_a}{dt} = i\omega b(\Omega_1 e^{i\omega t} + 2\Omega_2 e^{i2\omega t})$$

Using the above equation and (27) with  $x = 1$ , the Kutta condition of Equation (23b) is expressed as

$$\begin{aligned} A_1 e^{-ik} e^{i\omega t} + (\sigma A_1 e^{-ik} + A_2 e^{-i2k}) e^{i2\omega t} \\ = \frac{-ik\Omega_1 e^{i\omega t}}{(1+\sigma e^{i\omega t})} - \frac{i2k\Omega_2 e^{i2\omega t}}{(1+\sigma e^{i\omega t})} \end{aligned}$$

$A_1$  is determined by multiplying both sides of the above equation by  $e^{-i\omega t}$  and integrating with respect to  $(\omega t)$  from 0 to  $2\pi$ ; the same procedure with  $e^{-i2\omega t}$  instead of  $e^{-i\omega t}$  is used for  $A_2$ , giving

$$A_1 = -ik\Omega_1 e^{ik} ; \quad A_2 = -i2k(-\sigma\Omega_1 + \Omega_2) e^{i2k}$$

Substituting these values into Equation (27) yields

$$\begin{aligned} \gamma_w(x, t) = -ik\Omega_1 e^{-ik(x-1)} e^{i\omega t} \\ - ik \left[ \sigma\Omega_1 e^{-ik(x-1)} + 2(-\sigma\Omega_1 + \Omega_2) e^{-i2k(x-1)} \right] e^{i2\omega t} \end{aligned} \quad (29)$$

The next step is to determine the functions  $C_1(x)$  and  $C_2(x)$  which appear in (26). Equations (26) and (29) are used in the surface boundary condition (22a) and, the coefficients of the  $e^{i\omega t}$  terms on both sides of (22a) are equated. This gives a singular integral equation for  $C_1(x)$ . The same procedure for the  $e^{i2\omega t}$  terms yields a second singular integral equation, for  $C_2(x)$ . After rearranging, the two equations are

$$-B_1(x) + \frac{ik}{2\pi} e^{ik\Omega_1} \int_1^\infty \frac{e^{-ik\xi}}{x-\xi} d\xi = \frac{1}{2\pi} \oint_{-1}^1 \frac{C_1(\xi)}{x-\xi} d\xi \quad (30)$$

$$\begin{aligned} -\sigma B_2(x) + \frac{ik}{2\pi} \left\{ \sigma e^{ik\Omega_1} \int_1^\infty \frac{e^{-ik\xi}}{x-\xi} d\xi + 2(-\sigma\Omega_1 + \Omega_2) e^{i2k} \int_1^\infty \frac{e^{-i2k\xi}}{x-\xi} d\xi \right\} \\ = \frac{1}{2\pi} \oint_{-1}^1 \frac{C_2(\xi)}{x-\xi} d\xi \end{aligned} \quad (31)$$

Equation (30) is nothing but the bound vorticity equation for the constant free stream case [22]; whereas (31) contains the effect of free stream fluctuations. The Schwarz-Söhngen procedure for obtaining  $C_1(x)$  from (30) is described in [22]; the same method will be used here to obtain  $C_2(x)$  from (31). Schwarz established that (30) could be inverted using Söhngen's inversion relations if one temporarily regards  $\Omega_1$  as a known constant.  $C_1(x)$  and the entire left hand side are assumed to be piecewise continuous and/or to have only a finite number of integrable singularities. Further, a unique solution is given for the case when  $C_1(1)$  is bounded. It is assumed here that  $C_2(x)$  also satisfies all the conditions imposed on  $C_1(x)$ .

Inverting (30) and (31) by using the above mentioned procedure and simplifying one of the integrals by interchanging orders of integration gives

$$C_1(x) = \frac{2}{\pi} \sqrt{\frac{1-x}{1+x}} \left\{ \oint_{-1}^1 \sqrt{\frac{1+\xi}{1-\xi}} \frac{B_1(\xi)}{(x-\xi)} d\xi + \frac{ik}{2} e^{ik\Omega_1} \int_1^\infty \sqrt{\frac{\lambda+1}{\lambda-1}} \frac{e^{-ik\lambda}}{x-\lambda} d\lambda \right\} \quad (32)$$

$$\begin{aligned} C_2(x) = \frac{2}{\pi} \sqrt{\frac{1-x}{1+x}} \left\{ \oint_{-1}^1 \sqrt{\frac{1+\xi}{1-\xi}} \frac{\sigma B_2(\xi)}{(x-\xi)} d\xi + \frac{ik}{2} \left[ \sigma e^{ik\Omega_1} \int_1^\infty \sqrt{\frac{\lambda+1}{\lambda-1}} \frac{e^{-ik\lambda}}{x-\lambda} d\lambda \right. \right. \\ \left. \left. + 2e^{i2k} (-\sigma\Omega_1 + \Omega_2) \int_1^\infty \sqrt{\frac{\lambda+1}{\lambda-1}} \frac{e^{-i2k\lambda}}{x-\lambda} d\lambda \right] \right\} \end{aligned} \quad (33)$$

Using the definitions of (28) and integrating (32) and (33) between the limits  $(-1,1)$  yields  $\Omega_1$  and  $\Omega_2$  as

$$\Omega_1 = \frac{4 \int_{-1}^1 \sqrt{\frac{1+\xi}{1-\xi}} B_1(\xi) d\xi}{\pi i k e^{ik} [H_1^{(2)}(k) + iH_0^{(2)}(k)]} \quad (34a)$$

$$\begin{aligned} \Omega_2 = \sigma \left\{ \frac{4 \int_{-1}^1 \sqrt{\frac{1+\xi}{1-\xi}} B_2(\xi) d\xi}{\pi i (2k) e^{i2k} [H_1^{(2)}(2k) + iH_0^{(2)}(2k)]} \right. \\ \left. + \Omega_1 \left[ 1 - \frac{1}{2e^{ik}} \left( \frac{H_1^{(2)}(k) + iH_0^{(2)}(k)}{H_1^{(2)}(2k) + iH_0^{(2)}(2k)} \right) \right] \right\} \quad (34b) \end{aligned}$$

Let  $\Omega_2^1$  be such that  $\Omega_2 = \sigma \Omega_2^1$ , then  $(-\sigma \Omega_1 + \Omega_2) = \sigma(-\Omega_1 + \Omega_2^1)$ . From (34)

$$(-\Omega_1 + \Omega_2^1) = \frac{2 \int_{-1}^1 \sqrt{\frac{1+\xi}{1-\xi}} [B_2(\xi) - B_1(\xi)] d\xi}{\pi i k e^{i2k} [H_1^{(2)}(2k) + iH_0^{(2)}(2k)]} \quad (35)$$

$H_\nu^{(2)}$  is the Hankel function of second kind and order  $\nu$ .

The use of (34a) in (32), and (35) in (33) completes the determination of  $C_1(x)$  and  $C_2(x)$ . The perturbation velocities, (19), can then be found by the use of (26). The total velocities at the upper and lower surfaces are given by  $(V(t) + \frac{\gamma_a}{2})$  and  $(V(t) - \frac{\gamma_a}{2})$  respectively.

Before proceeding further the comment made earlier regarding the  $(i3\omega t)$  term in Equation (25) for  $\gamma_w$  is considered. As can be seen from (34b)  $\Omega_2 \sim \sigma$  and since

$$A_2 = -i2k(-\sigma \Omega_1 + \Omega_2) e^{i2k}$$

this implies  $A_2 \sim \sigma$ , thus making  $\sigma A_2 \sim \sigma^2$ . It may also be noted here that  $C_2(x) = 0$  when  $\sigma = 0$ , see Equations (33) and (34b).

The pressure distribution can be determined using Equation (19) for the potential derivatives in the pressure-potential relation (5) for points on the airfoil surface as

$$\frac{p_{u,l}(x,t) - p_\infty}{\rho V_o} = \mp \frac{1}{2} \left[ \frac{V(t)}{V_o} \gamma_a(x,t) + \frac{b}{V_o} \frac{\partial}{\partial t} \int_{-1}^x \gamma_a(\xi,t) d\xi \right] \quad (36)$$

where the subscript u and the minus sign are for the upper surface and the subscript l and plus sign refer to the lower surface. Using Equations (21) and (26) the first term on the right hand side of the above equation is expressed as

$$\frac{V(t)}{V_o} \gamma_a(x,t) = C_1(x) e^{i\omega t} + [\sigma C_1(x) + C_2(x)] e^{i2\omega t} \quad (37)$$

where the  $(i3\omega t)$  term ( $\sim \sigma^2$ ) has been neglected. Equation (26) can be used to evaluate the second term of (36) as

$$\frac{b}{V_o} \frac{\partial}{\partial t} \int_{-1}^x \gamma_a(\xi,t) d\xi = ik \left[ \int_{-1}^x C_1(\xi) d\xi e^{i\omega t} + 2 \int_{-1}^x C_2(\xi) d\xi e^{i2\omega t} \right] \quad (38)$$

The procedure for expressing the first integral on the right hand side of (38) in terms of known quantities is given in reference [22]; the same series of steps is applied to the second integral.

$$\int_{-1}^x C_1(\xi) d\xi = -\frac{2}{\pi} \int_{-1}^1 \Lambda_1(x,\xi) B_1(\xi) d\xi - \frac{\Omega_1 e^{ik}}{\pi} \int_1^\infty \frac{\partial \Lambda_2}{\partial \lambda} e^{-ik\lambda} d\lambda \quad (39a)$$

$$\int_{-1}^x C_2(\xi) d\xi = \sigma \left\{ -\frac{2}{\pi} \int_{-1}^1 \Lambda_1(x, \xi) B_2(\xi) d\xi - \frac{\Omega_1 e^{ik}}{\pi} \int_1^{\infty} \frac{\partial \Lambda_2}{\partial \lambda} e^{-ik\lambda} d\lambda \right. \\ \left. - \frac{(-\Omega_1 + \Omega_2^1) e^{i2k}}{\pi} \int_1^{\infty} \frac{\partial \Lambda_2}{\partial \lambda} e^{-i2k\lambda} d\lambda \right\} \quad (39b)$$

where,  $\Omega_2^1$  (defined previously) is given by

$$\Omega_2 = c\Omega_2^1$$

and

$$\Lambda_1(x, \xi) = \frac{1}{2} \ln \left[ \frac{1-x\xi + \sqrt{1-\xi^2} \sqrt{1-x^2}}{1-x\xi - \sqrt{1-\xi^2} \sqrt{1-x^2}} \right] \quad (40a)$$

$$\Lambda_2(x, \lambda) = 2 \tan^{-1} \left[ \sqrt{\frac{(1-x)(\lambda+1)}{(1+x)(\lambda-1)}} \right] - \pi \quad (40b)$$

$$\frac{\partial \Lambda_2}{\partial \lambda} = \sqrt{\frac{1-x}{1+x}} \left[ \frac{1}{\sqrt{\lambda^2-1}} + \sqrt{\frac{\lambda+1}{\lambda-1}} \frac{1}{(x-\lambda)} \right] \quad (40c)$$

Substituting these results in Equation (36) gives the final expression (after certain cancellations) for pressure as

$$\frac{p_{u,l}(x, t) - p_{\infty}}{\rho V_o^2} = + \frac{1}{2} \left[ P_1(x) e^{i\omega t} + \sigma P_2(x) e^{i2\omega t} \right] \quad (41a)$$

where

$$P_1(x) = \frac{2}{\pi} \left[ 1 - C(k) \right] \sqrt{\frac{1-x}{1+x}} \int_{-1}^1 \sqrt{\frac{1+\xi}{1-\xi}} \frac{B_1(\xi)}{V_o} d\xi \\ + \frac{2}{\pi} \int_{-1}^1 \left[ \sqrt{\frac{1-x}{1+x}} \sqrt{\frac{1+\xi}{1-\xi}} \frac{1}{x-\xi} - ik\Lambda_1(x, \xi) \right] \frac{B_1(\xi)}{V_o} d\xi \quad (41b)$$

$$\begin{aligned}
p_2(x) = & \frac{2}{\pi} [1 - C(2k)] \sqrt{\frac{1-x}{1+x}} \int_{-1}^1 \sqrt{\frac{1+\xi}{1-\xi}} \frac{[B_2(\xi) - B_1(\xi)]}{V_0} d\xi \\
& + \frac{2}{\pi} \int_{-1}^1 \left[ \sqrt{\frac{1-x}{1+x}} \sqrt{\frac{1+\xi}{1-\xi}} \frac{1}{x-\xi} - i2k\Lambda_1(x, \xi) \right] \frac{B_2(\xi)}{V_0} d\xi \\
& + \frac{2}{\pi} \sqrt{\frac{1-x}{1+x}} \left\{ \int_{-1}^1 \sqrt{\frac{1+\xi}{1-\xi}} \frac{1}{(x-\xi)} \frac{B_1(\xi)}{V_0} d\xi \right. \\
& \left. + 2[1 - C(k)] \int_{-1}^1 \sqrt{\frac{1+\xi}{1-\xi}} \frac{B_1(\xi)}{V_0} d\xi \right\} \quad (41c)
\end{aligned}$$

and  $C(k)$  is the Theodorsen function [19] defined by

$$C(k) = \frac{H_1^{(2)}(k)}{H_1^{(2)}(k) + iH_0^{(2)}(k)} \quad (42)$$

#### Camber Line at Constant Angle of Attack

Consider a camber line  $C(x^*)$  at a constant angle of attack  $\alpha_0$  subjected to a free stream  $V(t)$ . The downwash  $w$  from (9) is given by

$$w(x^*, 0, t) = V_0 (1 + \sigma e^{i\omega t}) \left( \frac{dC}{dx^*} - \alpha_0 \right)$$

where  $V(t)$  has been assumed to be given by (21). The above can be expressed in the form

$$w(x^*, 0, t) = B_C(x^*) + \sigma B_C(x^*) e^{i\omega t} \quad (43)$$

where

$$B_C(x^*) = V_0 \left( \frac{dC}{dx^*} - \alpha_0 \right) \quad (44)$$

The procedure for determining  $\gamma_w$ ,  $\gamma_a$  and the surface pressure is the same as that for the oscillating flat plate. Vortices are distributed along the chord and in the wake. Equations (10)-(19) are valid for this case with the downwash given by (43). The assumption of small  $\sigma$  allows the solution of (18a) to be approximated by a single  $(i\omega t)$  term. The steady term in (43) does not contribute to  $\gamma_w$ , since all the wake vorticity associated with this term is assumed to have propagated far downstream to infinity. The steady term, however, does give rise to a constant  $\gamma_a$ . As before, terms that have  $(\sigma^2)$  dependency are neglected. Since the intermediate steps are the same as for the oscillating flat plate, only the final equations are presented.

$$\gamma_w(x,t) = -ik\Omega_{1c} e^{-ik(x-1)} e^{i\omega t} \quad (45)$$

$$\gamma_a(x,t) = C_{0c}(x) + C_{1c}(x) e^{i\omega t} \quad (46)$$

where

$$C_{0c}(x) = \frac{2}{\pi} \sqrt{\frac{1-x}{1+x}} \int_{-1}^1 \sqrt{\frac{1+\xi}{1-\xi}} \frac{B_c(\xi)}{(x-\xi)} d\xi \quad (47)$$

$$C_{1c}(x) = \frac{2}{\pi} \sqrt{\frac{1-x}{1+x}} \left\{ \int_{-1}^1 \sqrt{\frac{1+\xi}{1-\xi}} \frac{\sigma B_c(\xi)}{x-\xi} d\xi + \frac{ike^{ik}}{2} \Omega_{1c} \int_1^\infty \sqrt{\frac{\lambda+1}{\lambda-1}} \frac{e^{-ik\lambda}}{x-\lambda} d\lambda \right\} \quad (48)$$

$$\Omega_{1c} = \frac{4 \int_{-1}^1 \sqrt{\frac{1+\xi}{1-\xi}} \sigma B_c(\xi) d\xi}{\pi i k e^{ik} [H_1^{(2)}(k) + iH_0^{(2)}(k)]} \quad (49)$$

The pressure relation (36) becomes

$$\frac{p_{u,l}(x,t) - p_{\infty}}{\rho V_0^2} = \mp \frac{1}{2} \left[ p_{o_c}(x) + \sigma p_{l_c}(x) e^{i\omega t} \right] \quad (50a)$$

where

$$p_{o_c}(x) = \frac{2}{\pi} \sqrt{\frac{1-x}{1+x}} \int_{-1}^1 \sqrt{\frac{1+\xi}{1-\xi}} \frac{1}{x-\xi} \frac{B_c(\xi)}{V_0} d\xi \quad (50b)$$

$$p_{l_c}(x) = \frac{2}{\pi} [1-C(k)] \sqrt{\frac{1-x}{1+x}} \int_{-1}^1 \sqrt{\frac{1+\xi}{1-\xi}} \frac{B_c(\xi)}{V_0} d\xi \\ + \frac{2}{\pi} \int_{-1}^1 \left[ 2 \sqrt{\frac{1-x}{1+x}} \sqrt{\frac{1+\xi}{1-\xi}} \frac{1}{x-\xi} - ik\Lambda_1(x,\xi) \right] \frac{B_c(\xi)}{V_0} d\xi \quad (50c)$$

where  $\Lambda_1(x,\xi)$  and  $C(k)$  are defined by (40a) and (42) respectively.

#### Thickness Distribution at Zero Incidence

Consider a symmetrical thickness distribution  $\pm T(x^*)$  at zero angle of attack subjected to a free stream  $V(t)$ . The plus and minus signs refer to the upper and lower surfaces, respectively. The downwash  $w$  from Equation (9) becomes

$$w(x^*, \sigma^{\pm}, t) = \pm V(t) T^1(x^*) \quad (51)$$

where

$$T^1(x^*) \equiv \frac{dT}{dx}^*$$

A distribution along the  $x^*$  axis of two-dimensional steady sources can be made to satisfy (51) when  $V(t) \equiv V_0$ . The extension to the variable free stream case can be achieved by taking the perturbation velocity



potential as

$$\varphi(x^*, z^*, t) = \frac{V(t)}{V_0} \varphi_0(x^*, z^*) \quad (52)$$

where  $\varphi_0(x^*, z^*)$  is the steady two-dimensional perturbation velocity potential corresponding to the constant free stream  $V_0$ , and is given by

$$\varphi_0(x^*, z^*) = \frac{1}{2\pi} \int_{-b}^b S(\xi^*) \ln \left[ (x^* - \xi^*)^2 + z^{*2} \right]^{\frac{1}{2}} d\xi^*$$

$S(x^*)$  being the source strength distribution.

The procedure to determine  $S(x^*)$  and the surface perturbation velocity  $u_s(x^*, t) \equiv \left( \frac{\partial \varphi}{\partial x^*} \right)_{z^* \rightarrow 0}$  is identical to the one used for the steady case, found in any standard text [36] on elementary aerodynamics.

Equation (52) is differentiated with respect to  $z^*$  and the limits

$\left( \frac{\partial \varphi}{\partial z^*} \right)_{z^* \rightarrow 0 \pm}$  are taken after which using (51) leads to

$$S(x^*) = 2V_0 T^1(x^*)$$

which determines  $\varphi(x^*, z^*, t)$  completely. The surface perturbation velocity is then

$$u_s(x^*, t) = \left( \frac{\partial \varphi}{\partial x^*} \right)_{z^* \rightarrow 0} = \frac{V_0 (1 + \sigma e^{i\omega t})}{\pi} \int_{-b}^b \frac{T^1(\xi^*)}{x^* - \xi^*} d\xi^* \quad (53)$$

where it has been assumed that  $V(t)$  is given by (21). Further, at the surface

$$\frac{\partial \varphi}{\partial t} = \frac{i\omega V_0 \sigma}{\pi} \int_{-b}^b T^1(\xi^*) \ln |x^* - \xi^*| d\xi^* e^{i\omega t}$$

Using the preceding two relations in the pressure equation, (5), and neglecting the term of order  $\sigma^2$  gives the pressure at the surface as

$$\frac{p_{u,l}(x,t) - p^\infty}{\rho V_o^2} = -\frac{1}{2} \left[ P_{o_t}(x) + \sigma P_{l_t}(x) e^{i\omega t} \right] \quad (54a)$$

where

$$P_{o_t}(x) = \frac{2}{\pi} \int_{-1}^1 \frac{T^1(\xi)}{x-\xi} d\xi \quad (54b)$$

$$P_{l_t}(x) = \frac{2ik}{\pi} \int_{-1}^1 T^1(\xi) \ln|x-\xi| d\xi + \frac{4}{\pi} \int_{-1}^1 \frac{T^1(\xi)}{x-\xi} d\xi \quad (54c)$$

### Equations for a Symmetrical Airfoil

Consider an airfoil that is simultaneously pitching and translating vertically, subjected to a fluctuating free stream speed given by  $V_o(1 + \sigma e^{i\omega t})$ . Let the constant part of the angle of attack be  $\alpha_o$ , the varying part be  $\alpha(t)$  and, assume that the airfoil is pitching about the point  $x^* = ab$ . The vertical translation is assumed to be given by  $z^* = -h^*(t)$ . The camber and thickness functions are assumed to be given by  $C(x^*)$  and  $T(x^*)$  respectively. Then for small displacements the airfoil surface equation is

$$z_a^*(x^*, t) = [(ab - x^*)\alpha(t) - h^*(t)] + [C(x^*) + (ab - x^*)\alpha_o] \pm T(x^*) \quad (55)$$

where the plus and minus signs refer to the upper and lower surfaces respectively.

Only the camber and thickness functions depend on the geometric shape of the airfoil, the rest of the terms can be associated with an equivalent flat plate. The oscillating flat plate contribution is given by the terms in the first square bracket on the right hand side; the second bracket contains the terms that correspond to the camber line

at constant angle of attack.

Let

$$\alpha(t) = \bar{\alpha} e^{i\omega t} \quad (56a)$$

$$h(t) = \bar{h} e^{i\omega t} \quad (h \equiv \frac{\bar{h}}{b}^*) \quad (56b)$$

The oscillating flat plate downwash functions, (22b), are then given by

$$\frac{B_1}{V_0}(x) = -\bar{\alpha} - ik\bar{\alpha}(x-a) - ik\bar{h} \quad (57a)$$

$$\frac{B_2}{V_0}(x) = -\bar{\alpha} \quad (57b)$$

For a symmetrical airfoil (zero camber), the fixed angle of attack downwash function, (44), is

$$\frac{B_c}{V_0}(x) = -\alpha_0 \quad (58)$$

The thickness distribution  $T(x)$  is taken to be the same as that for the NACA 00XX airfoils. The function that is actually required is  $T^1(x)$ , obtained by differentiating  $T(x)$ . Let

$$x_\rho = 1 + x \quad (59)$$

then

$$T^1(x) = \tau \left[ \frac{b_1}{\sqrt{2}} \frac{1}{\sqrt{x}_\rho} + b_2 + b_4 x_\rho + \frac{3}{4} b_6 x_\rho^2 + \frac{b_8}{2} x_\rho^3 \right] \quad (60)$$

where  $\tau$  is the thickness ratio, based on the chord. The constants  $b_1$ ,  $b_2$ ,  $b_4$ ,  $b_6$ ,  $b_8$  define the profile and have the values [33]

$$b_1 = 1.48450 ; \quad b_2 = -0.63000 ; \quad b_4 = -1.75800 ;$$

$$b_6 = 1.42150 ; \quad b_8 = -0.50750$$

For the  $T^1(x)$  specified by Equation (60) Van Dyke [33] has evaluated the Cauchy principal value

$$\oint_{-1}^1 \frac{T^1(\xi)}{x-\xi} d\xi$$

and his result is employed in the present work (see Equations (53), (54b) and (54c)) to yield

$$\begin{aligned} \oint_{-1}^1 \frac{T^1(\xi)}{x-\xi} d\xi = & \tau \left[ \frac{1}{\tau} T^1(x) \ln \left| \frac{x_\rho}{1-x} \right| + \frac{\sqrt{2} b_1}{\sqrt{x}_\rho} \ln \left( \frac{\sqrt{2} + \sqrt{x}_\rho}{\sqrt{x}_\rho} \right) \right. \\ & \left. - \left( 2b_4 + \frac{3}{2}b_6 + \frac{4}{3}b_8 \right) - \left( \frac{3b_6 + 2b_8}{2} \right) x_\rho - b_8 x_\rho^2 \right] \end{aligned} \quad (61)$$

Equation (54c) contains a second integral which, when evaluated for the  $T^1(x)$  of (60) becomes

$$\int_{-1}^1 T^1(\xi) \ln |x-\xi| d\xi = \tau \left( \frac{b_1}{2} I_1 + b_2 I_2 + 2b_4 I_4 + 3b_6 I_6 + 4b_8 I_8 \right) \quad (62a)$$

where

$$I_1(x) = -4 + 2 \ln |x-1| - \sqrt{2x}_\rho \ln \left( \frac{\sqrt{2} - \sqrt{x}_\rho}{\sqrt{2} + \sqrt{x}_\rho} \right) \quad (62b)$$

and for  $m = 0, 1, 2, 3$

$$\begin{aligned}
\frac{I(x)}{2(m+1)} &= \frac{1}{(m+1)} \left\{ \ln|x-1| + \left( \frac{x_p}{2} \right)^{m+1} \left[ \ln \left| \frac{x_p}{x-1} \right| - \sum_{r=1}^{m+1} \frac{1}{r} \left( \frac{2}{x_p} \right)^r \right] \right\} \\
&\quad (x \neq -1, \text{ i.e. } x_p \neq 0) \\
&= \frac{1}{m+1} \left( \ln 2 - \frac{1}{m+1} \right) \quad (x = -1, \text{ i.e. } x_p = 0) \quad (62c)
\end{aligned}$$

The downwash functions  $B_1(x)$  and  $B_2(x)$  from Equations (57) are substituted into the pressure relations, (41), for the oscillating flat plate. Similarly,  $B_c(x)$  from (58) is used in the constant incidence relations, (50). The various Cauchy principal values and improper integrals are evaluated and the results are given below. The surface pressures were expressed as

$$\frac{p_{u,l}(x,t) - p_\infty}{\rho V_o^2} = \frac{1}{2} \left[ P_1(x) e^{i\omega t} + \sigma P_2(x) e^{i2\omega t} \right] \quad (41a)$$

and

$$\frac{p_{u,l}(x,t) - p_\infty}{\rho V_o^2} = \frac{1}{2} \left[ P_{oc}(x) + \sigma P_{1c} e^{i\omega t} \right] \quad (50a)$$

where

$$\begin{aligned}
P_1(x) &= 2 \sqrt{\frac{1-x}{1+x}} \left[ \left( \bar{\alpha} + ik\bar{\alpha} \left( \frac{1}{2} - a \right) + ik\bar{h} \right) C(k) + ik\bar{\alpha} \left( \frac{1}{2} + x \right) \right] \\
&\quad + 2ik\sqrt{1-x^2} \left[ \bar{\alpha} + ik\bar{\alpha} \left( \frac{x}{2} - a \right) + ik\bar{h} \right] \quad (63a)
\end{aligned}$$

$$P_2(x) = 2 \sqrt{\frac{1-x}{1+x}} \left[ - \left( ik\bar{\alpha} \left( \frac{1}{2} - a \right) + ik\bar{h} \right) C(2k) + 2 \left( \bar{\alpha} + ik\bar{\alpha} \left( \frac{1}{2} - a \right) \right) \right]$$

$$+ ik\bar{h})C(k) + ik\bar{\alpha} \left( \frac{1}{2} + x \right) \Big] + 4ik\bar{\alpha}\sqrt{1-x^2} \quad (63b)$$

$$P_{o_c}(x) = 2\alpha_o \sqrt{\frac{1-x}{1+x}} \quad (64a)$$

$$P_{l_c}(x) = 2\alpha_o C(k) \sqrt{\frac{1-x}{1+x}} + 2ik\alpha_o \sqrt{1-x^2} \quad (64b)$$

The contribution to the surface pressure from the thickness distribution is obtained from Equations (54). Since the determination of  $P_{o_t}(x)$  and  $P_{l_t}(x)$  involves only straightforward substitutions of Equation (61) into (54b) and (54c), and (62a) into (54c), the final expressions for  $P_{o_t}(x)$  and  $P_{l_t}(x)$  will not be presented here.

Expressions for the lift and moment are given next. The thickness function produces neither lift nor moment due to its symmetrical loading. In the following equations the contributions from the oscillating flat plate and the straight camber line at fixed incidence have been grouped together.

Define

$$C_l = \frac{l}{\rho V_o^2 b} \quad ; \quad C_m = \frac{m}{2\rho V_o^2 b^2}$$

where  $l$  is the lift and  $m$  is the pitching moment about the point  $x = x_m$ , positive leading edge up.

The coefficients  $C_l$  and  $C_m$  are expressed as

$$C_l = C_{l_o} + C_{l_1} e^{i\omega t} + C_{l_2} e^{i2\omega t} \quad (65a)$$

$$C_m = C_{m_0} + C_{m_1} e^{i\omega t} + C_{m_2} e^{i2\omega t} \quad (65b)$$

where

$$C_{\ell_0} = 2\pi\alpha_0$$

$$C_{\ell_1} = 2\pi \left[ \left( \bar{\alpha} + ik\bar{\alpha} \left( \frac{1}{2} - a \right) + ik\bar{h} \right) C(k) \right. \\ \left. + \frac{ik}{2} \left( \bar{\alpha} - ik\bar{\alpha}a + ik\bar{h} \right) + \sigma\alpha_0 \left( 1 + C(k) + \frac{ik}{2} \right) \right]$$

$$C_{\ell_2} = \sigma 2\pi \left[ - \left( ik\bar{\alpha} \left( \frac{1}{2} - a \right) + ik\bar{h} \right) C(2k) \right. \\ \left. + 2 \left( \bar{\alpha} + ik\bar{\alpha} \left( \frac{1}{2} - a \right) + ik\bar{h} \right) C(k) + ik\bar{\alpha} \right]$$

$$C_{m_0} = \pi\alpha_0 \left( x_m + \frac{1}{2} \right)$$

$$C_{m_1} = \frac{\pi}{2} \left[ 2 \left( x_m + \frac{1}{2} \right) \left( \bar{\alpha} + ik\bar{\alpha} \left( \frac{1}{2} - a \right) + ik\bar{h} \right) C(k) - ik\bar{\alpha} \left( \frac{1}{2} - x_m \right) \right. \\ \left. + k^2 \bar{\alpha} \left( \frac{1}{8} + x_m a \right) - k^2 \bar{h} x_m \right] + \sigma\pi\alpha_0 \left[ \left( x_m + \frac{1}{2} \right) \left( 1 + C(k) \right) + \frac{kx_m}{2} \right]$$

$$C_{m_2} = \sigma\pi \left\{ \left( x_m + \frac{1}{2} \right) \left[ - \left( ik\bar{\alpha} \left( \frac{1}{2} - a \right) + ik\bar{h} \right) C(2k) \right. \right. \\ \left. \left. + 2 \left( \bar{\alpha} + ik\bar{\alpha} \left( \frac{1}{2} - a \right) + ik\bar{h} \right) C(k) \right] - ik\bar{\alpha} \left( \frac{1}{4} - x_m \right) \right\}$$

Let  $U_e(x, t)$  be the total non-dimensional velocity at the surface.

The perturbation velocities for the lifting contributions are related

to the bound vorticity,  $\gamma_a$ , through Equation (19). The bound vorticities are given by (26), (32), (33) and (46), (47), (48). The downwash functions  $B_1(x)$  and  $B_2(x)$  from (57) are substituted into (32) and (33); similarly  $B_c(x)$  from (58) is placed into (47) and (48). The perturbation velocity,  $u_s(x, t)$ , due to the thickness distribution is determined from (53). Since the integral occurring in (53) is given by (61), final expressions for  $u_s$  will not be presented here. The total velocity at the surface is then

$$U_e(x, t) = \left[ 1 + \sigma e^{i\omega t} \pm \frac{1}{2} \left( \frac{C_1(x)}{V_o} e^{i\omega t} + \frac{C_2(x)}{V_o} e^{i2\omega t} + \frac{C_{oc}(x)}{V_o} + \frac{C_{1c}(x)}{V_o} e^{i\omega t} \right) + \frac{u_s(x, t)}{V_o} \right] \quad (66)$$

where the plus and minus signs refer to the upper and lower surfaces respectively and the functions  $C_{oc}(x)$ ,  $C_{1c}(x)$ ,  $C_1(x)$  and  $C_2(x)$ , obtained from Equations (47), (48), (32) and (33) respectively, are given by

$$\frac{C_{oc}(x)}{V_o} = 2\alpha_o \sqrt{\frac{1-x}{1+x}} \quad (67a)$$

$$\frac{C_{1c}(x)}{V_o} = \sigma 2\alpha_o \sqrt{\frac{1-x}{1+x}} \left[ 1 - \frac{2}{\pi [H_1^{(2)}(k) + iH_o^{(2)}(k)]} \int_1^\infty \sqrt{\frac{\lambda+1}{\lambda-1}} \frac{e^{-ik\lambda}}{x-\lambda} d\lambda \right] \quad (67b)$$

$$\frac{C_1(x)}{V_o} = 2 \sqrt{\frac{1-x}{1+x}} \left\{ (\bar{\alpha} + ik\bar{\alpha}(x-a) + ik\bar{\alpha} + ik\bar{h}) \right.$$



$$- \frac{2}{\pi} \frac{\left( \bar{\alpha} + ik\bar{\alpha}\left(\frac{1}{2} - a\right) + ik\bar{h} \right)}{[H_1^{(2)}(k) + iH_0^{(2)}(k)]} \int_1^{\infty} \sqrt{\frac{\lambda+1}{\lambda-1}} \frac{e^{-ik\lambda}}{x-\lambda} d\lambda \quad (68a)$$

$$\begin{aligned} \frac{C_2(x)}{V_0} = & \alpha_2 \sqrt{\frac{1-x}{1+x}} \left\{ \bar{\alpha} + \frac{2}{\pi} \frac{\left( ik\bar{\alpha}\left(\frac{1}{2} - a\right) + ik\bar{h} \right)}{[H_1^{(2)}(2k) + iH_0^{(2)}(2k)]} \int_1^{\infty} \sqrt{\frac{\lambda+1}{\lambda-1}} \frac{e^{-i2k\lambda}}{x-\lambda} d\lambda \right. \\ & \left. - \frac{2}{\pi} \frac{\left( \bar{\alpha} + ik\bar{\alpha}\left(\frac{1}{2} - a\right) + ik\bar{h} \right)}{[H_1^{(2)}(k) + iH_0^{(2)}(k)]} \int_1^{\infty} \sqrt{\frac{\lambda+1}{\lambda-1}} \frac{e^{-ik\lambda}}{x-\lambda} d\lambda \right\} \quad (68b) \end{aligned}$$

### Computational Details

a) The preceding relations for the pressure and velocity contain the well known square root singularity at the leading edge,  $x = -1$ . Both Lighthill's [34] and Riegel's [33] rules are applicable to the present case. Van Dyke [33] compares the two rules and shows for a NACA 0012 airfoil that the results from Riegel's rule are in better agreement with the exact theory as far as the surface velocity is concerned. Hence, Riegel's rule is used in the present work to handle the leading edge singularity. Briefly, the empirical correction is applied by multiplying the velocity by the factor  $\cos \theta$  where  $\tan \theta$  is the slope of the surface. This would correct the pressure formulas also since the singularity appears in these equations through the  $\gamma_a$  term of Equation (36).

b) The second remark is concerned with the numerical evaluation of the wake integrals that appear in Equations (67) and (68). These improper integrals are of the type

$$\frac{1}{\pi} \int_1^{\infty} \sqrt{\frac{\lambda+1}{\lambda-1}} \frac{e^{-ik\lambda}}{x-\lambda} d\lambda \quad (-1 \leq x < 1)$$

The square root singularity at the lower limit is removed by the transformation

$$\lambda = \cosh \eta$$

giving

$$\frac{1}{\pi} \int_0^{\infty} \frac{(\cosh \eta + 1)}{(x - \cosh \eta)} e^{-ik \cosh \eta} d\eta$$

The above form is still inconvenient for purposes of numerical integration since for large values of  $\eta$  the integrand tends to oscillate without any decrease in the amplitude. To overcome this difficulty the integral

$$\frac{1}{\pi} \int_0^{\infty} e^{-ik \cosh \eta} d\eta$$

is added to and subtracted from the original transformed integral

giving

$$- \frac{(1+x)}{\pi} \int_0^{\infty} \frac{e^{-ik \cosh \eta}}{\cosh \eta - x} d\eta - \frac{1}{\pi} \int_0^{\infty} e^{-ik \cosh \eta} d\eta$$

The integral on the right has been shown by Theodorsen [19] to have the value

$$- \frac{1}{2} [Y_0(k) + i J_0(k)]$$

Thus

$$\frac{1}{\pi} \int_1^{\infty} \sqrt{\frac{\lambda+1}{\lambda-1}} \frac{e^{-ik\lambda}}{x-\lambda} d\lambda = - \frac{(1+x)}{\pi} \int_0^{\infty} \frac{e^{-ik \cosh \eta}}{\cosh \eta - x} d\eta + \frac{1}{2} [Y_0(k) + i J_0(k)]$$

where  $J_0$  and  $Y_0$  are Bessel functions of the first and second kind res-

pectively. The integral on the right can now be evaluated numerically without any difficulty. The actual integration is carried out by employing the Gauss -Legendre quadrature [37].

## CHAPTER III

### BOUNDARY LAYER ANALYSIS

The pressure distribution from the previous chapter is assumed to be impressed on the unsteady boundary layer, the solution of which yields the skin friction and hence, the drag acting on the airfoil. This chapter gives the details about the following: the implicit finite difference scheme used to solve the unsteady boundary layer equations; the flow in the vicinity of the stagnation point; the analysis of the laminar flow region; the determination of the transition point; the profile at the first turbulent station; and, the analysis of the turbulent flow region.

#### General Considerations

##### Method of Solution

The boundary layer can be analyzed by either a numerical technique (such as a finite difference scheme) or by the solution of a set of moment-of-momentum integral equations. For the general solution of non-steady boundary layers the integral method has been employed, for the laminar case, by Schuh [38], Rozin [39] and Presz and Heiser [40], and for the turbulent flow situation by McDonald and Shamroth [41].

Unlike finite difference techniques, integral methods involve the assumption of a suitable velocity profile family. Secondly, in contrast to the steady flow situation for which several integral techniques have been explored thoroughly, the number of applications to the unsteady

case remain very few, thus making it difficult to ascertain their reliability in predicting the behavior of non-steady boundary layers. Because of these two reasons the present work uses an appropriate finite difference scheme. It must be pointed out that in general, compared to integral techniques finite difference methods consume more time and may also require larger amounts of computer memory.

Finite difference calculations of time-dependent boundary layers around oscillating airfoils have been performed by Crimi and Reeves [42], Scruggs et al. [43] and McCroskey and Philippe [30]. In references [42] and [43] the primary objective is the analysis of airfoil dynamic stall whereas in [30] the emphasis is on the investigation of viscous flow around both stalled and unstalled airfoils. The numerical method of [30] (based on the implicit finite difference scheme of Dwyer [23], [24]) will be used in the present study because it is simple, is more directly applicable to the present situation and, most importantly, permits the rapid solution of the boundary layer equations.

Let  $\xi$  and  $y$  be the dimensionless streamwise and normal boundary layer coordinates respectively, where  $\xi = 0$  is the location of the stagnation point. Both  $\xi$  and  $y$  are non-dimensionalized by the semi-chord  $b$ . The dimensionless time is given by  $\tau = \omega t$  and  $U_e$  is the potential flow velocity at the outer edge of the boundary layer, obtained from Equation (66). The Reynolds number based on the semi-chord and velocity  $V_o$  is denoted by  $Re$ . The dimensionless streamwise and vertical velocities in the boundary layer are denoted by  $u$  and  $v$  respectively, where the non-dimensionalizing factor is  $V_o$ .

Applying the transformation [30]

$$\eta = \sqrt{\text{Re}} \left( \frac{U_e}{2\xi} \right)^{\frac{1}{2}} y \quad (69)$$

to the unsteady boundary layer equations the continuity and momentum equations can be written as

$$\xi \frac{\partial g}{\partial \xi} + \frac{\partial h}{\partial \eta} - \frac{1}{2} [\beta_t - (\beta_x + 1)g] = 0 \quad (70)$$

$$\frac{k\xi}{U_e} \frac{\partial g}{\partial \tau} + \xi g \frac{\partial g}{\partial \xi} + h \frac{\partial g}{\partial \eta} + \beta_t (g-1) + \beta_x (g^2-1) - \frac{1}{2} \frac{\partial}{\partial \eta} \left( \ell \frac{\partial g}{\partial \eta} \right) = 0 \quad (71)$$

where

$$g(\xi, \eta, \tau) = \frac{u}{U_e} \quad (72a)$$

$$h = \sqrt{\text{Re}} \left( \frac{\xi}{2U_e} \right)^{\frac{1}{2}} v + \frac{\eta}{2} [\beta_t + (\beta_x - 1)g] \quad (72b)$$

$$\beta_x = \frac{\xi}{U_e} \frac{\partial U_e}{\partial \xi} \quad ; \quad \beta_t = \frac{k\xi}{U_e^2} \frac{\partial U_e}{\partial \tau} \quad (72c)$$

$$\ell = 1 + \frac{\epsilon}{\nu} \quad (72d)$$

$\epsilon$  and  $\nu$  being the eddy and kinematic viscosities respectively ( $\ell = 1$  for laminar flow). Except for a slight change in notation the above equations are precisely the same as those in reference [30]. The advantages of working with the transformed equations are [44]: 1) stagnation point conditions can be obtained by taking the limit  $\xi \rightarrow 0$ ; and, 2) the laminar boundary layer thickness is very nearly constant in the transformed coordinates. For the turbulent case the time-dependent untransformed equations corresponding to Equations (70) and (71) have been derived and discussed in reference [41].

### Finite Difference Scheme

As mentioned earlier, the basic numerical scheme used is that of Dwyer [23], [24]. While only a brief description of the scheme is given here the actual difference representations and the final difference equations corresponding to Equations (70) and (71) are presented in Appendix A. References [23], [24] and [30] should be consulted for further details.

The scheme allows for variable step sizes in all the three directions  $\xi$ ,  $\eta$  and  $\tau$ . Whereas the variability in the  $\xi$  and  $\tau$  directions is arbitrary, the step sizes for adjacent points in the  $\eta$  direction are related by

$$\frac{\Delta\eta_{j+1}}{\Delta\eta_j} = r \quad (73)$$

where  $\Delta\eta_j = \eta_j - \eta_{j-1}$ ,  $j$  is the index for the  $\eta$  grid location and  $r$  is a constant which is equal to or slightly greater than unity. Backward differences are used for the  $\xi$  and  $\tau$  derivatives while the  $\eta$  derivatives are represented by central differences. The nonlinear terms are linearized by the use of previous  $\xi$  values. For the laminar case,  $\ell = 1$ , the Crank-Nicolson [25] method is used. A fully implicit scheme is used for the turbulent case where  $\ell$  is variable and iterations on the transport properties are required at each  $\xi$  station. In both cases the final set of simultaneous difference equations to be solved have a tri-diagonal matrix form and are solved rapidly by a standard algorithm [37].

Note that  $U_e$ ,  $\beta_x$ ,  $\beta_t$  are obtained from the potential flow results. The longitudinal pressure gradient parameter,  $\beta_x$ , is obtained

by a simple backward difference formula applied to  $U_e$ . Differentiation of  $U_e$  with respect to time gives the unsteady pressure gradient parameter,  $\beta_t$ .

### Procedural Outline

At any particular time the overall procedure for computing the flow quantities is as follows. The stagnation point is located by noting at what value of  $\xi$  the potential velocity changes sign. Next, the velocity profile in the vicinity of the stagnation point is found by taking the limit  $\xi \rightarrow 0$  in Equations (70) and (71). The finite difference technique allows the flow quantities at a particular  $\xi$  station to be computed from the conditions at the previous  $\xi$  station; this involves the solution of the tridiagonal matrix in the  $\eta$  direction. At each  $\xi$  station a check is made, using an appropriate transition criteria, whether or not the flow has become turbulent. If the flow is still laminar the same procedure is carried out for the next  $\xi$  station. However, if the transition criteria indicates that the flow should no longer be laminar an initial turbulent velocity profile is constructed. Using this profile the flow quantities at the next turbulent station are then computed; this involves several iterations on the transport properties, which means that, whereas, in the laminar case the tridiagonal system was solved only once, now the system has to be solved as many times as the number of iterations. The computations are terminated at a small distance away from the trailing edge.

The skin friction at each  $\xi$  station is found by employing a parabolic fit through the computed velocity values near the airfoil surface.



The unsteadiness in the flow requires the specification of initial conditions in  $\tau$ . Following McCroskey and Philippe [30], this was taken care of by starting the computations at a time when  $\int \beta_t^2 d\xi$  was a minimum and suppressing the  $(\partial g / \partial \tau)$  term in Equation (71). In almost all of the cases considered half a cycle of oscillation was sufficient to damp out the small error that was introduced by the above approximation. The error damped out slightly faster when the above procedure was used as compared to the situation in which the computations were started at an arbitrary value of  $\tau$ .

#### Detailed Considerations

The remainder of this chapter contains details about the flow in the vicinity of the stagnation point, computations in the laminar flow region, transition point determination, the construction of the profile at the first turbulent station, and computations in the turbulent flow region.

#### Stagnation Point Profiles

In the vicinity of the stagnation point,  $\xi = 0$ , the potential flow velocity can be represented [45] by

$$U_e = A\xi \quad (74)$$

where  $A$  is independent of  $\xi$ . Near  $\xi = 0$  the pressure gradient parameters then become

$$\left(\beta_x\right)_0 = 1 \quad ; \quad \left(\beta_t\right)_0 = \frac{k}{A} \left(\frac{1}{U_e} \frac{\partial U_e}{\partial \tau}\right)_{\xi \rightarrow 0} \quad (75)$$

Once the stagnation point has been located,  $A$  in Equation (74) can be

evaluated by a simple difference formula, since  $\left(\frac{\partial U_e}{\partial \xi}\right) = A$ .

In the neighborhood of the point  $\xi = 0$  Equations (70) and (71) then reduce to

$$\frac{\partial h}{\partial \eta} - \frac{1}{2} \left[ \left( \beta_t \right)_0 - 2g \right] = 0 \quad (76)$$

$$\frac{k}{A} \frac{\partial g}{\partial \tau} + h \frac{\partial g}{\partial \eta} + \left( \beta_t \right)_0 (g-1) + (g^2-1) - \frac{1}{2} \frac{\partial^2 g}{\partial \eta^2} = 0 \quad (77)$$

where  $k$  has been taken equal to unity since the flow is laminar and  $h$ , Equation (72b), is now

$$h = \sqrt{\text{Re}} \left( \frac{1}{2A} \right)^{\frac{1}{2}} v + \frac{\eta}{2} \left( \beta_t \right)_0$$

The finite difference scheme described earlier is used to solve the above two differential equations. The constant  $r$ , Equation (73), is taken to be equal to unity (which implies equal spacing in the  $\eta$  direction). The resulting tridiagonal matrix form for Equation (77) and the difference representation of (76) are given in Appendix B.

Note that the unknowns  $g$  and  $h$  have to be obtained by a simultaneous solution of Equations (76) and (77). This requires an iterative procedure. The momentum equation (77) is solved first, for  $g$ , with the steady flow Hiemenz stagnation profiles [45] as inputs. Next,  $h$  is computed from Equation (76) using the calculated  $g$ . The  $g$  and  $h$  thus determined are substituted back into Equation (77) and the same procedure is carried out several times. It was found that five such iterations were sufficient for satisfactory convergence — the difference between the skin friction values from the first and fifth iterations

being less than one percent of the latter value and, the corresponding percentage difference between the fifth and tenth iterations being 0.002.

#### Details-Laminar Region

The Crank-Nicolson [25] method of differencing was employed to solve the laminar boundary layer equations. The resulting set of difference equations which is in the tridiagonal form is given in Appendix A.

The constant  $r$ , Equation (73), was taken to be equal to unity, which implies equal spacing in the  $\eta$  direction. For all the cases considered, the analysis of the laminar region was carried out with 65 points in the vertical,  $\eta$ , direction and with a constant step size,  $\Delta\eta$ , of 0.1.

The number of time steps per cycle of oscillation and the number of points in the streamwise direction depend on whether the boundary layer becomes turbulent or not. For the cases where transition does take place the relevant details are given in the section about the turbulent flow analysis. When the boundary layer remains laminar the computations were carried out with 20 equal time steps per cycle of oscillation and for a total (upper and lower surfaces) of 45 streamwise points. Non-uniform streamwise step sizes were used, the spacing near the stagnation point being closer as compared to the spacing for points farther downstream.

At any one time step the calculations are terminated at the streamwise location where the wall shear vanishes. Due to the unsteadiness in the flow this location keeps shifting. Consider the situation

where, for increasing time, the point of zero wall shear tends to move downstream. At time  $\tau_1$  let the location of this point be  $\xi_1$ . At a time  $(\tau_1 + \Delta\tau)$  let the corresponding location be  $\xi_2$ . The case being considered is when  $\xi_2$  is downstream of  $\xi_1$  (this could happen if the airfoil angle of attack is decreasing with increasing time). To compute the unknown flow quantities at time  $(\tau_1 + \Delta\tau)$  the finite difference scheme requires conditions at time  $\tau_1$ , which are not available for locations that are downstream of  $\xi_1$ . In order to proceed with the calculations the computer program is so constructed that, at time  $(\tau_1 + \Delta\tau)$ , for all  $\xi$ 's downstream of  $\xi_1$  the scheme uses the values of flow variables that are available at a previous time, say  $(\tau_1 - \Delta\tau)$ , instead of the values at time  $\tau_1$ .

#### Transition Point Location

For two-dimensional incompressible flows there are several, mostly empirical, methods [27], [42], [46], [47] available for predicting transition due to the growth of laminar instabilities. However, none of the methods take into account unsteady effects. To the author's knowledge there does not exist a method that claims to be able to predict the transition point for time-dependent flows.

Michel's method [27], [46], [47] is employed in the present work both because of it's success in predicting the transition location for profile drag calculations [48] and it's ease to use. The method is applied to the present unsteady situation by using instantaneous values for the relevant parameters. This implies that the determination of the transition point is based on a quasi-steady assumption. The method assumes that the variation of the transition momentum thickness Reynolds

number,  $R_{\theta_{tr}}$ , with the Reynolds number based on the distance along the airfoil,  $R_{\xi}$ , is a "universal" curve. This empirical transition curve is described in reference [46] as

$$R_{\theta_{tr}} = 1.174 \left[ 1 + \left( 22,400/R_{\xi} \right) \right] R_{\xi}^{0.46} \quad \left( 0.1 \times 10^6 \leq R_{\xi} \leq 40 \times 10^6 \right) \quad (78)$$

where

$$R_{\theta_{tr}} = \left( \theta_{tr} U_e \right) Re \quad ; \quad R_{\xi} = \left( \xi U_e \right) Re$$

and the non-dimensional momentum thickness is defined by

$$\theta = \int_0^{\infty} \frac{u}{U_e} \left( 1 - \frac{u}{U_e} \right) dy$$

Transition can also occur by the mechanism of a laminar separation bubble in which the laminar boundary layer separates followed then by transition and subsequent reattachment of the flow in the turbulent state. For an NACA 0012 airfoil, static calculations [30] show that for angles of attack  $\gtrsim 6.5^\circ$  transition by the growth of laminar instabilities is preceded by laminar separation; a bubble analysis is then required. There exist several bubble analyses (listed in reference [30]) that attempt to predict the bubble characteristics. However, as pointed out in reference [30], even for the case of a static NACA 0012 airfoil the results from the various analyses vary considerably when the same situation is considered for all the methods. Apart from the basic complexity of the phenomena involved, the introduction of unsteadiness in the flow would further complicate the situation. It was, therefore, decided to exclude from the present work transition by the mechanism of a separation bubble.

### Profile at the First Turbulent Station

At the transition point an initial turbulent profile is required in order to proceed with the computations. Scruggs et al. [43] obtain the initial conditions based on the assumption of steady flow over a flat plate. Following Dwyer et al. [24], McCroskey and Philippe [30] approximate the velocity profile by matching up a power law profile with a linear viscous sublayer. Such a procedure requires the specification of three parameters: the boundary layer thickness,  $\delta$ ; the local skin friction coefficient,  $C_f$ ; and the power law exponent,  $n$ . In both references [24] and [30] it is admitted that the selection of the parameters may be quite difficult in certain cases. Dwyer et al. [24] suggest using flat plate data, in terms of the Reynolds number based on the distance along the airfoil, to determine the three parameters. McCroskey and Philippe [30] consider transition by the laminar separation bubble and choose the parameters on an empirical basis while reflecting, at the same time, the local reattachment conditions. They mention an error reducing iterative process that is carried out on the initial  $g$  and  $h$  profiles but do not give any details.

Dwyer et al. [24] consider only steady flow situations. However, in references [43] and [30] the respective procedures are applied to time-dependent cases, which means that the quasi-steady assumption is implicit in their selection of the initial profile. This is not surprising considering the high complexity of the problem which involves unsteady transition near a suction peak. Obviously, a considerable amount of both theoretical and experimental analysis is needed in order to provide a reliable and accurate method for the determination of the

initial profile.

In the present work, following Dwyer et al. [24], the profile is represented by a power law and a linear viscous sublayer. The procedure by which the three parameters,  $\delta$ ,  $C_f$ , and  $n$ , are obtained in the present case is described below.

For a flat plate it is known that at the transition point the laminar and turbulent momentum thicknesses are approximately equal to each other, that is, the momentum thickness is continuous along the plate. Further, at transition the shape factor,  $H$ , (defined as the ratio of the displacement thickness,  $\delta^*$ , to the momentum thickness,  $\theta$ ) drops from a laminar value of 2.6 to 1.4 in the turbulent regime. Details about these experimental observations are given in references [49] and [45] respectively.

For the general computation of turbulent boundary layers it is usually assumed, even when the pressure gradient is non-zero, that the momentum thickness is continuous at the transition point [45], [49], [50].

In light of the preceding remarks and due to the severe lack of data about this complex phenomenon the present work assumes the following: 1) the momentum thickness,  $\theta$ , is continuous at the transition point; 2) the shape factor,  $H$ , in the turbulent regime at transition has a value of 1.4; and, 3) the skin friction coefficient,  $C_f$ , is given by the flat plate relation

$$C_f = \frac{0.0256}{R_\theta^{0.25}} \quad (79)$$

where  $R_\theta = (\theta U_e) \text{Re}$ , and  $\theta$  is fixed by the first assumption.

Describing the profile by a linear viscous sublayer and a power

law

$$\frac{u}{u_\tau} = (y u_\tau) \text{Re} \quad (y \leq y_t) \quad (80a)$$

$$\frac{u}{U_e} = \left(\frac{y}{\delta}\right)^{\frac{1}{n}} \quad (y > y_t) \quad (80b)$$

where  $u_\tau$  is the non-dimensional friction velocity defined by

$$u_\tau = \sqrt{\frac{C_f}{2}}$$

$\delta$  is the dimensionless (with respect to  $b$ ) boundary layer thickness,  $n$  is the power law exponent and  $y_t$  is the ordinate where the linear and power law profiles match.

For arbitrary pressure distributions the assumption of a power law profile results in [49]

$$\delta = \frac{(H+1)H\theta}{(H-1)}$$

which, for the assumed value of 1.4 for  $H$  gives  $\delta = 8.4\theta$ . This fixes the parameter  $\delta$ . The skin friction coefficient,  $C_f$ , is determined by Equation (79), thus fixing the friction velocity,  $u_\tau$ .

Only the power law exponent,  $n$ , remains to be found. Note that the choice of  $n$  has to be consistent with the continuity requirement on  $\theta$ . This provides a way of determining  $n$ . Selecting  $\delta$  and  $C_f$  in the manner described above and with a trial value of  $n$  the corresponding momentum thickness is found from Equations (80). If this thickness is not close enough to the laminar  $\theta$  a new value of  $n$  is chosen. This process is continued until the turbulent  $\theta$  from Equations (80) is very



nearly equal to the laminar  $\theta$ .

The aforementioned procedure completely determines the  $g$  profile at the first turbulent station. The  $h$  profile is still unknown. The continuity equation and certain flat plate relations are employed to determine  $h$ . Actually,  $v$  is determined first and then  $h$  is evaluated from Equation (72b). From the untransformed continuity equation

$$v = - \int_0^y \frac{\partial u}{\partial \xi} dy$$

The  $u$  profile is given by Equations (80), but the integral requires  $\frac{\partial u}{\partial \xi}$  which is in terms of  $\frac{\partial \delta}{\partial \xi}$  and  $\frac{\partial C_f}{\partial \xi}$  (actually,  $\frac{d\delta}{d\xi}$  and  $\frac{dC_f}{d\xi}$  under the present quasi-steady assumption for the profile at the first turbulent station). These derivatives are evaluated using, again, flat plate relations for the respective quantities and the profile of Equations (80). Since the relations employed are well known [45] and the derivation is straightforward the final expressions for  $v$  are not presented here.

#### Details-Turbulent Region

This section contains a description of the turbulence model employed and details about the numerical procedure.

Turbulence Model. The Cebeci-Smith eddy viscosity formulation [26] is used in the present work to model the turbulent boundary layer. This formulation has been thoroughly explored for a wide variety of steady cases and has worked quite well for two-dimensional and incompressible flows. A description of the Cebeci-Smith formulation follows. The boundary layer is regarded as a composite layer consisting of inner

and outer regions [26]. In the inner region the eddy viscosity is given by an expression based on Prandtl's mixing length, taking into account the presence of the wall and non-zero pressure gradients. A constant eddy viscosity expression modified by an intermittency factor is used for the outer region. The two regions are matched by requiring the eddy viscosity to be continuous.

Unsteady flow calculations based on this model have been performed by several investigators [51], [42], [30], [52]. In all of these computations the extension of the model to time-dependent flows has been accomplished by a straightforward generalization of the relevant quantities. This involves using the instantaneous values of the potential flow velocity, the displacement and the boundary layer thicknesses, and incorporating the unsteady term,  $\frac{\partial U_e}{\partial t}$ , into the pressure gradient modification for the inner region. The various empirical constants present in the eddy viscosity expressions are not, however, modified to account for unsteady effects. As noted by McCroskey and Philippe [30], the physics of the local turbulent field is thus effectively assumed to be quasi-steady. Nevertheless, they conclude from their results that the eddy viscosity model is apparently valid for the frequency range of the airfoil cases considered by them.

In terms of the transformed variables the final eddy viscosity expressions for the inner and outer regions are, respectively (see Equation (72d))

$$\left(\frac{\epsilon}{\nu}\right)_i = \left(2\text{Re } \xi U_e\right)^{\frac{1}{2}} \left[ 0.16 \eta^2 (1 - e^{-K})^2 \frac{\partial g}{\partial \eta} \right] \quad (\eta \leq \eta_o)$$

where

$$K = \left(2\text{Re}\xi U_e\right)^{\frac{1}{4}} \frac{\eta}{26} \left[ \left(\frac{\partial g}{\partial \eta}\right)_{\text{wall}} - 2\eta(\beta_t + \beta_x) \right]^{\frac{1}{2}}$$

and

$$\left(\frac{e}{\nu}\right)_o = \left(\frac{2\text{Re}\xi}{U_e}\right)^{\frac{1}{2}} \left[ \frac{0.0168 U_e \int_0^{\infty} (1-g)d\eta}{1 + 5.5 \left(\frac{\eta}{\bar{\delta}}\right)^6} \right] \quad (\eta > \eta_o)$$

where  $\bar{\delta}$  is the transformed boundary layer thickness, defined by

$$\bar{\delta} = \left(\frac{\text{Re}U_e}{2\xi}\right)^{\frac{1}{2}} \delta$$

Numerical Procedure. As mentioned earlier, the turbulent boundary layer is analyzed by an implicit scheme, the details and resulting set of difference equations which is in tridiagonal form are given in Appendix A. The remainder of this section contains the following:

a) a description of the iterative process necessary at each turbulent  $\xi$  station; b) some remarks concerning the movement of the transition point; and, c) details about the mesh sizes, number of time steps, etc.

a) Let the  $\xi$  station index at which the quantities are unknown be  $(i+1)$ . Since the eddy viscosity expressions contain terms that have to be evaluated at station  $(i+1)$ , following Dwyer et al. [24], an iterative scheme is used to update these transport properties. The transport properties are calculated based on information at the station  $i$ , and then the boundary layer is solved at the station  $(i+1)$ . The transport properties are then updated and the iterative process continued until satisfactory convergence is obtained. It was found, typi-

cally, that the change in the total drag was less than 0.1% when the number of iterations was increased from three to six. All turbulent flow calculations were performed with four iterations at each  $\xi$  station.

b) The unsteadiness in the flow causes the location of the transition point to change. Therefore, a particular  $\xi$  location which had laminar conditions at a time  $(\tau - \Delta\tau)$  may, at time  $\tau$ , be in the turbulent regime and vice versa. The step sizes in the  $\eta$  direction for the laminar and turbulent boundary layers are quite different from each other, with the turbulent layer having a greater number of points near the wall and, further, in order to proceed ahead in time the numerical scheme requires information at the previous time value. To handle this difference in step sizes a linear interpolation scheme is employed to calculate the corresponding values at the new vertical locations.

c) All computations were performed with the constant  $r$ , Equation (73), equal to 1.025, thus ensuring small steps near the wall and larger ones away from the wall. The first step away from the wall (i.e.  $\Delta\eta_2$ , if  $j = 1$  represents the wall) had a value of 0.005. With this combination of  $r$  and  $\Delta\eta_2$  a total of 210 points in the  $\eta$  direction were required to reach the boundary layer edge for the cases considered. Note that the wall shear is quite sensitive to changes in  $r$  and  $\Delta\eta_2$ . The above values were chosen based on a comparison with the well known [45] skin friction variation for a flat plate and the necessity of minimizing the total computer memory requirements.

The computations were carried out with 40 equal time steps per cycle of oscillation unlike the completely laminar case where only 20 steps were sufficient. The smaller time step for the turbulent case is

necessary if the transition point movement per time step (and hence the change in drag per time step) is to be kept reasonably small and thus avoid large jumps in the drag versus time curve. In almost all the cases considered it was necessary to compute for only 62 time steps (slightly more than  $1\frac{1}{2}$  cycles) to establish periodicity for the drag (i.e. to damp out the errors to a very negligible value).

The number of streamwise locations around the airfoil was kept at 105 (for the completely laminar case there were only 45 such locations). The much greater number of locations is necessary in order to locate the transition point accurately and concurrently, to avoid large jumps in the drag curve. As in the laminar case the locations were spaced at unequal intervals.

## CHAPTER IV

### RESULTS AND DISCUSSION

The previous chapters of this thesis contained an unsteady potential flow development for an oscillating airfoil in a fluctuating free stream and an appropriate unsteady boundary layer analysis. In this chapter numerical results obtained from these analyses are presented together with a discussion of their significance.

#### Potential Flow

By setting  $\sigma = 0$  in the expressions of the linearized, small perturbation potential flow analysis of Chapter IV the case of an oscillating airfoil subjected to a constant free stream can be recovered. For the case of a non-zero  $\sigma$  there do not exist, to the author's knowledge, explicit expressions for the pressure and velocity over the oscillating airfoil; however, the lift and moment relations have been given by Greenberg [18].

The first part of this section contains a comparison of the constant free stream  $C_p$  distribution from Chapter II with the experimental results of Windsor [53]. This comparison is made solely to verify the correctness of the potential flow part of the final computer program. The remainder of this section contains the following: 1) comments regarding the extension of the present approach to the case when the airfoil and the free stream frequencies are not the same and, 2) a detailed comparison of the present work with that of Greenberg [18].

### Comparison ( $\sigma = 0$ ) with Windsor's Results

Windsor [53] has made pressure measurements on a two-dimensional NACA 0012 airfoil oscillating (about the quarter chord point) sinusoidally in pitch. Figure 2 shows the calculated and measured  $C_p$ 's at  $\omega t = \frac{\pi}{2}$  radians for  $k = 0.2695$ ,  $\alpha = -0.20^\circ + 4.12^\circ \sin(\omega t)$ . The experimental Reynolds number, based on the chord, was  $0.93 \times 10^6$ .

### Extension of Present Approach to the Case of Different Airfoil and Free Stream Frequencies

In the analysis for the oscillating flat plate it has been assumed that the free stream fluctuations and the airfoil oscillations have the same frequency - (20), (21). If this was not the case then the surface boundary condition (9) would give rise to terms with frequencies that are additive combinations of the individual airfoil and free stream frequencies; these terms would then replace the left hand side of (22a). Note that the approximate solutions for this case could also be obtained by using the procedure given earlier for the situation when the individual frequencies are the same. The constants,  $k_n$ , in (24) would have to be taken as equal to  $\left(\frac{i\omega_n}{V_o}\right)$  where  $\omega_n$ 's are the frequencies that would be present on the left side of (22a). Equation (24) would be valid only if  $\frac{k_n \sigma V_o}{i\omega}$ ,  $\sigma \frac{\omega_n}{\omega}$  in this case, is sufficiently small, where  $\omega$  is the free stream frequency.

### Comparison with Greenberg's [2] Analysis

As noted in Chapter I explicit relations for the lift and moment on an oscillating airfoil in a fluctuating stream have been given earlier by Greenberg [18]. He extends the constant free stream analy-

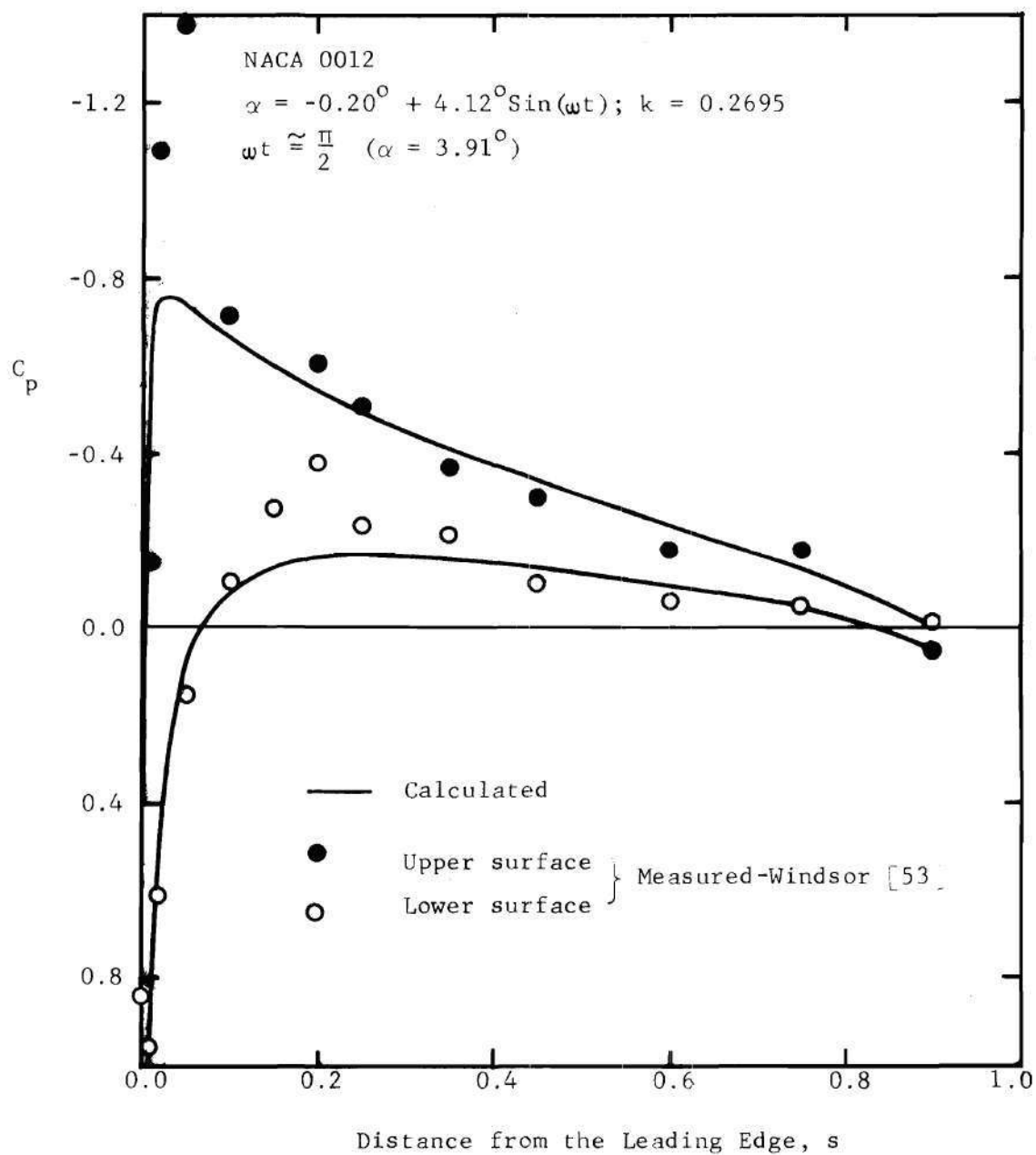


Figure 2. Comparison of Calculated and Measured Pressure Coefficient



sis (based on the technique of conformal transformation) of Theodorsen [19] to take into account variations in the free stream. The Kutta condition is satisfied by requiring the induced velocity at the trailing edge to be finite. Greenberg considers the problem in which the airfoil and stream frequencies are different. He neglects the effect on the wake of the fluctuations in the free stream relative to the mean velocity,  $V_o$  (this has been noted earlier by Ashley et al. [54]). The following remarks which are directly applicable to the case when the airfoil and stream frequencies are the same remain valid for the situation where the frequencies are different.

The present analysis shows that the approximate wake given by (27) neglects terms of order  $\sigma^2$  and higher and consequently, the zero pressure discontinuity condition in the wake, (23a), is not satisfied exactly (error  $\sim \sigma^2$ ). Also, such a wake along with the bound vorticity  $\gamma_a$  given by (26) can be made to satisfy exactly both the trailing edge condition, (23b), and the surface boundary condition, (22a). Greenberg neglects the direct effect of  $\sigma$  on the wake, which is equivalent to replacing  $e^{k_n I(t)}$  by  $e^{k_n V_o t}$  in the expression for  $\gamma_w$  (see development leading to equation (24)). Hence, the wake given by (27) is a better approximation since it takes into account terms that are of order  $\sigma$ .

Surprisingly, even though Greenberg has neglected the direct effect of  $\sigma$  on the wake he does not place any restriction on  $\sigma$ , instead, an attempt is made to justify the assumed wake by taking  $\omega \rightarrow \infty$  (i.e.  $\frac{1}{\omega} \rightarrow 0$ ), whereas, it is evident from (24) that the accuracy of the approximation depends on  $\left(\frac{k_n \sigma V_o}{i\omega}\right)$  and not just  $\left(\frac{1}{\omega}\right)$ . Note that the quantity  $\left(\frac{k_n \sigma V_o}{i\omega}\right)$ , which is assumed to be small, reduces to  $(n\sigma)$   $n = 1, 2$ , and

hence the restriction on  $\sigma$  (when the airfoil and stream frequencies are not equal it would reduce to  $\sigma\left(\frac{\omega_n}{\omega}\right)$  - see previous comment). In fact this restriction on  $\sigma$  can be shown to be true even from equations given in his paper. From a physical viewpoint a restriction on  $\sigma$  seems more plausible than the requirement of having  $\omega \rightarrow \infty$ . This is so because as  $\sigma$  becomes larger and larger (although it still must be less than unity to avoid reverse flow) one would definitely expect  $\sigma$  to have an increasingly direct effect on the wake. Moreover, the condition  $\omega \rightarrow \infty$  would make the assumption of simple harmonic variation,  $e^{i\omega t}$ , questionable since the limit of  $e^{i\omega t}$  as  $\omega \rightarrow \infty$  is not defined.

As far as the  $e^{i\omega t}$  terms are concerned, Greenberg's expressions for the lift and pitching moment for the oscillating flat plate are the same as those that would be derived from the present analysis. This is to be expected since these terms do not depend on  $\sigma$  and represent the constant free stream contribution. The differences between the two wakes are in the  $e^{i2\omega t}$  terms. Specifically, Greenberg's wake does not contain the term corresponding to  $\sigma e^{-ikx} \cdot e^{i2\omega t}$  in (27) (the non-existence of the term being a consequence of the approximation  $e_n^k I(t) \approx e_n^k V(t)$ ) and, the manner in which the wake constants (similar to  $A_1$  and  $A_2$ ) are determined is equivalent in the present procedure to neglecting the  $\sigma e^{i\omega t}$  term in the trailing edge condition for  $\gamma_w$ , (23b). These differences preclude any effect in the wake of the  $e^{i\omega t}$  term on the  $e^{i2\omega t}$  term. Finally, in the equations for the lift and moment Greenberg has certain terms that have a  $\sigma^2$  dependency; these are generated due to the specific way in which the problem has been formulated and not because the wake model takes into account the direct effect of  $\sigma$ .

Greenberg's paper, reference [18], should be consulted for further details on the problem formulation. The effect of the  $\sigma^2$  terms on the accuracy of the final results is not clear.

For the case of a flat plate pitching about the quarter chord point with  $\alpha = 3.5^\circ + 2^\circ \cos(\omega t)$ ,  $k = 0.20$ , and  $\sigma = 0.10$ , the computed lifts and moments from the present analysis and that of Greenberg are given in Table 1. As mentioned earlier, Greenberg's expressions contain terms with  $\sigma^2$  dependency; the coefficients  $C_{l_5}$ ,  $C_{l_6}$ ,  $C_{m_5}$  and  $C_{m_6}$  in the table reflect this dependency. The present analysis, accurate up to order  $\sigma$ , does not contain these coefficients. The identical moment coefficients obtained from the analyses is due to the fact that the flat plate is pitching about the quarter-chord point. If the airfoil were to pitch about some other point the moment coefficients also would be different.

### Skin Friction Comparisons

Before computing the unsteady skin friction for the general case of an oscillating airfoil in a fluctuating free stream certain simpler calculations were carried out. This was done to verify the correctness of the computer program.

Figures 3-5 contain several comparisons for both laminar and turbulent flow. Figure 3 shows the presently calculated and experimentally determined [55] steady state skin friction for a NACA 0012 airfoil at zero incidence in a flow with a chordal Reynolds number of  $2.675 \times 10^6$ . The location marked T denotes the experimental transition point. The turbulent computations were initiated at this point, with the initial profile determined by the procedure described in the previous chapter. The

Table 1. Lift and Moment Comparisons

Flat plate airfoil pitching about the quarter chord point

$$\alpha = 3.5^\circ + 2^\circ \cos \omega t; k = 0.20; V = V_0(1 + 0.1 \cos(\omega t))$$

$$C_l = C_{l_0} + C_{l_1} \sin \omega t + C_{l_2} \cos \omega t + C_{l_3} \sin 2\omega t + C_{l_4} \cos 2\omega t + C_{l_5} \sin 3\omega t + C_{l_6} \cos 3\omega t$$

$$C_m = C_{m_0} + C_{m_1} \sin \omega t + C_{m_2} \cos \omega t + C_{m_3} \sin 2\omega t + C_{m_4} \cos 2\omega t + C_{m_5} \sin 3\omega t + C_{m_6} \cos 3\omega t$$

<u>Lift</u>	$C_{l_0}$	$C_{l_1}$	$C_{l_2}$	$C_{l_3}$	$C_{l_4}$	$C_{l_5}$	$C_{l_6}$
Present	0.3838	-0.0091	0.2320	0.0002	0.0328	See text	
Greenberg	0.3838	-0.0091	0.2320	0.0009	0.0333	0.0004	0.0014
<u>Moment</u>	$C_{m_0}$	$C_{m_1}$	$C_{m_2}$	$C_{m_3}$	$C_{m_4}$	$C_{m_5}$	$C_{m_6}$
Present	0.0	0.0119	0.0008	0.0016	0.0	See text	
Greenberg	0.0	0.0119	0.0008	0.0016	0.0	0.0	0.0

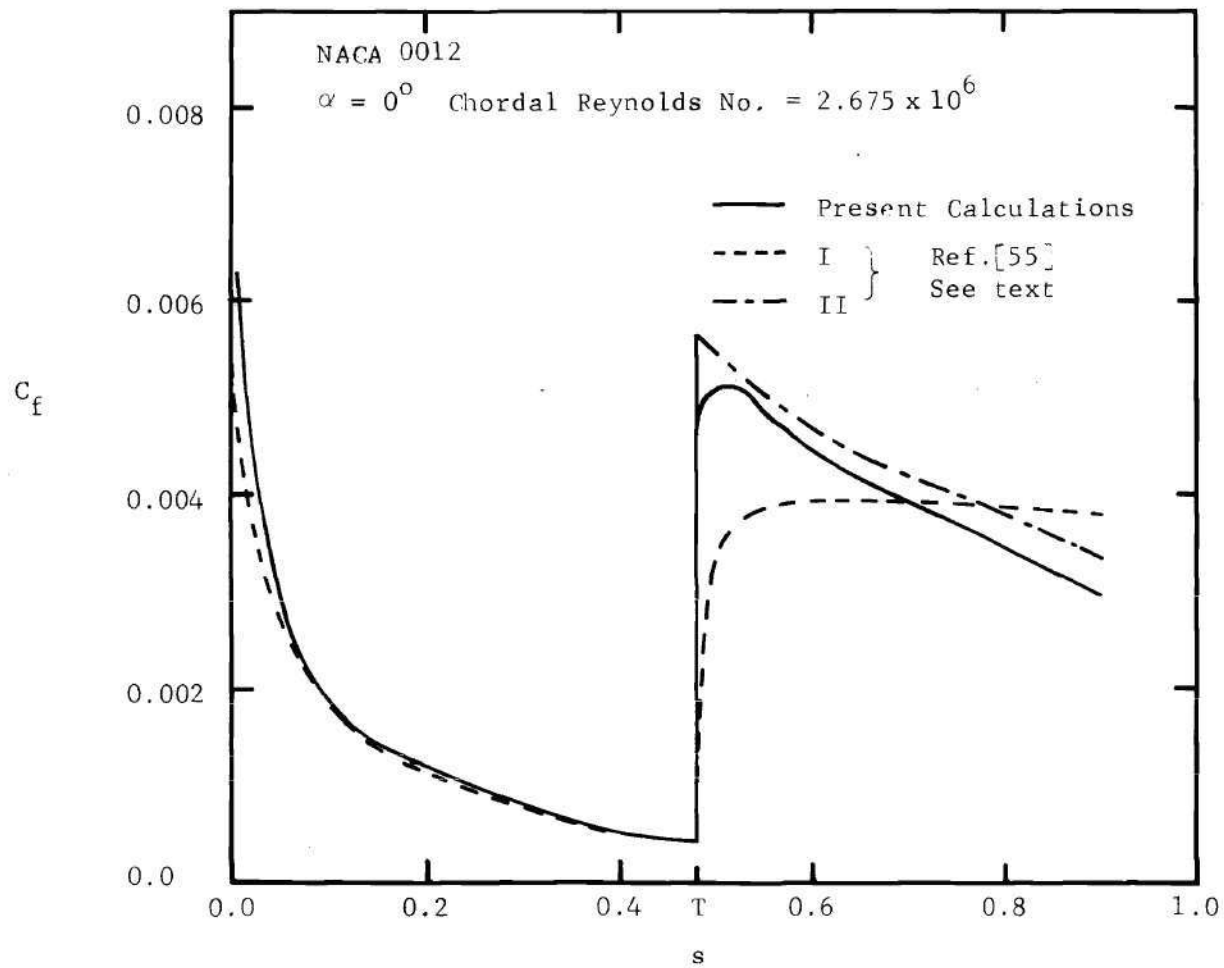


Figure 3. Skin Friction Comparisons for NACA 0012 Airfoil

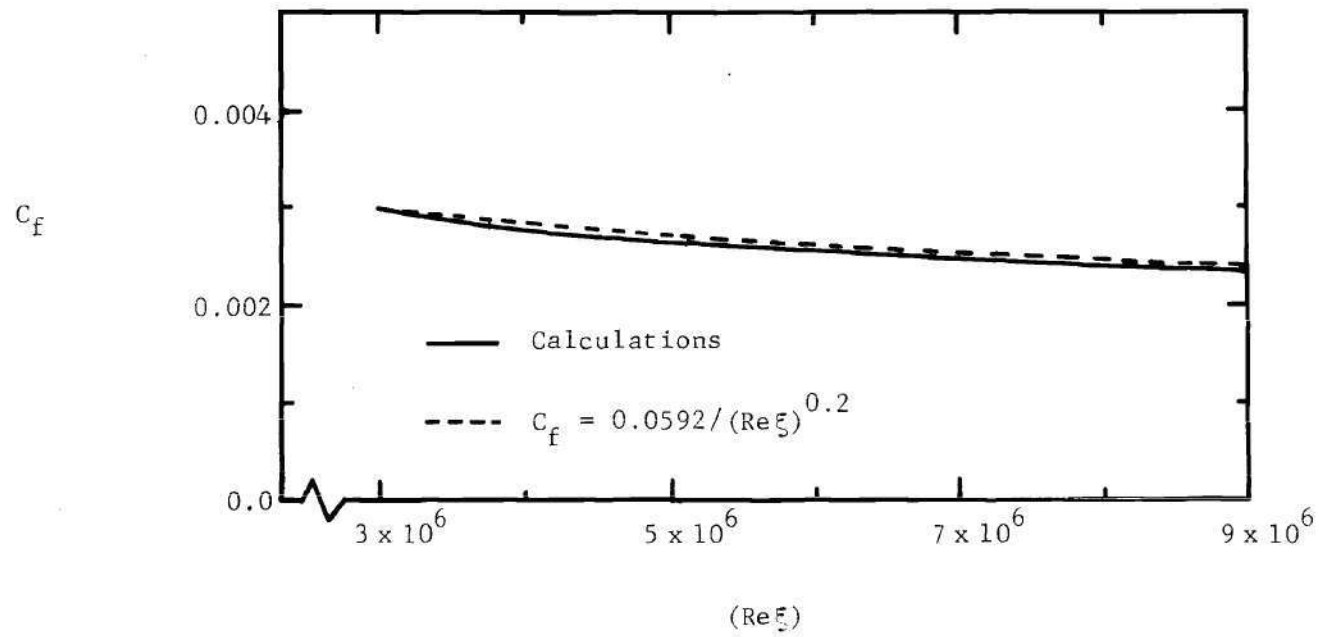


Figure 4. Turbulent Skin Friction for a Flat Plate

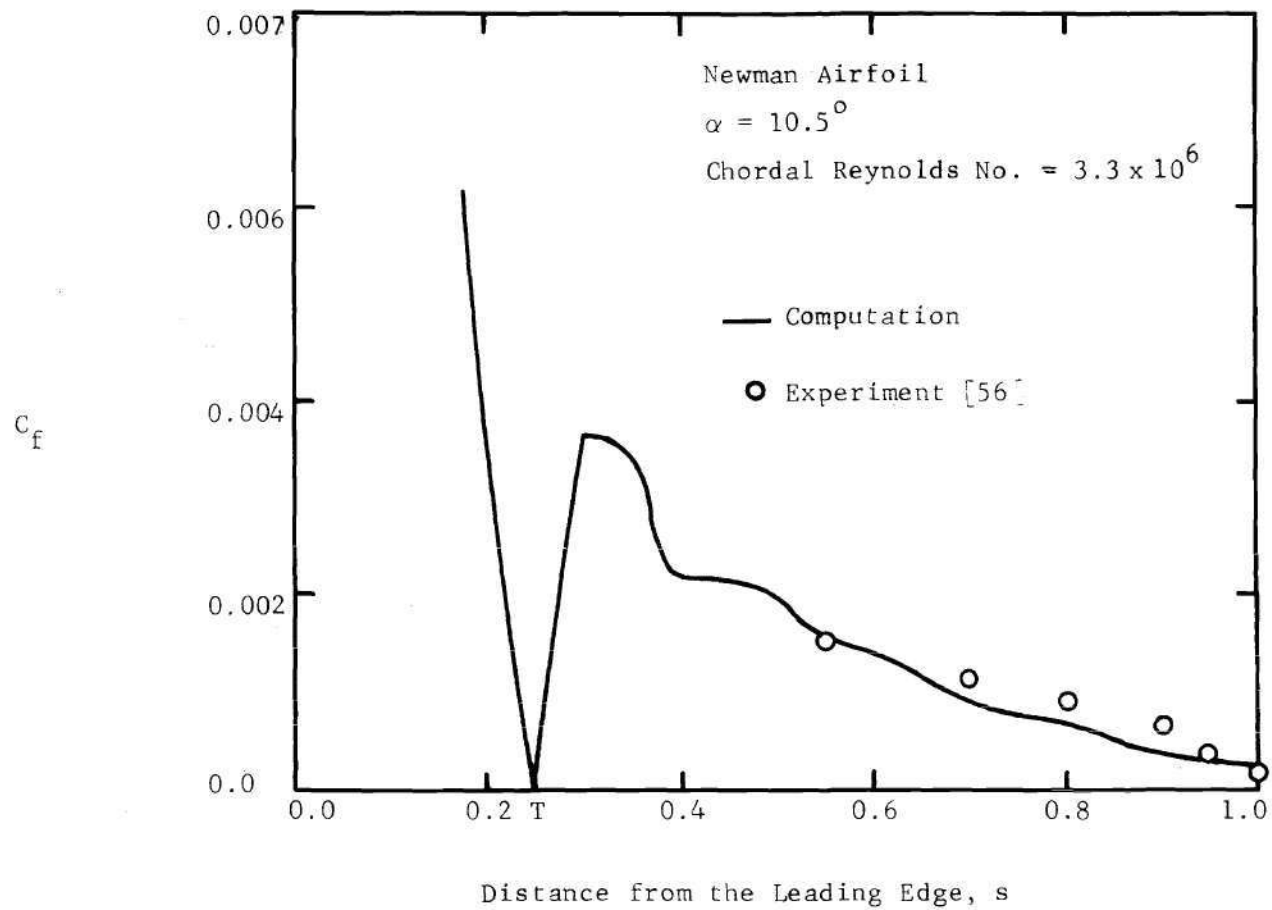


Figure 5. Turbulent Skin Friction Comparison-  
Newman Airfoil

curve labeled I is the experimental  $C_f$  obtained by differentiating the measured velocity profiles. The curve II, also from [55], represents the theoretical turbulent  $C_f$  calculated by an integral technique. As expected, for the laminar region the agreement between the calculated and experimental curves is very good. For the turbulent region, however, the agreement is not good between the present curve and the experimental curve, I; however, the agreement between the present curve and curve II is much better. Note that there exists a lack of agreement between curves I and II. Reference [55] notes the difficulty present in determining an experimental distribution that involves the differentiation of an experimental curve. The total computed skin friction drag coefficient,  $C_d$ , is 0.0057 and the experimental value is 0.0052.

Figure 4 presents the turbulent skin friction for a flat plate at zero incidence. The solid curve represents the computed  $C_f$  and the broken curve was obtained from the well known flat plate formula [45]  $C_f = 0.0592/(\text{Re}\xi)^{0.2}$ . The fully developed flat plate velocity profile was taken as the starting profile for the computations. As expected, the agreement is very good between the curves for this zero pressure gradient situation.

Figure 5 compares the computed turbulent  $C_f$  with the experimental data of Newman [56] for the case of a 20% thick symmetrical airfoil kept at an angle of attack of  $10.5^\circ$ ; the chordal Reynolds number was  $3.3 \times 10^6$ . The experimental transition point is denoted by T, and the turbulent computations were started from this location. Due to the high incidence, transition takes place by the mechanism of a laminar separation bubble. For this reason, in this case, the first turbulent profile was obtained



by a procedure slightly different from that described in the previous chapter. The flat plate relations based on the distance from the stagnation point (instead of the laminar momentum thickness) were employed to fix  $C_f$  and  $\delta$  for the initial profile. The power law exponent,  $n$ , was chosen by computing the skin friction for several choices of  $n$  and then selecting the value that provided the best agreement with the experimental data. The experimental potential flow velocity was utilized in the computations to avoid errors that might have resulted by the application of the small disturbance potential flow analysis for this case of high incidence. Considering the uncertainty in determining the initial turbulent profile, the agreement between the calculations and the experimental data is satisfactory.

McCroskey and Philippe [30] have performed unsteady laminar and turbulent calculations for the case of a flat plate at zero incidence in a fluctuating free stream, where  $U_e = 1 + 0.125 \sin(\omega t)$ . Since the present computational method is basically the same as their scheme the above case is convenient for verifying the correctness of the formulation. The skin friction amplitude and phase (with respect to  $U_e$ ) distributions from [30] were compared with the present results. Complete agreement was obtained for the laminar case. The agreement in the turbulent situation,  $Re = 5 \times 10^6$ , was excellent; the difference between the amplitude distributions being less than 5% and the phases differing by approximately 10%. As noted previously in Chapter III, McCroskey and Philippe mention an error reducing iterative process carried out on the  $g$  and  $h$  profiles at the first turbulent station, but do not give any details. The present approach does not involve such a procedure.

Presumably, the above discrepancies are due to this difference between the two approaches.

### Least Squares Fit for Drag

Once the skin friction distribution is known from the boundary layer analysis the drag at any instant is obtained by integrating the skin friction around the airfoil and then taking the component of the integral in the free stream direction.

It may be recalled that for the potential flow analysis the airfoil oscillations and the free stream fluctuations were assumed to be simple harmonic in time with the same frequency. The resulting pressure (and velocity) was periodic in time with a period of  $2\pi$  radians and, for the constant incidence case was harmonic with only a  $\omega t$  dependency. Introducing oscillations in the airfoil incidence brought in an additional ( $2\omega t$ ) dependency. The shape of the drag curve for such a complex potential flow is not known in advance until the drag computations are completed. However, it is possible to obtain a rough estimate of the drag variation from a simple argument, which is as follows. Let the free stream be of the form  $V_o(1 + \sigma \cos(\omega t))$ . A crude attempt to account for the free stream variations would be to assume a constant drag coefficient, say  $(C_d)_c$ , and express the drag as

$$D = (C_d)_c \cdot \rho b [V_o(1 + \sigma \cos(\omega t))]^2 \quad (81)$$

It can be seen that the above drag is periodic, with a period of  $2\pi$  radians, and, for small values of  $\sigma$ ,  $D$  is very nearly simple harmonic and in phase with the free stream.

Consider now a least squares fit for the drag obtained from the unsteady boundary layer analysis. Let the computed drag coefficient at a time  $\tau (= \omega t) = \tau_m$  be  $C_{d_m}$ ,  $m = 1, 2, \dots, M$ . Further, let the least squares curve be of the form

$$C_d(\tau) = A_o + A_c \cos(\tau + \varphi) \quad (82)$$

The constant  $A_o$  represents the steady component,  $A_c$  the oscillatory amplitude and,  $\varphi$  is the phase difference between  $C_d(\tau)$  and the free stream. The constants  $A_o$ ,  $A_c$  and  $\varphi$  will be obtained in the usual least squares manner [37] by minimizing

$$E = \sum_{m=1}^M [C_{d_m} - C_d(\tau_m)]^2$$

The derivatives  $\partial E / \partial A_o$ ,  $\partial E / \partial A_c$  and  $\partial E / \partial \varphi$  are each set equal to zero and the three constants found by a simultaneous solution of the three resulting equations.

A quantitative measure of the difference between the computed drag curve and the fitted curve (82) would be useful in judging the closeness of the "fit." An appropriate quantity would be

$$\bar{d} = \frac{\sqrt{\sum_{m=1}^M [C_{d_m} - C_d(\tau_m)]^2}}{M} \cdot \frac{100}{A_c} \quad (83)$$

Basically,  $\bar{d}$  is the average departure, expressed as a percentage of the oscillatory amplitude  $A_c$ , of the least squares curve from the computed curve.

For all the cases considered it was found that the computed drag

was periodic with a period of  $2\pi$  radians and the departure  $\bar{d}$  was always less than 2.0.

Throughout the following, unless stated otherwise, all computed drag curves will be fitted by Equation (82), and the constants  $A_o$ ,  $A_c$  and  $\varphi$  determined in the manner described earlier. This is done in order to facilitate the interpretation of the raw results.

As an example, Figure 6 shows the computed drag coefficient for completely laminar flow around an NACA 0012 airfoil with  $\alpha = 2^\circ + 2^\circ \cos(\omega t)$ ,  $(V/V_o) = 1 + 0.1 \cos(\omega t)$ ,  $k = 0.2$ , and  $Re = 10^5$ . The departure  $\bar{d}$ , for this case, was equal to 1.2. The constants  $A_o$ ,  $A_c$  and  $\varphi$  were equal to 0.00519, 0.00064 and  $18.7^\circ$ , respectively. Also shown in the figure is the least squares fitted curve using these constants.

Note that the drag coefficient in the figure is shown for a total time greater than  $2\pi$  radians. As mentioned in the previous chapter, the computations were usually carried out for a total of approximately  $1\frac{1}{2}$  cycles to allow the transients to damp out. The locations marked S and E ( $\omega t = 3\pi$ ) on the abscissa are the points at which the calculations were initiated and terminated respectively. The transient behavior can be observed by comparing the drag coefficients at S and at  $\omega t = \pi$ ; the value at S is slightly greater than the value at  $\omega t = \pi$ . Note that acceptable periodicity has been established for  $\omega t \geq 0$ .

### Laminar Flow Results

The response of the laminar boundary layer to small fluctuations in the free stream has been considered in several studies, of which the analyses of Lighthill [28] and Nickerson [29], and the experiments of Hill and Stenning [31] are of interest in the present work. More re-

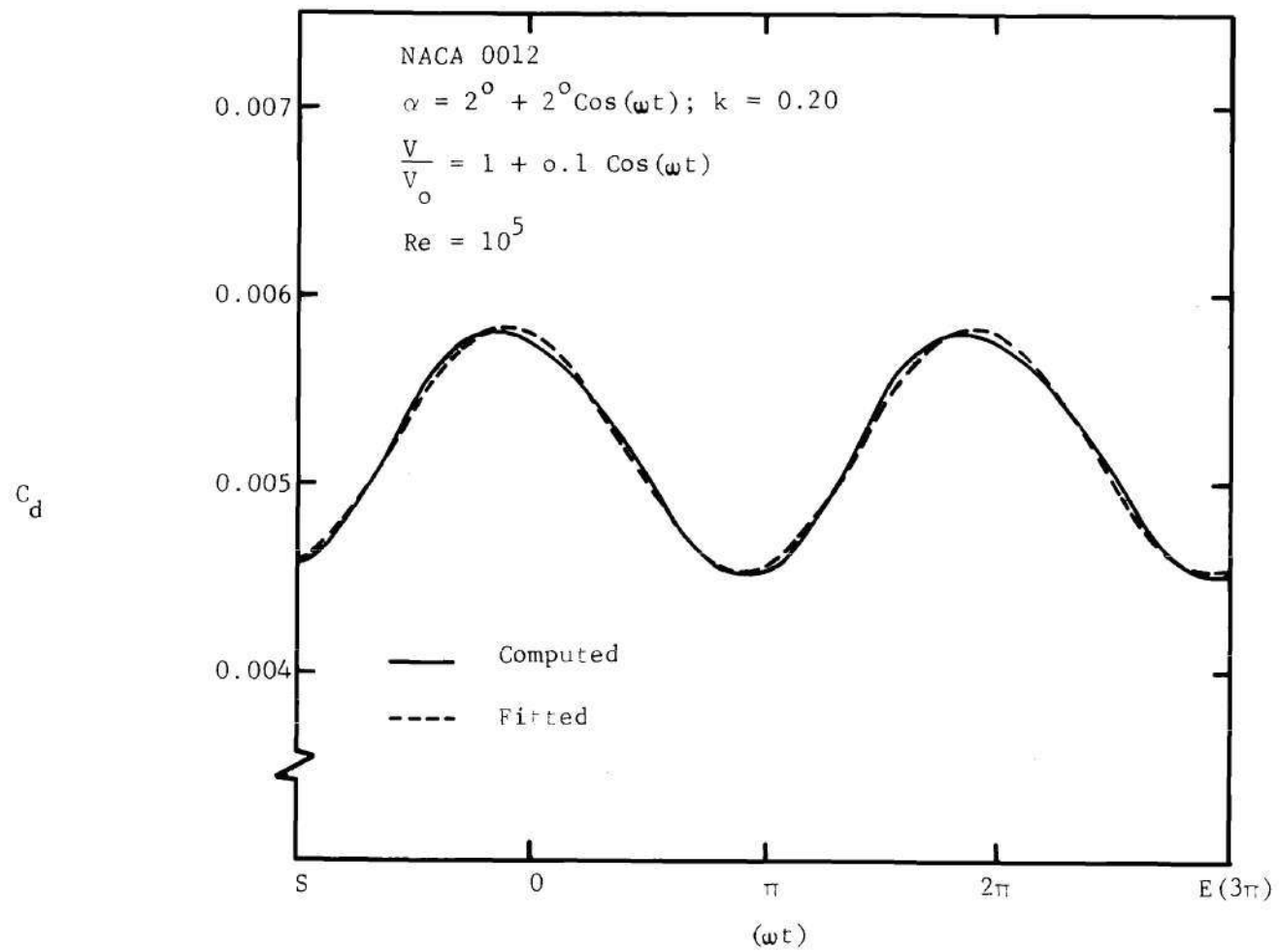


Figure 6. Example of a Computed Drag Curve

cently, Valensi and Rebont [14] and Kunz [15] have attempted to measure the unsteady drag of an airfoil at a constant incidence subjected to a fluctuating free stream.

Lighthill's study shows that unsteady effects strongly influence the skin friction and its phase with respect to the free stream. Valid for flows where the lift is zero and the Karman-Pohlhausen parameter  $\Lambda$  is approximately constant, his analysis reveals that the skin friction fluctuations have a phase advance over the free stream velocity, that is, their maxima anticipate the velocity maxima. Lighthill treats the low and high-frequency cases separately. For each point on the surface there can be identified a crossover or critical frequency,  $\omega_0$ , such that for  $\omega < \omega_0$  (low-frequency) the phase lead is given by  $\tan^{-1}(\omega/\omega_0)$  and, for  $\omega > \omega_0$  (high-frequency) the lead is  $45^\circ$ . A special case where his analysis is directly applicable is that of a flat plate at zero incidence. As noted by McCroskey and Philippe [30] at low frequencies, the unsteady effects for this case are approximately proportional to the local reduced frequency,  $\omega d/V_0$  ( $d$  being the distance from the leading edge), and the Lighthill analysis gives the phase advance as  $\tan^{-1}(1.7\omega d/V_0)$ . Their numerically computed phase curve forms a smooth bridge between Lighthill's low and high-frequency approximations. As noted earlier, the present computations are in complete agreement with McCroskey and Philippe's results. Experimentally, for the flat plate case, Hill and Stenning [31] show that the amplitude and phase values from the Lighthill low-frequency analysis agree well with their measurements in the range  $0 < (\omega d/V_0) < 0.6$ . For the present airfoil computations, considering the range of interest of the reduced frequency,  $k$ ,

it is the low-frequency case that is more relevant.

All airfoil calculations were performed using the NACA 0012 basic thickness form. For the oscillating airfoil the quarter chord point was specified to be the axis of rotation. Typical computer time per run on the CDC 6600 was approximately  $1\frac{1}{2}$  minutes.

#### Comparison with Experimental Data

Valensi and Rebont [14] have performed experiments designed to measure the unsteady drag of an NACA 0012 airfoil at a constant incidence and performing harmonic oscillations parallel to the wind tunnel free stream. Figures 7-9 present the calculated and measured drag curves. As far as the curve shape and the drag magnitudes are concerned the agreement between the two curves is, in all cases, excellent. The calculated drag has a small but definite lead in phase over the free stream velocity; the direction of this phase shift being in agreement with the skin friction phase advance predicted by previous analyses [28], [29] and measurements [31]. Valensi and Rebont's drag curves have, however, a definite phase lag.

Kunz [15] measured the drag of a stationary NACA 0012 airfoil at a non-zero incidence subjected to a fluctuating free stream, where the fluctuations were introduced by a set of rotating vanes mounted downstream of the wind tunnel test section. He relates the free stream fluctuations to an "equivalent in-plane displacement" and then obtains "drag derivatives" with respect to the equivalent displacement. It was found that his drag derivatives were approximately ten times higher than the derivatives obtained through the present computations.

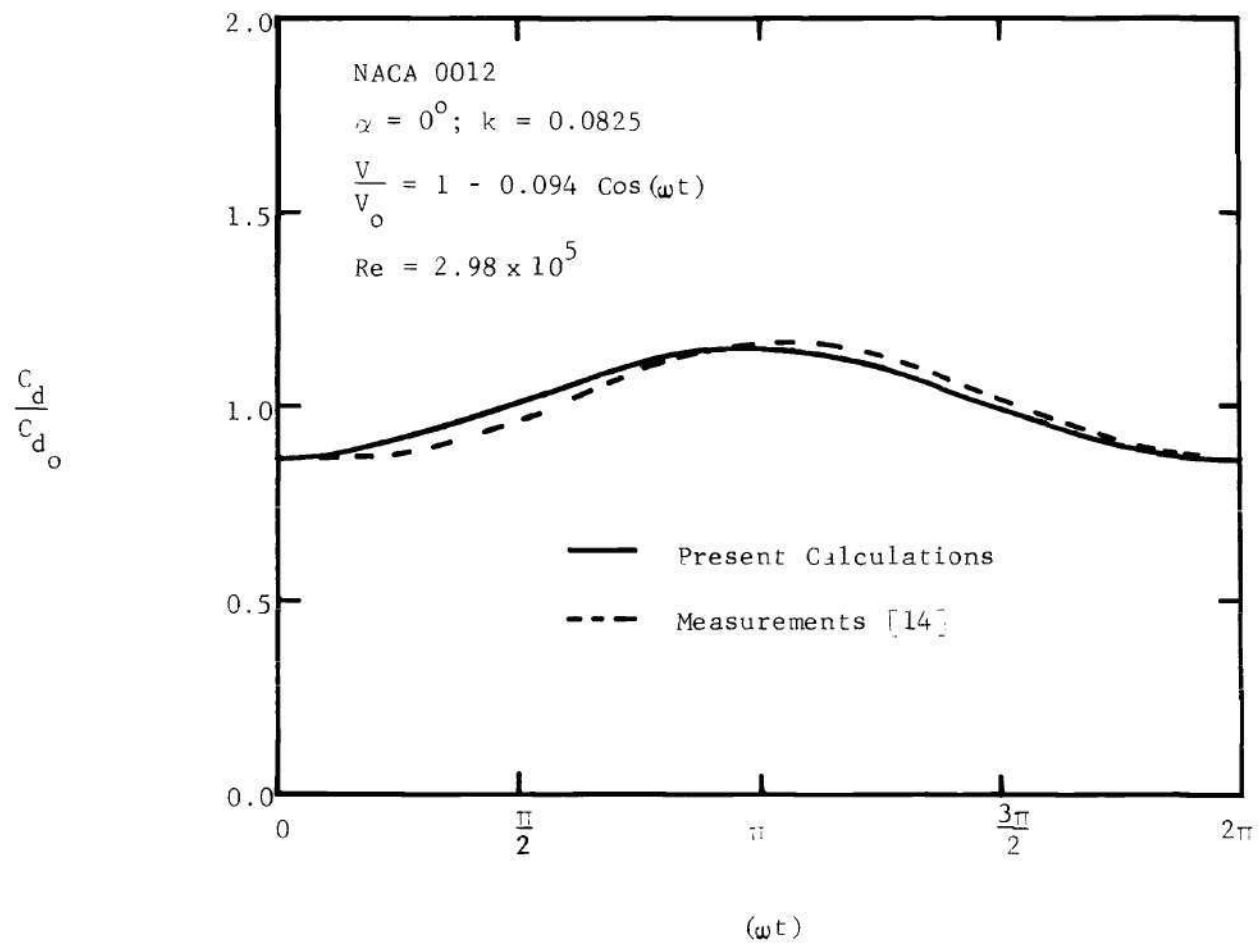


Figure 7. Comparison of Computed and Measured Drags - I



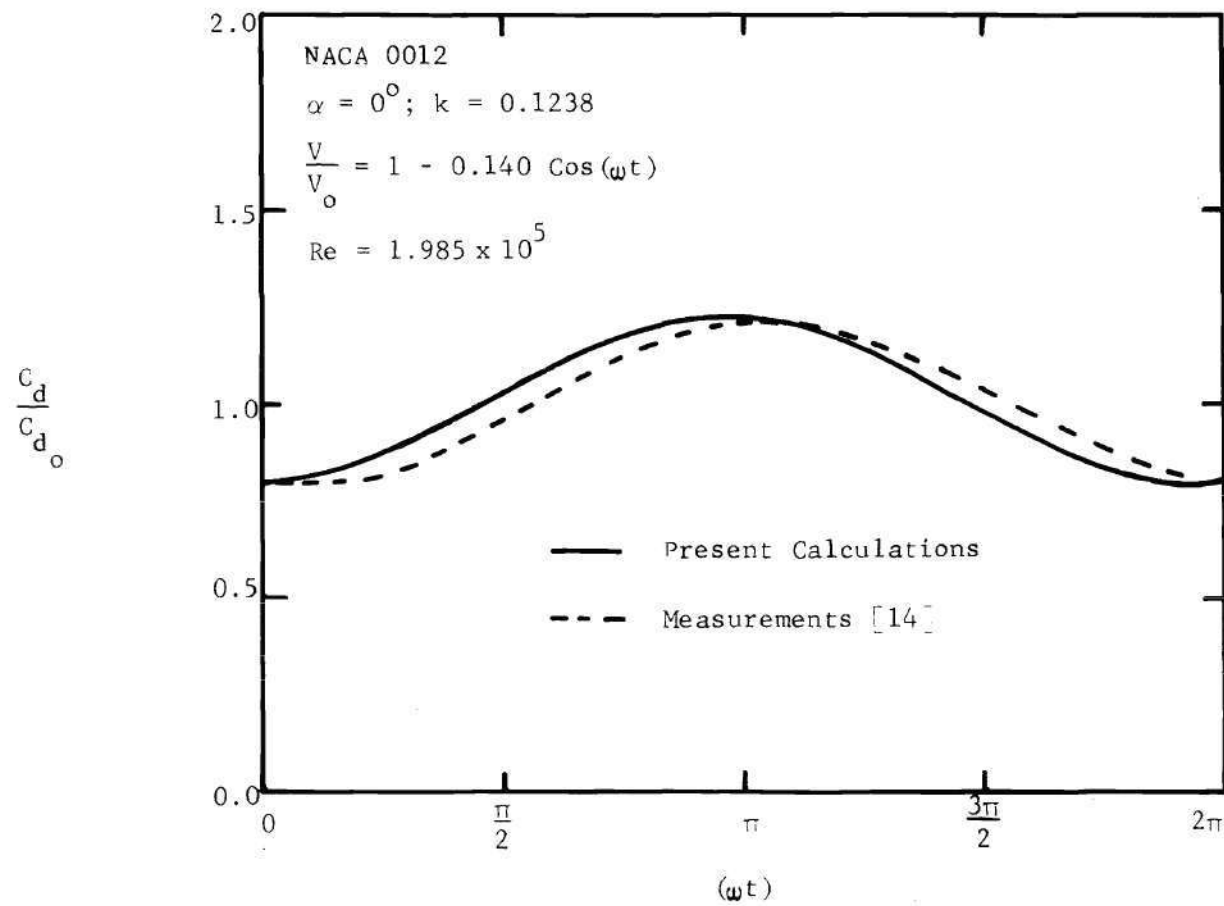


Figure 8. Comparison of Computed and Measured Drags - II

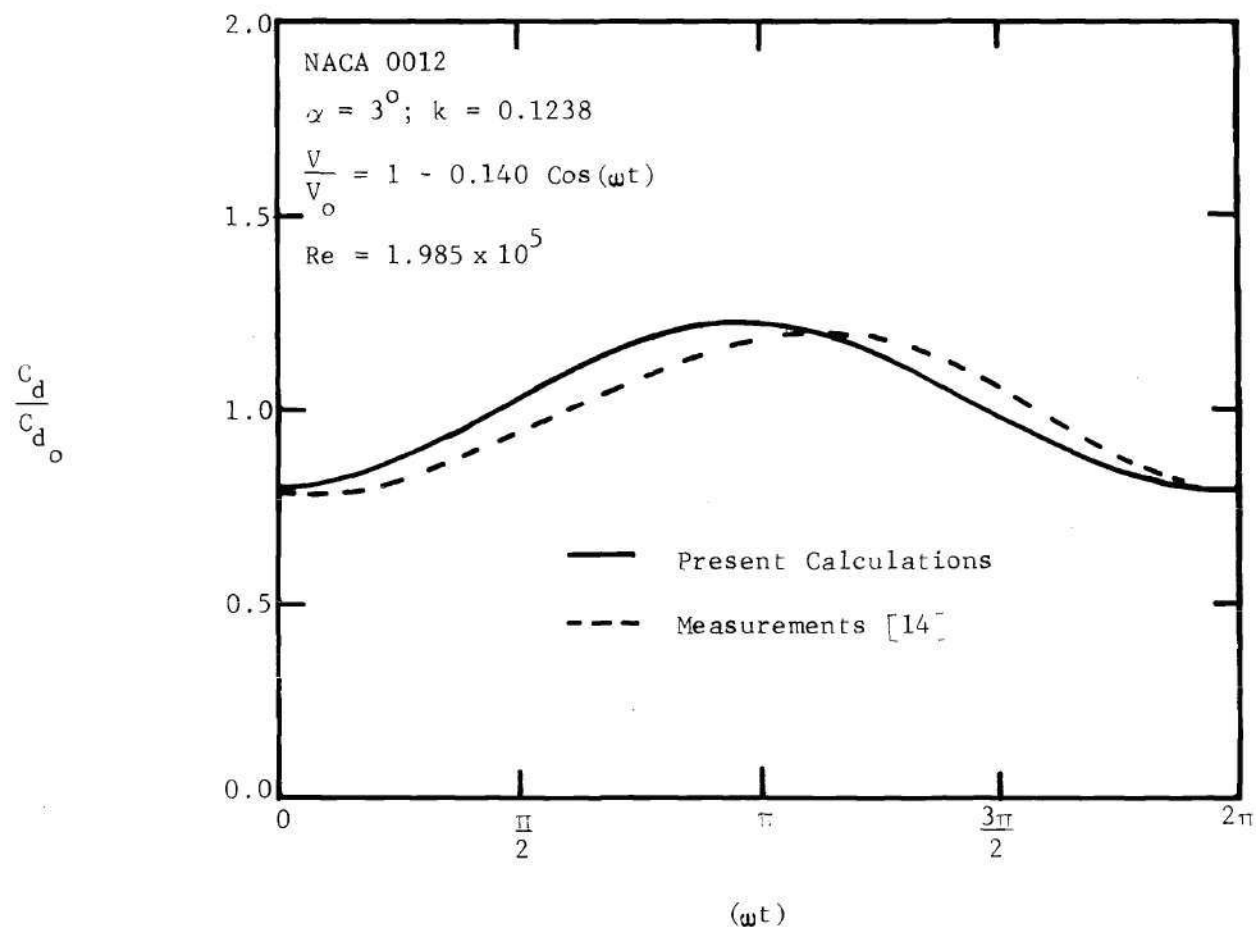


Figure 9. Comparison of Computed and Measured Drags - III

### Effects due to the Amplitude of Free Stream Fluctuations

Figures 10-13 show the effect of  $\sigma$  on the drag.

Shown in Figures 10 and 11a are two sets of computed curves for the stationary and oscillating airfoil cases. For the constant free stream condition,  $\sigma = 0$ , the drag for the former case is, as expected, a constant. The corresponding curve for the oscillating airfoil appears to have a  $\cos(\omega t + \pi - \epsilon)$  type of variation where  $\epsilon \approx \frac{\pi}{9}$  radians. This behavior can be explained by a consideration of the movement of the zero wall shear location, say  $S$ , downstream of which the analysis assumes zero skin friction.

For simplicity, let the reduced frequency be zero. This corresponds to the quasi-steady approximation in which all time derivatives are suppressed and steady state calculations are performed at each instant. At positive angles of attack, compared to the symmetrical case of zero incidence, the upper surface  $S$  moves towards the leading edge and,  $S$  for the lower surface shifts towards the trailing edge, staying close to it throughout most of the cycle. It was found that the total chordwise movement of  $S$  on the upper surface is approximately twice the value for the lower surface. The variation of  $S$  on the upper surface will, therefore, have a greater influence on the changes in the drag. When the angle of attack is maximum this location is nearest to the leading edge as compared to the minimum incidence case when it is farthest. In the former situation the drag will be close to the lowest value for the cycle and in the latter case it would be close to the highest value. The preceding observations show that for oscillations of the type  $\alpha = \alpha_o + \alpha_r \cos(\omega t)$ ,  $\alpha_o \geq \alpha_r$ , the drag would be  $\pi$  radians off phase

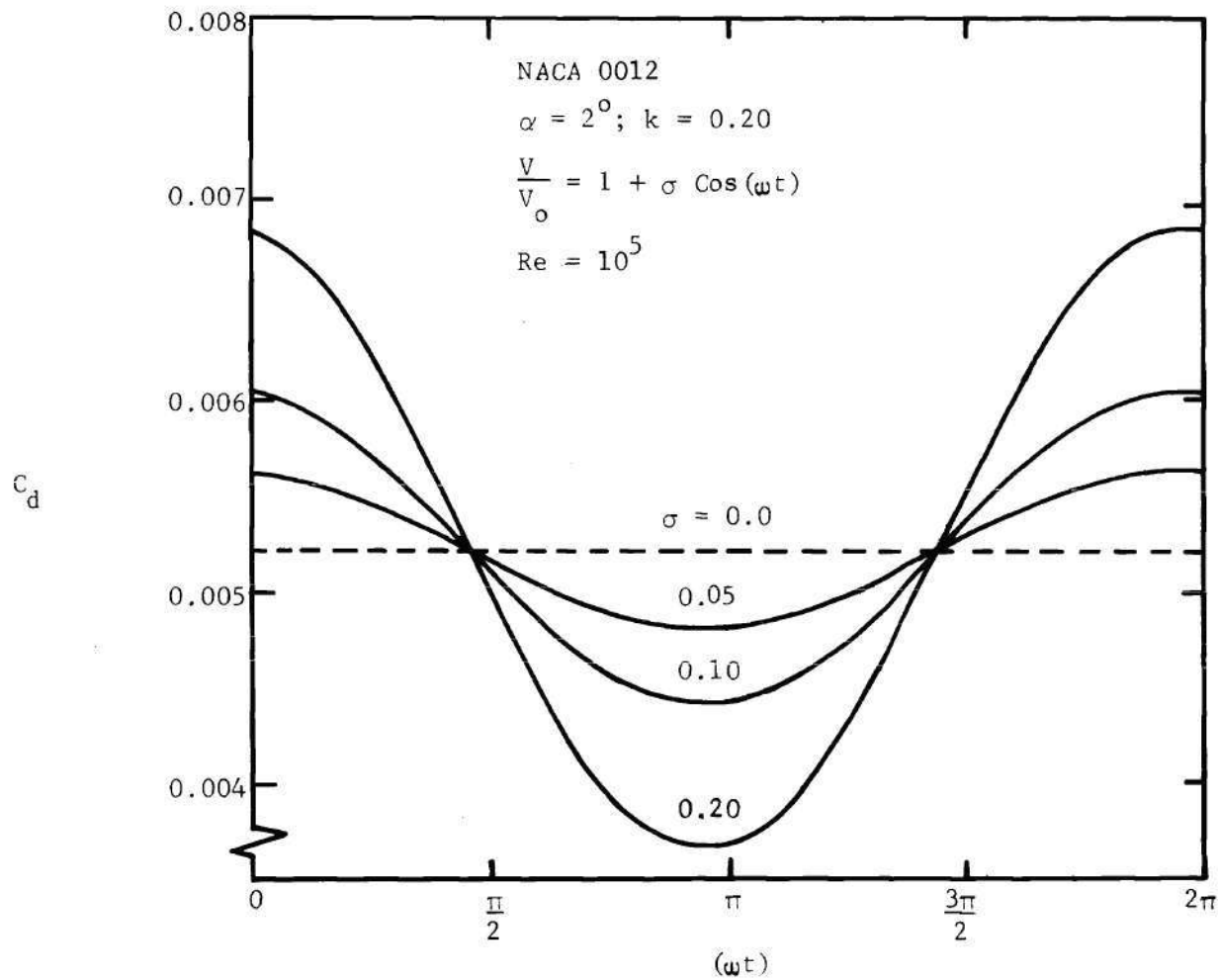


Figure 10. Variation of Drag with Time,  $\alpha = 2^\circ$ , Effect of  $\sigma$

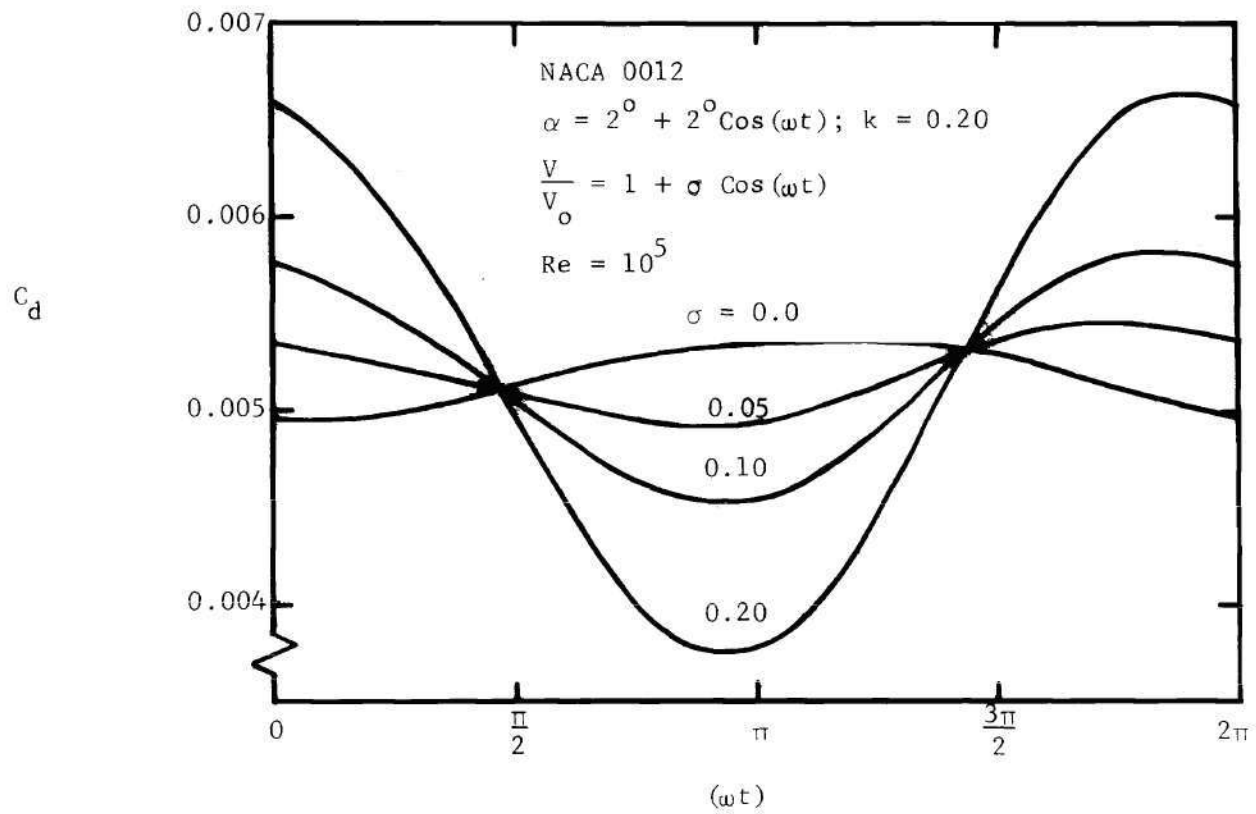


Figure 11a. Variation of Drag with Time,  $\alpha = 2^\circ + 2^\circ \cos(\omega t)$ , Effect of  $\sigma$

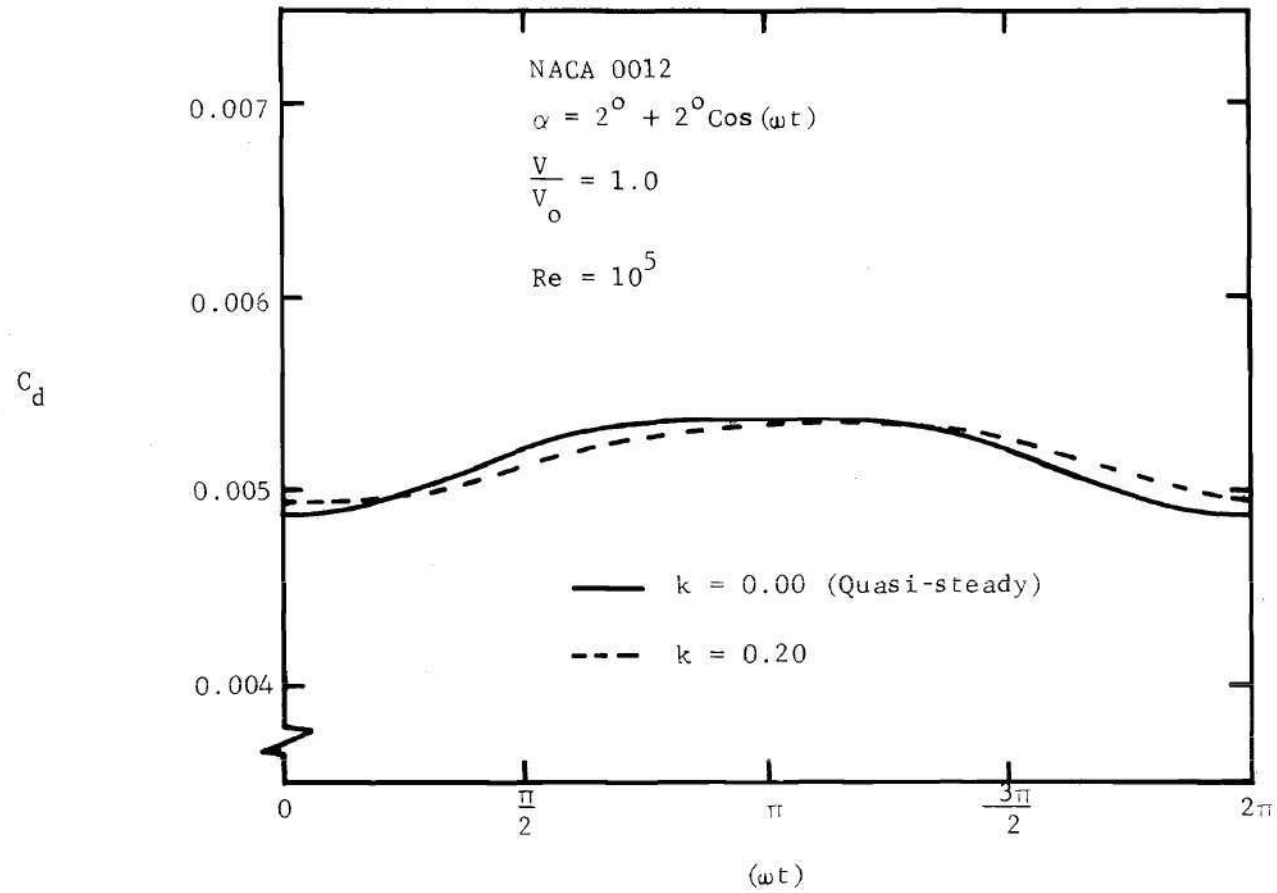


Figure 11b. Quasi-Steady Variation of Drag with Time,  $\alpha = 2^\circ + 2^\circ \cos(\omega t)$ ,  $\sigma = 0.00$

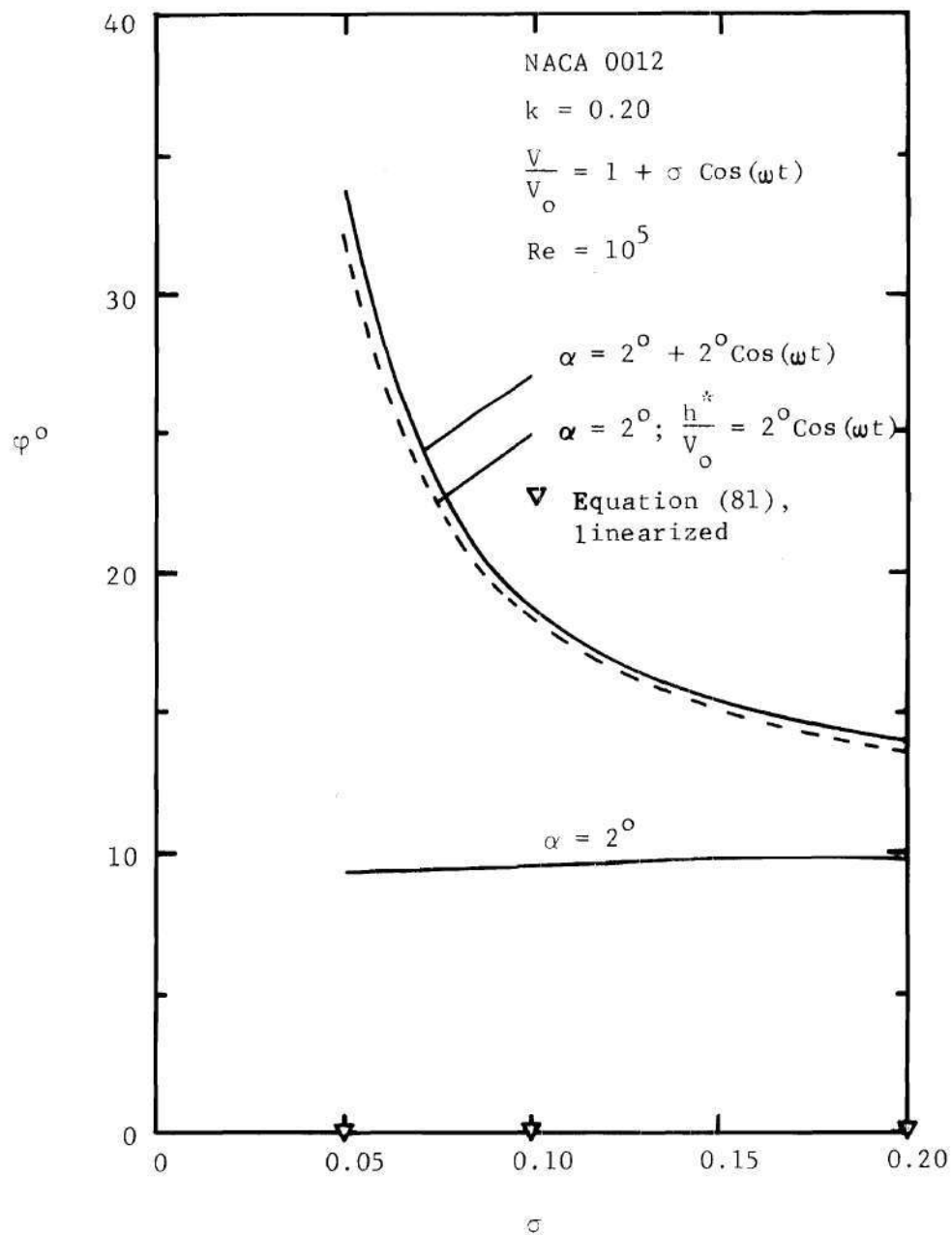


Figure 12. Variation of Phase,  $\phi$ , with  $\sigma$

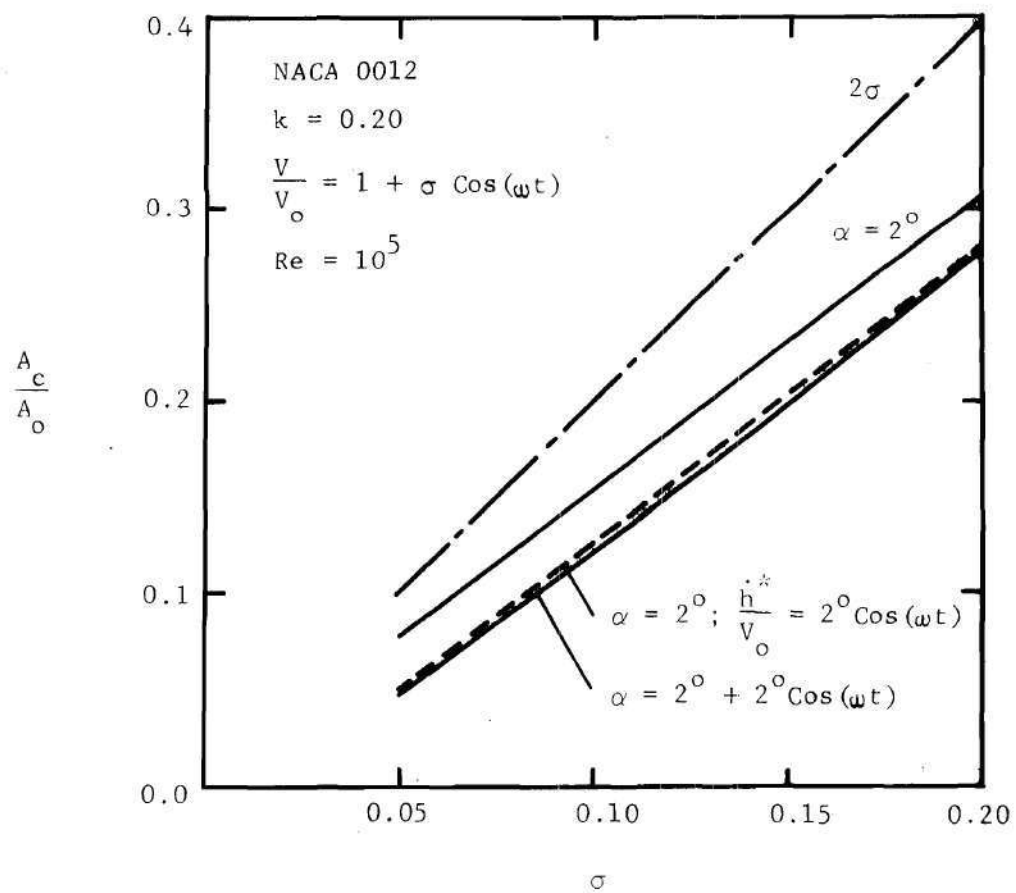


Figure 13. Variation of Amplitude Ratio,  $A_c/A_o$ , with  $\sigma$



(though not necessarily purely simple harmonic) from the  $\cos(\omega t)$  variation, and of course symmetric about  $\omega t = \pi$ . These conclusions were confirmed by actual calculations, the results of which are shown in Figure 11b. Also presented in Figure 11b, for comparison, is the  $\sigma = 0.00$  curve of Figure 11a ( $k = 0.20$ ). As noted earlier, the drag at  $k = 0.20$  has a phase lead of  $(\pi - \epsilon)$  radians and the difference,  $\epsilon$ , is therefore due to the non-zero value of the reduced frequency.

Note that in both Figures 10 and 11a all the curves intersect each other twice, at values of  $\omega t$  slightly less than  $\pi/2$  and  $3\pi/2$ . At  $V/V_0 = 1$  and  $\omega t = \pi/2$  and  $3\pi/2$ , the drag takes a value corresponding to that of the constant free stream case, regardless of  $\sigma$ . This also explains why, for the oscillating airfoil, the intersection near  $\omega t = 3\pi/2$  occurs at a higher value of  $C_d$  compared to the other intersection. That the intersections are not exactly at  $\pi/2$  and  $3\pi/2$  is indicative of the effect of reduced frequency. For  $k = 0.00$  the curves would be symmetrical about  $\omega t = \pi$  and intersect each other at  $\pi/2$  and  $3\pi/2$ .

It is evident from Figures 10 and 11a that the amplitude of the drag fluctuations increases as  $\sigma$  increases. The effect of  $\sigma$  on the phase with respect to the free stream velocity is, however, not so clearly discernible. These effects can be determined more precisely by fitting the least squares curve to the drag data and obtaining the constants  $A_0$ ,  $A_c$  and  $\phi$ , Equation (82). Shown in Figures 12 and 13 are the phase,  $\phi$ , and the amplitude ratio,  $A_c/A_0$ , versus  $\sigma$  for three cases:  $\alpha = 2^\circ$ ,  $\alpha = 2^\circ + 2^\circ \cos(\omega t)$ , and  $\alpha = 2^\circ$  with  $\dot{h}^*/V_0 = 2^\circ \cos(\omega t)$ . The free stream was represented by  $V/V_0 = 1 + \sigma \cos(\omega t)$  and the computations were performed for  $\sigma = 0.05, 0.10$ , and  $0.20$ , with  $Re = 10^5$  and  $k = 0.20$ .

It was found that the mean drag coefficient,  $A_0$ , was very nearly constant for all the cases, the maximum difference from 0.005226 being 0.8%. The ratio  $A_c/A_0$  for each condition was obtained by using the respective  $A_0$  and not the above value.

Figure 12 shows that for the stationary airfoil case,  $\alpha = 2^\circ$ , the phase advance varies very little with  $\sigma$ , being approximately  $9.5^\circ$ . The Lighthill result for the flat plate at zero incidence, discussed earlier, gives the skin friction phase advance to be independent of  $\sigma$  and a function of only  $\omega$ ,  $V_0$  and  $d$ . The results for the other two cases shown in the figure are quite different, with the phase advance decreasing as  $\sigma$  increases. Only the  $\alpha = 2^\circ + 2^\circ \cos(\omega t)$  case will be considered in detail since the interpretation for the  $\alpha = 2^\circ$  with  $\frac{\dot{h}^*}{V_0} = 2^\circ \cos(\omega t)$  condition is very similar. For very small  $\sigma$  the free stream velocity is very nearly constant and the drag curve is almost  $\pi$  radians off phase from the  $\cos(\omega t)$  variation. This is due to the  $2^\circ \cos(\omega t)$  oscillation as is evident from the  $\sigma = 0$  curves of Figures 10 and 11a. An increase in  $\sigma$  tends to overcome the effects of the angle of attack oscillation, thereby decreasing the phase advance of nearly  $\pi$  radians ( $180^\circ$ ) at  $\sigma = 0$  to approximately  $14^\circ$  at  $\sigma = 0.20$ . Note that compared to the  $\alpha = 2^\circ$  case the phase for  $\alpha = 2^\circ + 2^\circ \cos(\omega t)$  is higher. The cause for this is the almost  $180^\circ$  shift which gives a  $\cos(\omega t + 180^\circ) = -\cos(\omega t)$  contribution.

Figure 13 shows that for all three cases the amplitude ratio increases with  $\sigma$  and is linearly dependent on it. The Lighthill analysis, within its range of applicability, gives the same result. The lower  $A_c/A_0$  for the  $\alpha = 2^\circ + 2^\circ \cos(\omega t)$  is due to the  $-\cos(\omega t)$  contrib-

ution, discussed above.

The  $\alpha = 2^\circ$  with  $\dot{h}^*/V_0 = 2^\circ \cos(\omega t)$  condition is considered now. As Figures 12 and 13 show the results for this case are very similar to the  $\alpha = 2^\circ + 2^\circ \cos(\omega t)$  condition. From the expression for the downwash function, Equation (57a) in Chapter II, it can be seen that the downwash due to the translatory motion,  $\dot{h}$ , is analogous to the contribution from the  $\bar{\alpha}$  term. The only difference between the downwashes due to translation and angle of attack oscillation is the  $\dot{\alpha}$  contribution,  $ik\bar{\alpha}(x-a)$ , which is responsible for the small and almost constant deviation of the respective  $\phi$  and  $A_c/A_0$  curves from each other.

Also presented in Figures 12 and 13 are the phase and amplitude ratio variations obtained from the linearized form of Equation (81), which assumes a constant drag coefficient. This approximation gives the phase to be always zero and represents the amplitude ratio by  $2\sigma$ . That the phase is not at all predicted by this representation can be seen from Figure 12. As is evident from Figure 13 the amplitude ratio from this approximation differs considerably, by at least 25%, from the variations for the stationary and oscillating airfoils.

### Reduced Frequency Effects

The effect of the reduced frequency, a measure of unsteadiness, on the drag is shown in Figures 14-16.

Presented in Figure 14 is a typical set of  $C_d$  versus time curves for three values of  $k$ . Since the general trends were found to be similar for the stationary and the oscillating airfoil cases the drag curves are shown for the  $\alpha = 2^\circ + 2^\circ \cos(\omega t)$  condition only. Note that the  $k = 0.00$  curve is symmetrical about  $(\omega t) = \pi$  and has zero phase shift

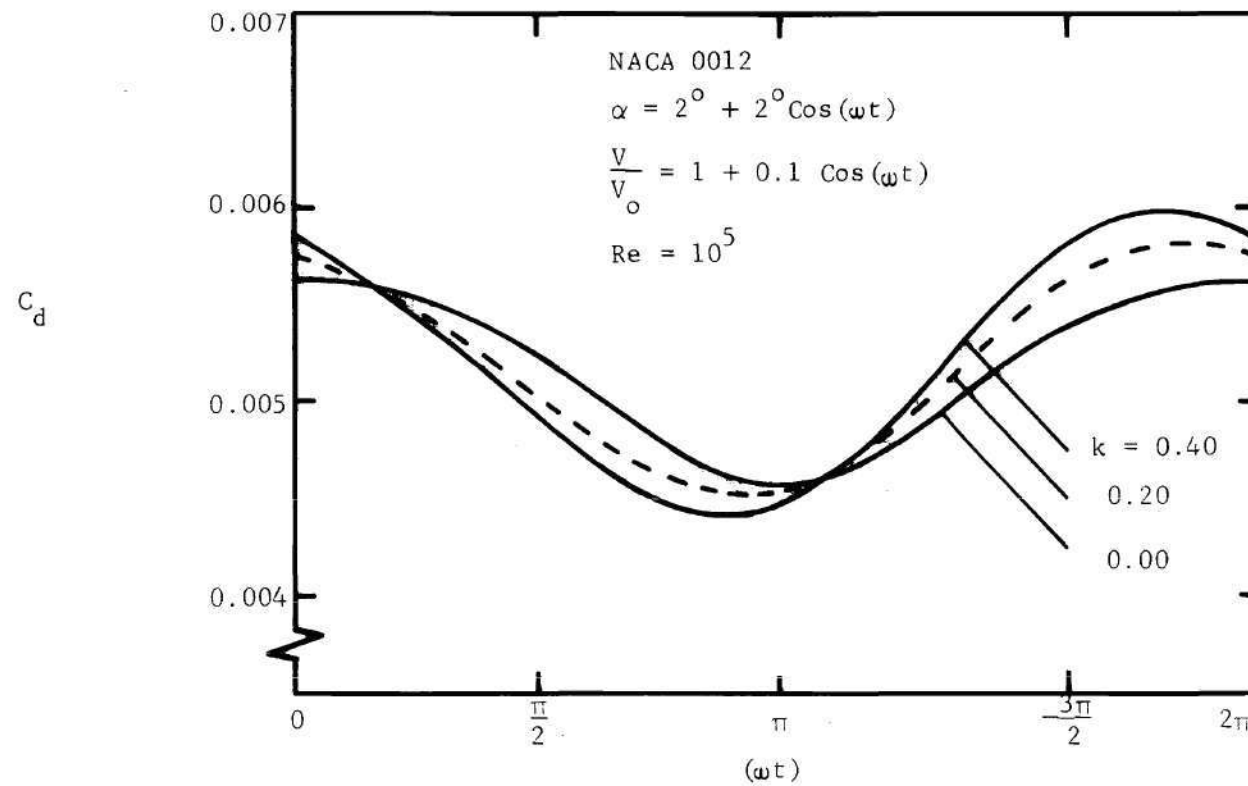


Figure 14. Variation of Drag with Time, Effect of Reduced Frequency,  $k$

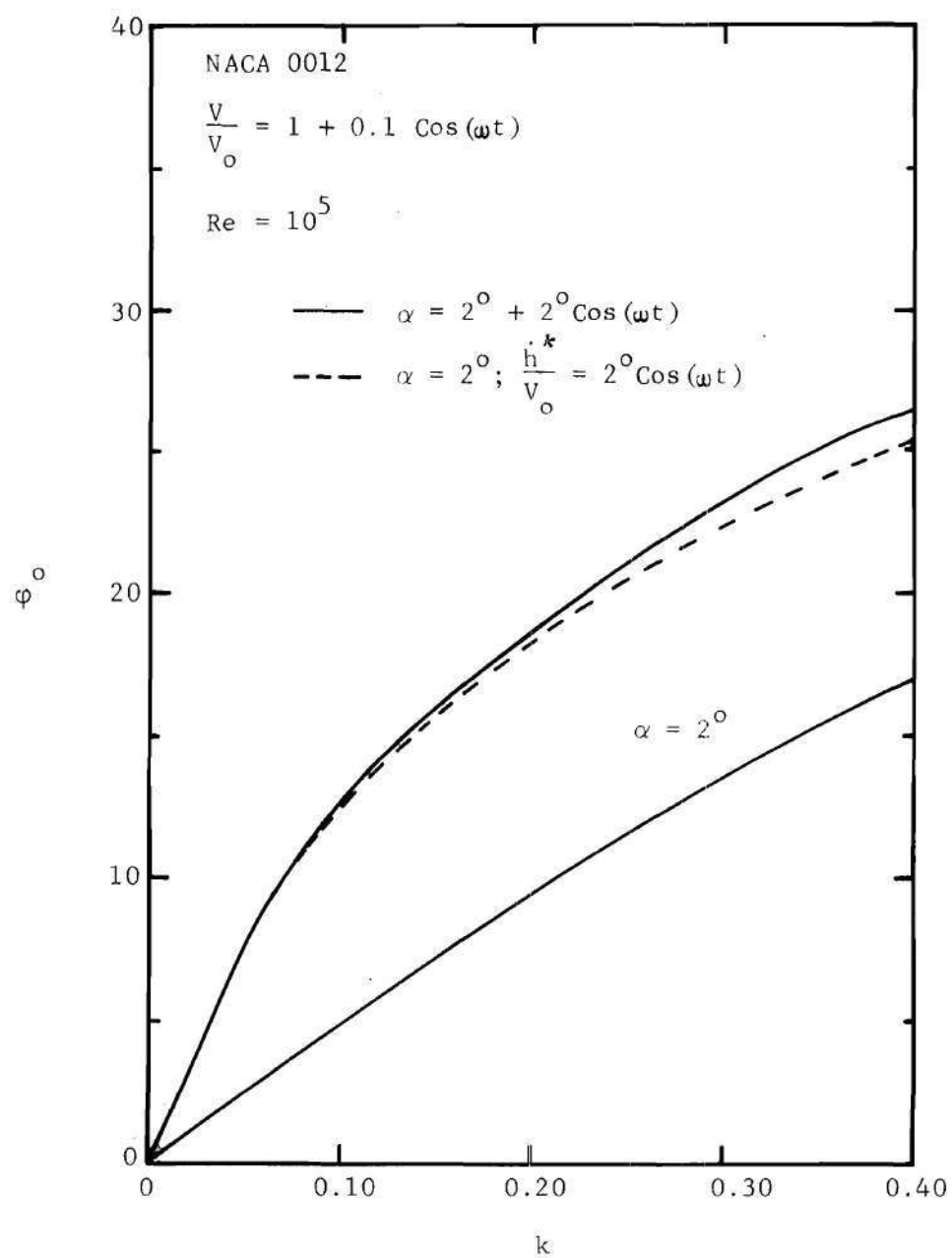


Figure 15. Variation of Phase,  $\phi$ , with Reduced Frequency,  $k$

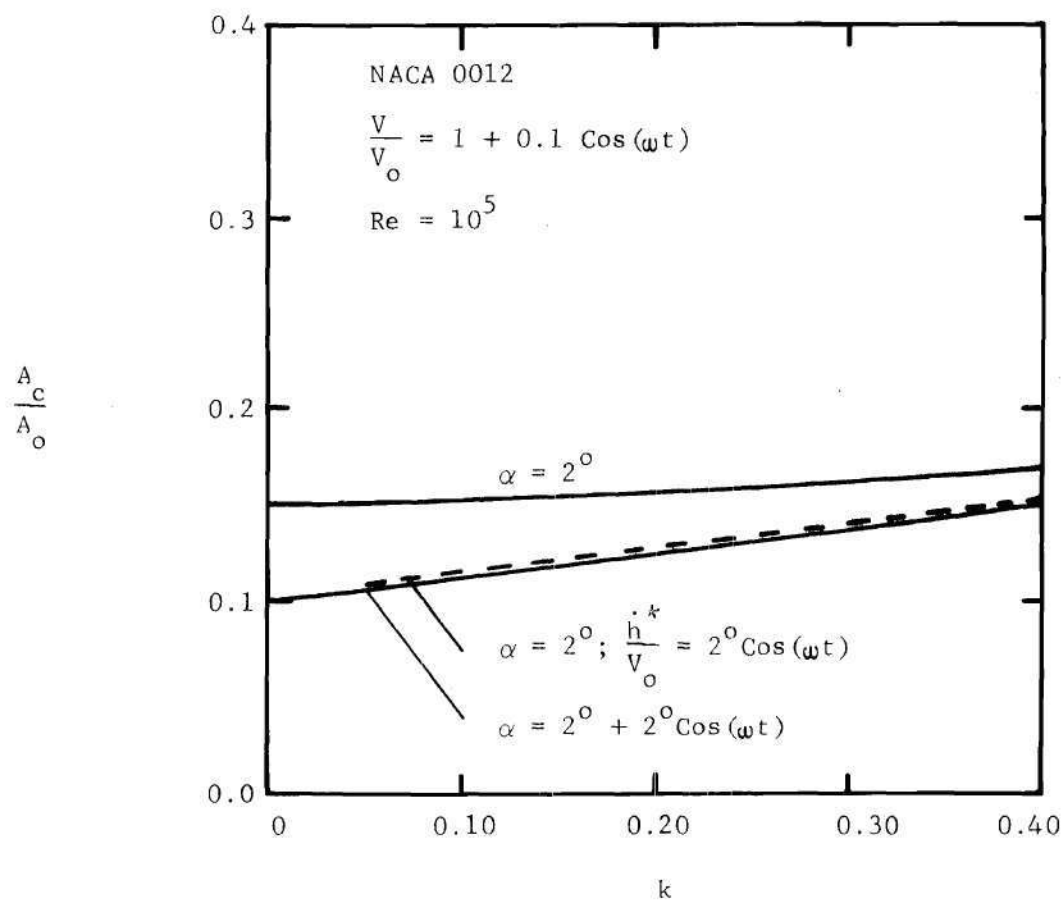


Figure 16. Variation of Amplitude Ratio,  $A_c/A_o$ , with Reduced Frequency,  $k$

with respect to the free stream velocity. If, in addition to keeping  $k = 0.00$ ,  $\sigma$  is set equal to zero the curve would maintain its symmetry but would have a  $180^\circ$  phase shift with respect to a  $\cos(\omega t)$  variation, as explained in the previous section. It can be seen that the amplitude and the phase advance of the drag fluctuations increase as the reduced frequency increases.

Figures 15 and 16 show the variations of the phase advance and the amplitude ratio with the reduced frequency. The computations were performed for three cases:  $\alpha = 2^\circ$ ,  $\alpha = 2^\circ + 2^\circ \cos(\omega t)$ , and  $\alpha = 2^\circ$  with  $\dot{h}^*/V_o = 2^\circ \cos(\omega t)$ . The free stream was specified as  $V/V_o = 1 + 0.1 \cos(\omega t)$  and  $Re$  was equal to  $10^5$ . Five values of the reduced frequency were investigated: 0.00, 0.05, 0.20, 0.30, and 0.40. It was found that  $A_o$  varied very little, the maximum percentage difference from 0.005202 being 0.6. As before, for each case the ratio  $A_c/A_o$  was obtained by using the respective  $A_o$ .

Figure 15 shows the increase in the phase advance as  $k$  increases. The curve for  $\alpha = 2^\circ$  is more linear than the non-stationary airfoil curves. Recall that the Lighthill low-frequency approximation for the flat plate gives the unsteady effects on the skin friction to be approximately proportional to the local reduced frequency,  $\omega d/V_o$ . The phase advances for the  $\alpha = 2^\circ + 2^\circ \cos(\omega t)$  and  $\alpha = 2^\circ$  with  $\dot{h}^*/V_o = 2^\circ \cos(\omega t)$  conditions are higher than the  $\alpha = 2^\circ$  phase. As explained in the previous section this increase is due to the  $-\cos(\omega t)$  type of contribution from the  $2^\circ \cos(\omega t)$  oscillations. Note that the nonlinearity in the curves is such that the slope decreases with increasing reduced frequency. For large reduced frequencies, then, the phase advance might reach a

maximum and level off. Such a behavior would be similar to the phase advance limit of  $45^\circ$  in the Lighthill high-frequency solution.

The increase of the amplitude ratio with reduced frequency can be seen in Figure 16. Whereas the slope for the  $\alpha = 2^\circ$  curve increases gradually from what appears to be a zero value, the other two curves have a constant positive slope — a linear variation. The reason, as before, for the lower  $A_c/A_o$  in the non-stationary airfoil cases is the  $-\cos(\omega t)$  type of contribution due to the  $2^\circ \cos(\omega t)$  oscillations.

Note that the difference between the curve for  $\alpha = 2^\circ$  and the other two curves decreases as the reduced frequency increases. The difference is maximum at  $k = 0.00$ , reflecting the largest reduction in  $A_c/A_o$  due to the full  $180^\circ$  phase shift ( $-\cos(\omega t)$  contribution). The phase,  $\varphi$ , however, is always zero for values of  $\sigma$  that are sufficiently large to overcome this effect of the  $2^\circ \cos(\omega t)$  oscillations.

For the  $\alpha = 2^\circ$  condition when  $k = 0.00$ ,  $A_c/A_o = 0.150$ . This corresponds to the well known [28] quasi-steady result:  $C_f \alpha (V/V_o)^{3/2}$ , which, for small fluctuations gives  $A_c/A_o \approx 3\sigma/2$  and  $\varphi = 0$ ; for  $\sigma = 0.1$   $A_c/A_o = 0.150$ .

The translating airfoil case,  $\alpha = 2^\circ$  with  $\dot{h}^*/V_o = 2^\circ \cos(\omega t)$ , is considered now. The difference between the phase advances of this case and that of  $\alpha = 2^\circ + 2^\circ \cos(\omega t)$  increases with the reduced frequency, as Figure 15 shows. This behavior is unlike the results of the previous section where both the differences between the respective  $\varphi$ 's and  $(A_c/A_o)$ 's were almost constant. Recall that the  $\dot{\alpha}$  term in the downwash, which distinguishes translation from angle of attack oscillation, is



proportional to the reduced frequency. Hence, the divergence of the two phase curves could be due to the increasing contribution of this term. However, the  $A_c/A_o$  versus  $k$  variations, Figure 16, have a constant difference between them. This means that for an increasing  $k$ , the  $\dot{\alpha}$  term has a greater influence on the phase than on the amplitude ratio.

### Effects due to Phase Difference Between Stream Fluctuations and Airfoil Oscillations

In general, it is possible that the free stream fluctuations and the airfoil oscillations are not in phase with each other. Figures 17 and 18 show the effect of such a phase difference,  $\psi$ , on the phase,  $\phi$ , and the amplitude ratio for four values of the reduced frequency. The free stream velocity was specified as  $V/V_o = 1 + 0.1 \cos(\omega t)$  with an angle of attack variation of  $\alpha = 2^\circ + 2^\circ \cos(\omega t + \psi)$ , and  $Re = 10^5$ . Computations were performed for 12 values of  $\psi$ :  $0, \pi/4, \pi/2, 5\pi/8, 3\pi/4, 7\pi/8, \pi, 5\pi/4, 3\pi/2, 13\pi/8, 7\pi/4$ , and  $15\pi/8$ . For each  $\psi$  the following values of the reduced frequency were investigated: 0.00, 0.15, 0.20, and 0.30. For the constant  $A_o$ , it was found that the maximum percentage difference from 0.005188 was 0.4, the respective  $A_o$  being used for obtaining  $A_c/A_o$  in each case. The results of the preceding two sections show that the effects on the drag due to translation and angle of attack oscillation are quite similar to each other. Hence, only the angle of attack oscillation was investigated.

Figure 17 shows that the phase of the drag is greatly influenced by variations in the phase difference,  $\psi$ . Note that the phase undergoes not only large percentage changes in magnitude but also a change in

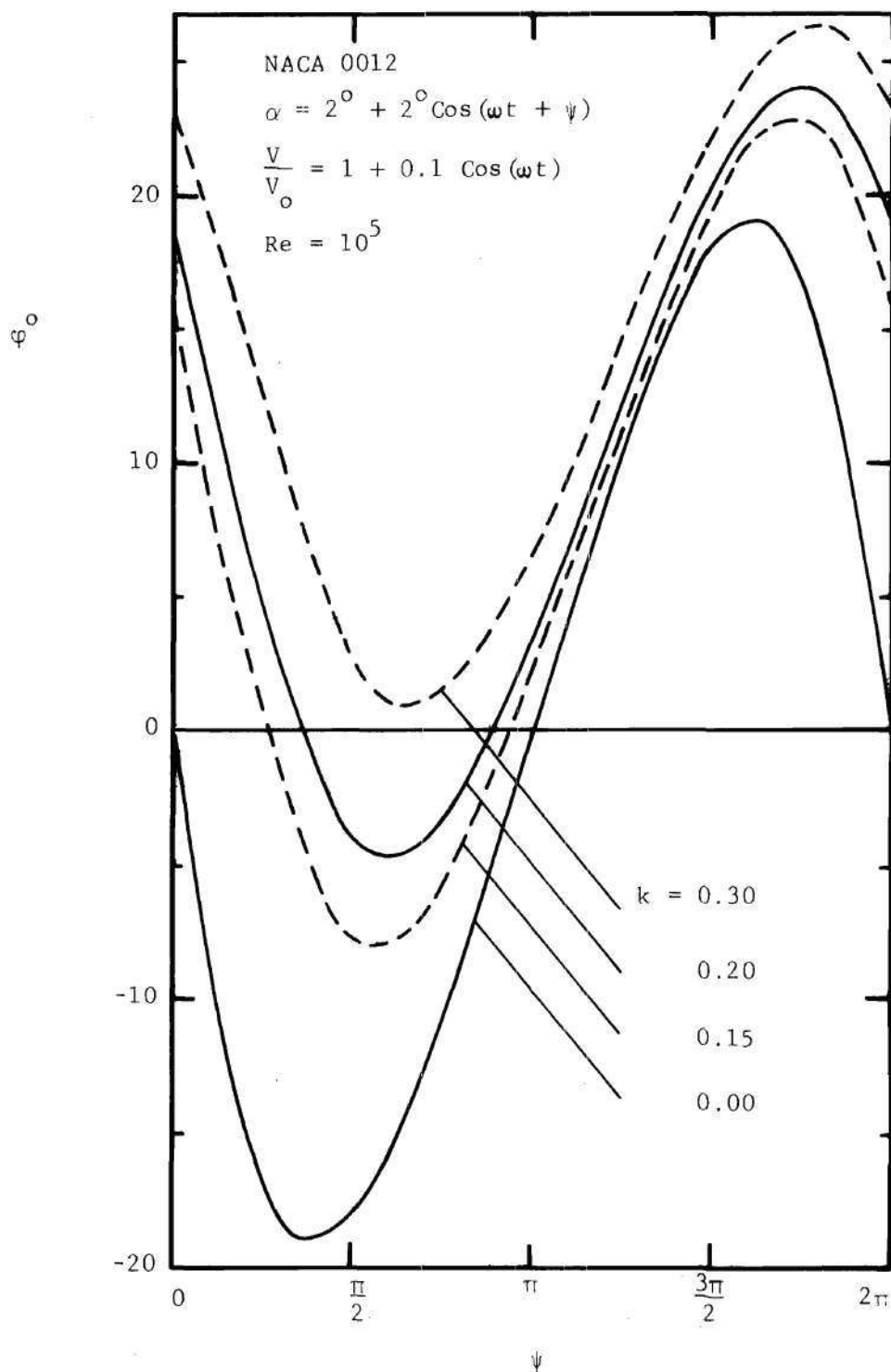


Figure 17. Variation of Phase,  $\phi$ , with Phase Difference,  $\psi$ , and Reduced Frequency,  $k$

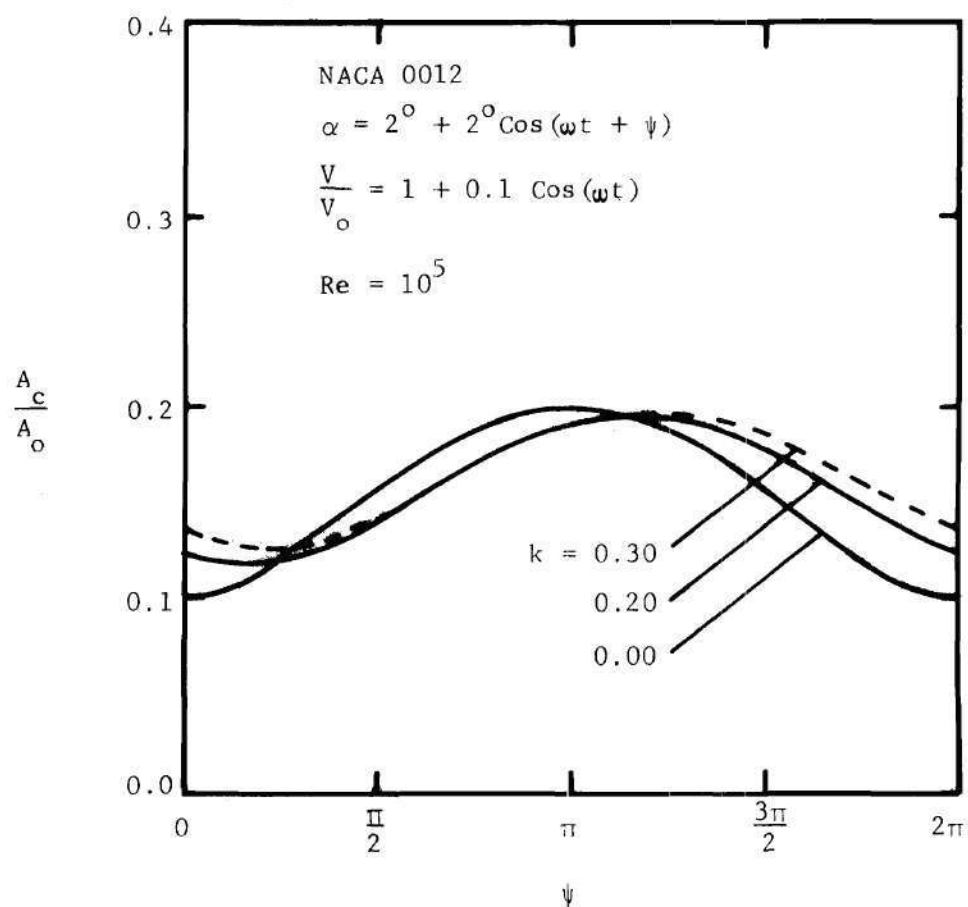


Figure 18. Variation of Amplitude Ratio,  $A_c/A_o$ , with Phase Difference,  $\psi$ , and Reduced Frequency,  $k$

sign, i.e. the drag can either lead or lag the free stream. This behavior can be explained by considering the movement of the upper surface zero wall shear location. In the following discussion only a brief account is given since the explanation is the same as the one presented with regard to the  $\sigma = 0.00$  curve of Figure 11a. Let  $k$  and  $\sigma$  be equal to zero. For  $\psi = 0$  it was shown earlier that the phase shift is  $180^\circ$ , Figure 11b. By the same reasoning the following can also be demonstrated: when  $\psi = \pi/2, \pi$ , and  $3\pi/2$ ,  $\varphi$  is equal to  $-90^\circ, 0^\circ$ , and  $90^\circ$ , respectively. The computations completely confirmed these conclusions. For a sufficiently large  $\sigma$  the  $180^\circ$  phase shift ( $-\cos(\omega t)$  contribution) at  $\psi = 0$  is overcome completely by the quasi-steady  $+\cos(\omega t)$  variation introduced by the free stream, resulting in  $\varphi = 0$ ; the drag is in phase with the free stream -  $k = 0.00$  curve of Figure 14. Therefore, at  $\psi = 0$ , the introduction of a non-zero  $\sigma$  diminishes the phase effects due to the angle of attack oscillations. This conclusion is valid for  $\psi \neq 0$  also: at  $\psi = (\pi/2, 3\pi/2)$  for  $\sigma = 0.05, 0.10$ , and  $0.15$  the corresponding  $\varphi$ 's are  $(-33^\circ, 33^\circ)$ ,  $(-18^\circ, 18^\circ)$ , and  $(-12^\circ, 12^\circ)$ . At  $\psi = \pi$ ,  $\sigma$  has no effect on  $\varphi$  since there is no phase shift to start with. Hence, it follows that for  $k = 0.00$  an increase in  $\sigma$  reduces the absolute maximum value of  $\varphi$ . This is only a restatement of the above conclusion. The effect of  $\sigma$  when  $k > 0$  is considered later in this section.

For all values of  $\psi$  an increase in the reduced frequency tends to make  $\varphi$  more positive, that is, diminish the phase lag and increase the advance. This can be seen from Figure 17 and, for  $\psi = 0$ , from Figure 15. It is interesting to note, however, that the magnitude of this effect is dependent on  $\psi$ , as is evident from Figure 17 where, for

$\pi/2 < \psi < 3\pi/2$  the curves are much closer to each other than at other values of  $\psi$ . This lack of uniformity is indicative of a nonlinear variation of the reduced frequency effect with  $\psi$ .

The variation of  $A_c/A_o$  with  $\psi$ , Figure 18, is considered now. The curve for  $k = 0.15$  has been omitted since the essential features can be understood from the other three variations. Note that the phase difference,  $\psi$ , has a large effect on the amplitude ratio. The  $k = 0.00$  curve is symmetrical about  $\psi = \pi$  with a minima and a maxima at  $\psi = 0$  and  $\pi$  respectively. These extremes occur because of the  $180^\circ$  and  $0^\circ$  phase shifts due to the angle of attack oscillations; the former reducing the quasi-steady fluctuations introduced by the free stream velocity and the latter augmenting the same. An increase in the reduced frequency shifts the curves to the right. For a non-zero  $k$ , that the minima and maxima do not occur at  $\psi = 0$  and  $\pi$  respectively can be due to a combination of: 1) the phase advance effect of  $k$ ; and, 2) the shift in the drag variation due to the angle of attack oscillations. For example, the phase of the  $\sigma = 0.00$  curve of Figure 11a is less than  $180^\circ$ , the full value being realized only for  $k = 0.00$ , Figure 11b.

The increase in  $A_c/A_o$  with the reduced frequency for  $\psi = 0$  can be seen from Figure 16 also. At some other values of  $\psi$  an increase in the reduced frequency brings about a reduction in  $A_c/A_o$  — for  $\pi/4 < \psi \leq \pi$  in Figure 18.

The variation of  $\varphi$  and  $A_c/A_o$  with  $\psi$  and  $\sigma$  is considered now. Figures 19 and 20 show these effects for four values of  $\psi$  and three different  $\sigma$ 's. The reduced frequency and Reynolds number were equal to 0.20 and  $10^5$ , respectively.

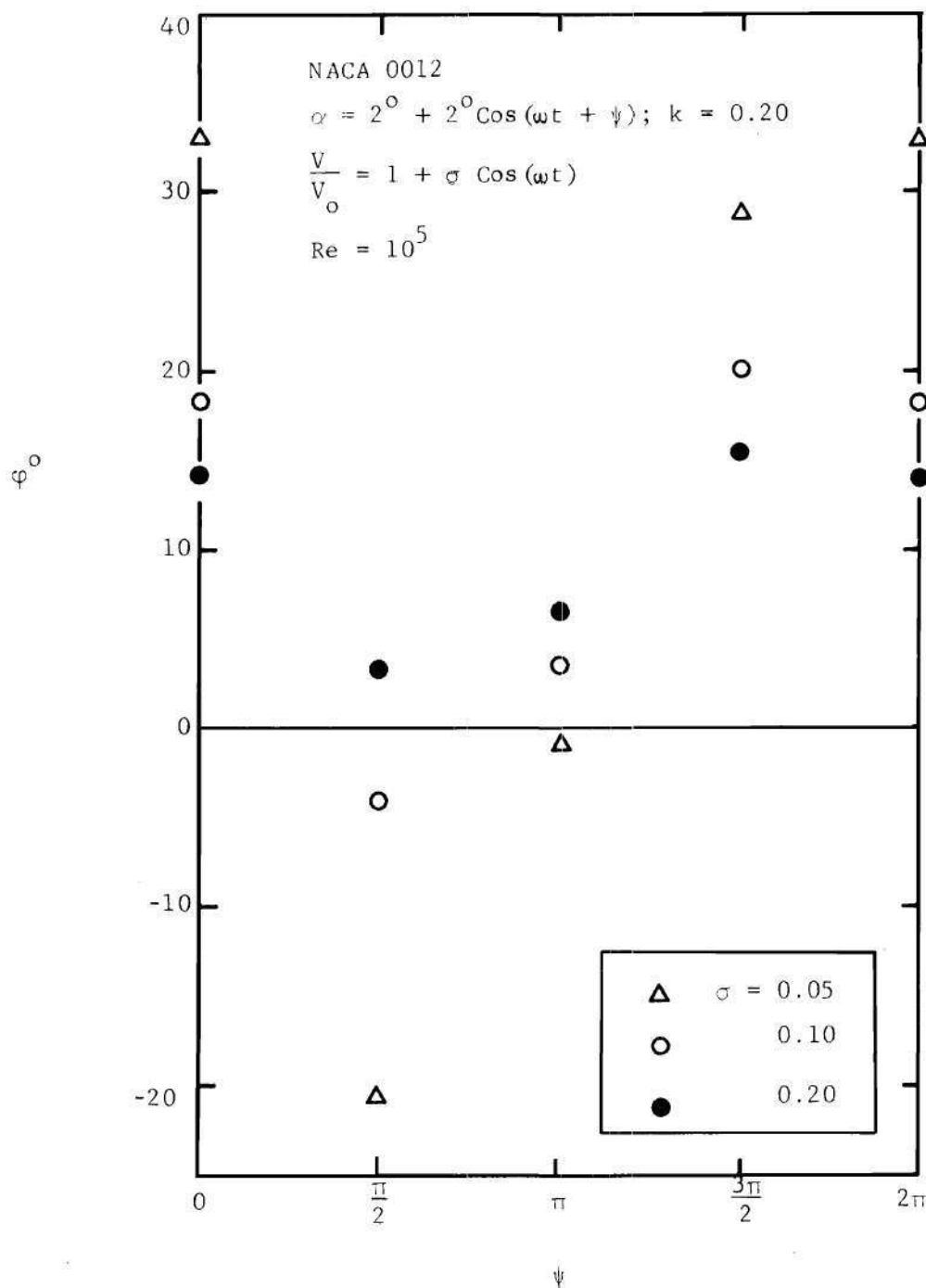


Figure 19. Variation of Phase,  $\phi$ , with Phase Difference,  $\psi$ , and  $\sigma$

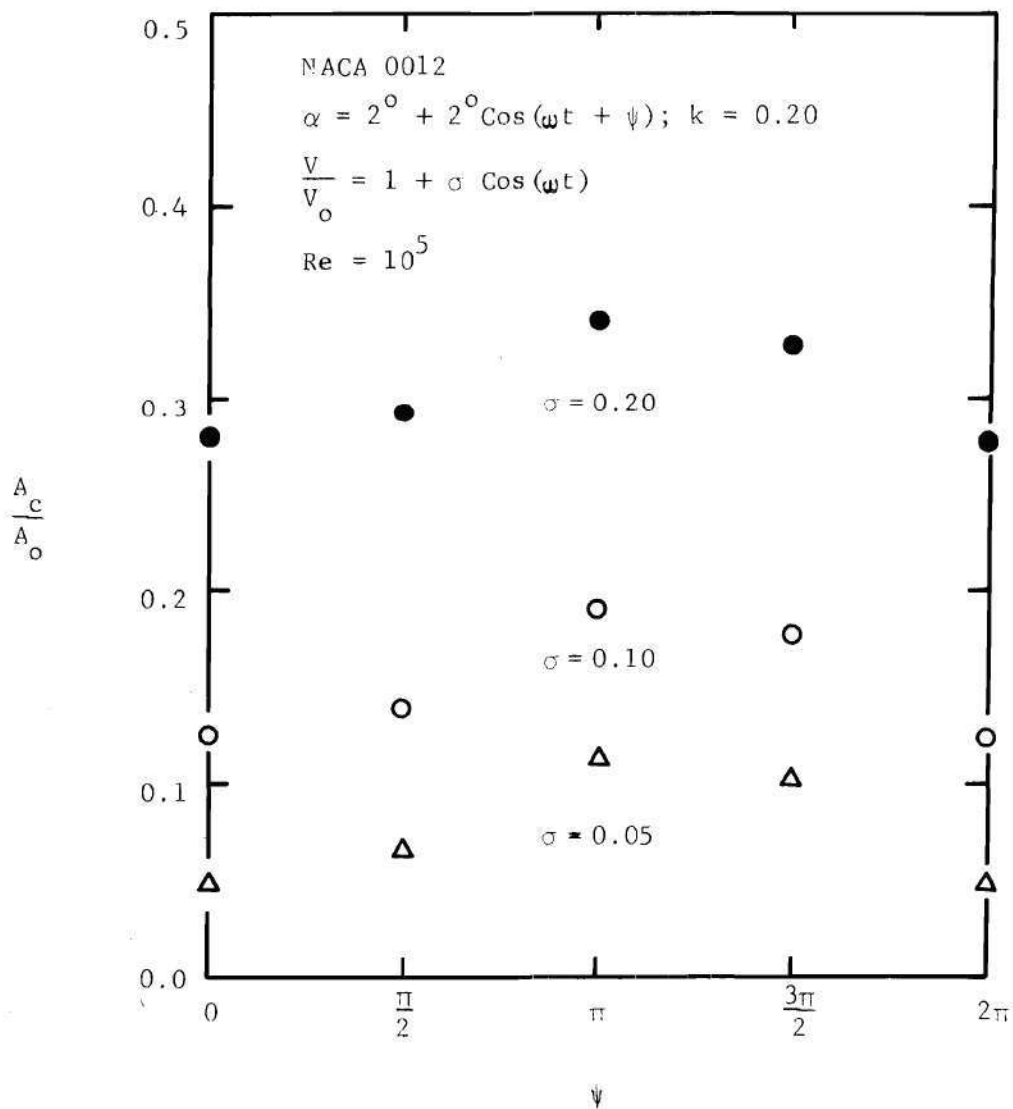


Figure 20. Variation of Amplitude Ratio,  $A_c/A_o$ , with Phase Difference,  $\psi$ , and  $\sigma$

Figure 19 shows that an increase in  $\sigma$  suppresses the variations in  $\varphi$  with respect to  $\psi$ . For  $k = 0.00$  this has been established earlier — see discussion regarding Figure 17. It is to be noted that for  $k = 0.00$  these decreased variations appear to occur around a "limit"  $\varphi$  of  $0^\circ$ . The corresponding "limit"  $\varphi$  from Figure 19 ( $k = 0.20$ ) appears to be around  $9^\circ$ . Recall that for the constant incidence,  $\alpha = 2^\circ$ , case  $\varphi$  was almost unvarying with  $\sigma$ , Figure 12, and for  $k = 0.20$  the value was close to  $9.5^\circ$ . These observations suggest that, in general for all  $\psi$ 's, increasingly higher values of  $\sigma$  tend to equalize the oscillating airfoil and constant incidence phases, at the same reduced frequency. Physically, this would mean that as the amplitude of the free stream fluctuations increases the tendency is to suppress the phase effects of the angle of attack oscillations; only the airfoil at a constant incidence is "seen" by the free stream.

Recall that for  $\psi = 0$  the amplitude ratio,  $A_c/A_o$ , varied linearly with  $\sigma$ , Figure 13. As is evident from Figure 20 this linearity is maintained for all values of  $\psi$ .

### Superposition of Drag

Recall that the linearized approach for the potential flow analysis allowed the superposition of the individual effects due to the oscillations and the constant incidence. Thus, the total lift and moment could be obtained by a summation of the individual contributions. However, the employment of the pressure distribution from such a linear analysis does not ensure, a priori, a corresponding linear behavior for the drag, since the boundary layer equations are nonlinear.

Consider the following three cases: 1)  $\alpha = 2^\circ$  with  $V/V_o =$



1)  $\alpha = 1 + \sigma \cos(\omega t)$ , 2)  $\alpha = 2^0 + 2^0 \cos(\omega t + \psi)$  with  $V/V_0 = 1$ , and 3)  $\alpha = 2^0 + 2^0 \cos(\omega t + \psi)$  with  $V/V_0 = 1 + \sigma \cos(\omega t)$ . The present computations established that the perturbation drag in the last case can be obtained very closely by a superposition of results from the other two cases.

Several conditions were investigated:  $Re = 10^5$  with,  $0.05 \leq \sigma \leq 0.20$ ,  $0.00 \leq k \leq 0.40$ , and  $0 \leq \psi \leq 2\pi$ , and it was found that the differences between the actual and superposed  $(A_c/A_0)$ 's and  $\varphi$ 's were less than 2%. All  $A_0$ 's were within 1% of 0.005224. As an illustrative example let  $V/V_0 = 1 + 0.1 \cos(\omega t)$ ,  $k = 0.20$ ,  $\psi = 0$ , and  $Re = 10^5$ , and express the drag coefficient as  $C_d = A_0(1 + D_1 \cos(\omega t) + D_2 \sin(\omega t))$ . Note that  $A_c/A_0 = (D_1^2 + D_2^2)^{1/2}$  and  $\varphi = -\tan^{-1}(D_2/D_1)$ . The respective computed  $(D_1, D_2)$  sets for the three cases were: (0.154, -0.025), (-0.037, -0.014), and (0.117, -0.039). Obviously, a summation of the corresponding constants of the first two sets yields the third set.

### Reynolds Number Dependency

For laminar flow the governing equations, (70) and (71), and their boundary conditions are independent of the Reynolds number and hence, the transformed profiles,  $g$ ,  $h$ , do not depend on the Reynolds number. The skin friction coefficient,  $C_f$ , is of course a function of the Reynolds number. It can be shown from fundamental definitions that  $C_f$  and therefore,  $C_d \propto Re^{-1/2}$ . This makes  $A_0$  and  $A_c \propto Re^{-1/2}$  and  $\varphi$  independent of  $Re$ . Note that  $A_c/A_0$  is not a function of  $Re$ . As expected, the computed results also showed the above variations with Reynolds number. Three values of  $Re$  were investigated:  $0.5 \times 10^5$ ,  $10^5$ , and  $2 \times 10^5$ . Finally, it is noted that the zero wall shear location is theoretically independent of the Reynolds Number.

### Turbulent Flow Results

Of the several analyses that have been performed to determine the response of the flat plate turbulent boundary layer to a fluctuating free stream the detailed study of McCroskey and Philippe [30] is of direct interest here. Relevant to the present study is their conclusion that the turbulent skin friction is approximately quasi-steady over a wide frequency range. With increasing frequency the skin friction phase remains close to that of the free stream velocity and the amplitude is almost constant.

The NACA 0012 basic thickness form was used in the present calculations. For the oscillating airfoil the quarter chord point was specified to be the axis of rotation. Typical computer time per run on the CDC 6600 was approximately 12 minutes. Note that for the turbulent case the computer central memory requirement is much higher than that for the completely laminar condition, thus creating large delays in the run turnaround.

### Preliminary Discussion

For the airfoil incidences that were considered the turbulent wall shear was never zero. The patterns of movement of the lower and upper surface transition points were found to have a considerable influence on the drag changes. At a theoretical transition point and downstream of it, the turbulent skin friction is of course much higher as compared to the corresponding laminar condition, for example see Figure 3. Consider two cases, where in the first case the transition point is upstream of the transition location in the other case. Consi-

dering only the effect due to the difference in the two locations the first case would then show a higher skin friction drag.

It was found that for the constant incidence case the transition points were stationary throughout the cycle of the free stream fluctuations. For the oscillating airfoil the transition points were not stationary, displaying considerable amounts of movement. Figures 21 and 22 show the drag variations with time for the above cases for two values of the reduced frequency: 0.00 and 0.20. As can be seen from Figure 22, the  $\alpha = 3.5^\circ$  variation is smoother than the one for  $\alpha = 3.5^\circ + 2^\circ \cos(\omega t)$ .

Note that for the  $k = 0.00$  condition the amplitude of the drag fluctuations for the oscillating airfoil appears to be less than that for the constant incidence airfoil, a behavior that is reversed at  $k = 0.20$ . A consideration of the upper and lower surface transition point movements, shown in Figures 23 and 24, is useful in interpreting these trends. Consider the  $k = 0.00$  condition where there is no hysteresis type of effect present. An increase in  $\alpha$  tends to move the upper transition location upstream, i.e. towards the leading edge. The movement is in the opposite direction for the lower location. These two movements act in opposition, with the former and latter tending to increase and decrease the drag, respectively. The lower amplitude of the drag fluctuations for  $\alpha = 3.5^\circ + 2^\circ \cos(\omega t)$  at  $k = 0.00$  implies, therefore, that the lower transition point movement has a greater influence on the drag changes. Consider now the  $k = 0.20$  condition. As Figures 23 and 24 show the transition curves are affected considerably by an increase in the reduced frequency from 0.00 to 0.20. The per-

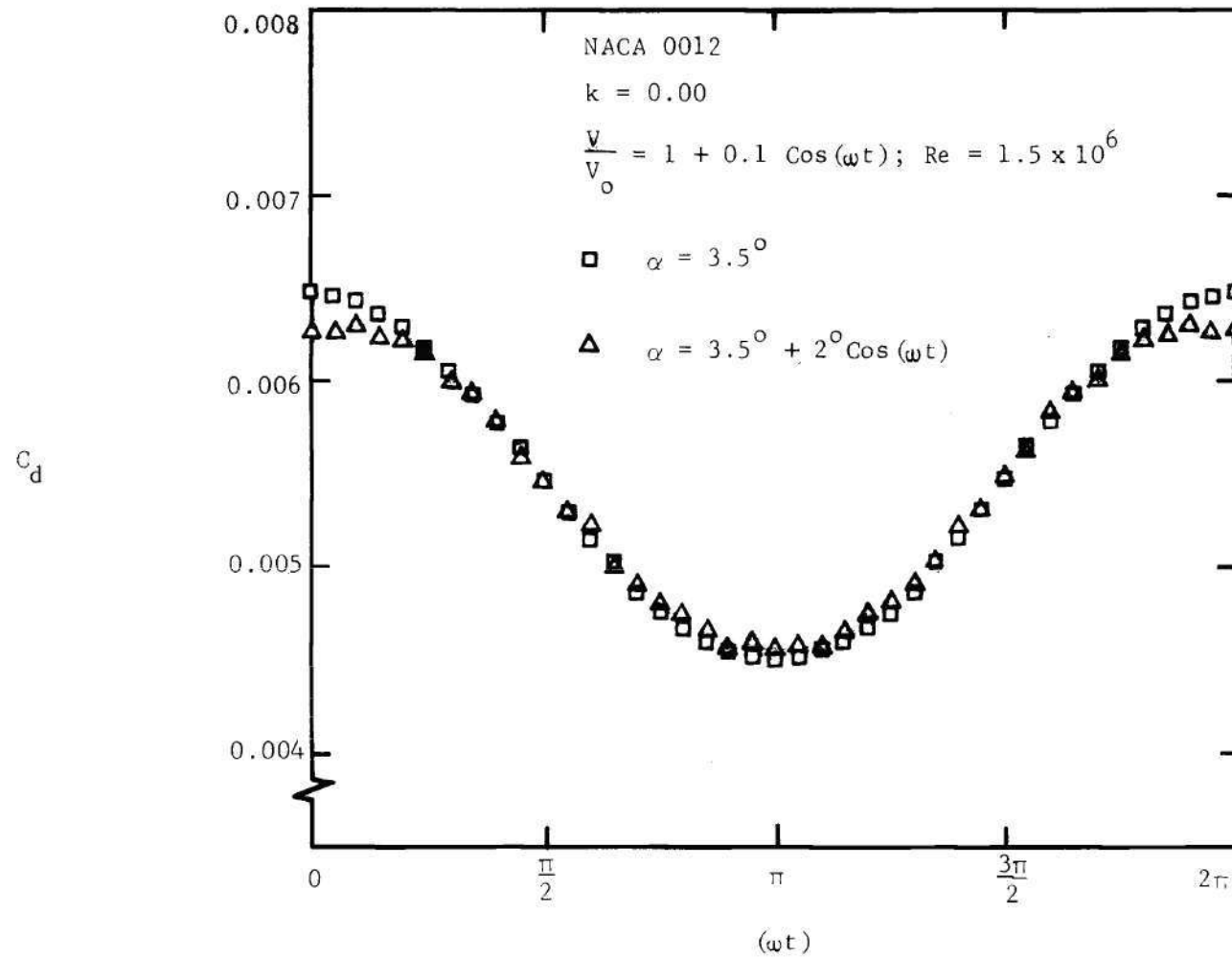


Figure 21. Variation of Drag with Time,  $k = 0.00$

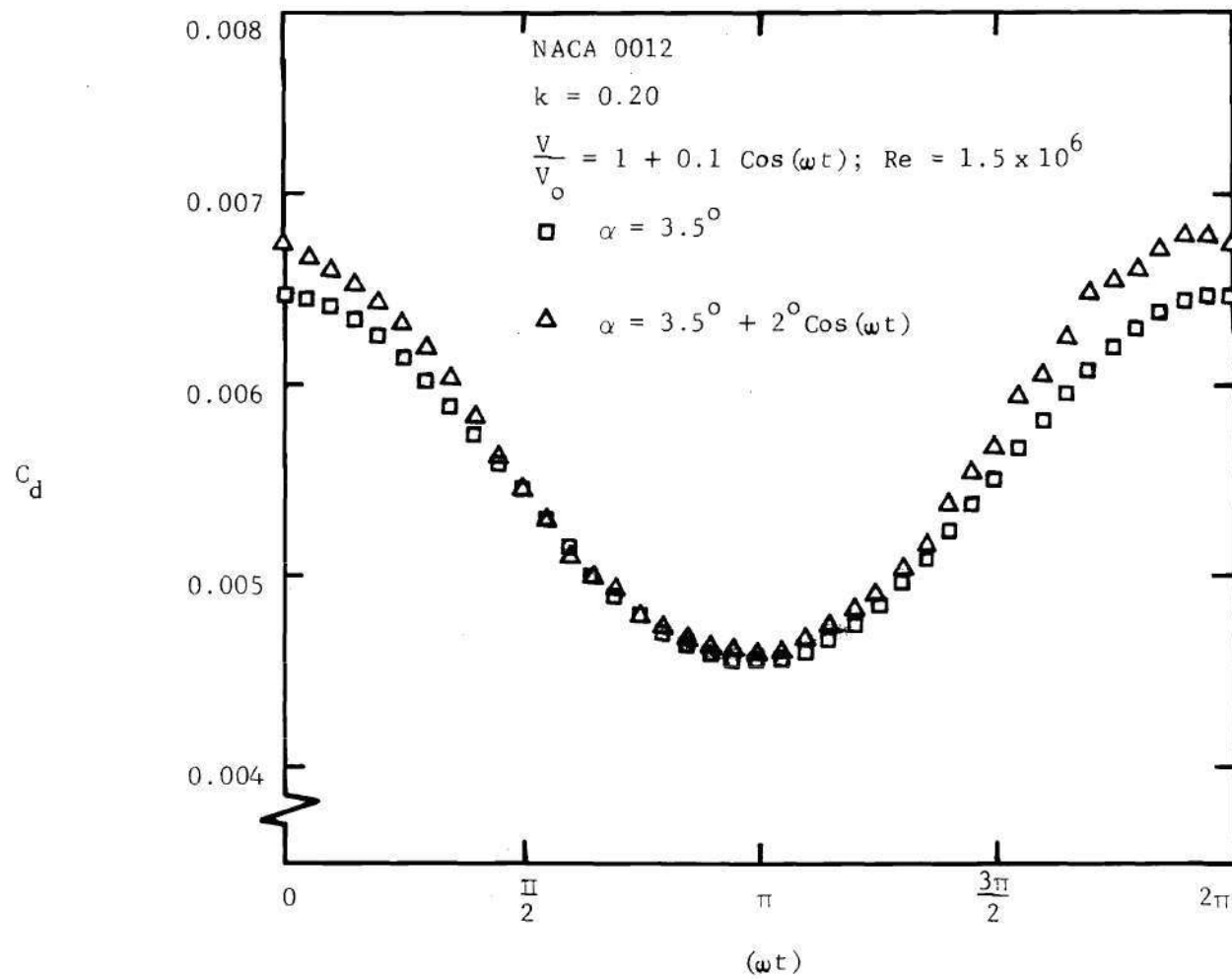


Figure 22. Variation of Drag with Time,  $k = 0.20$

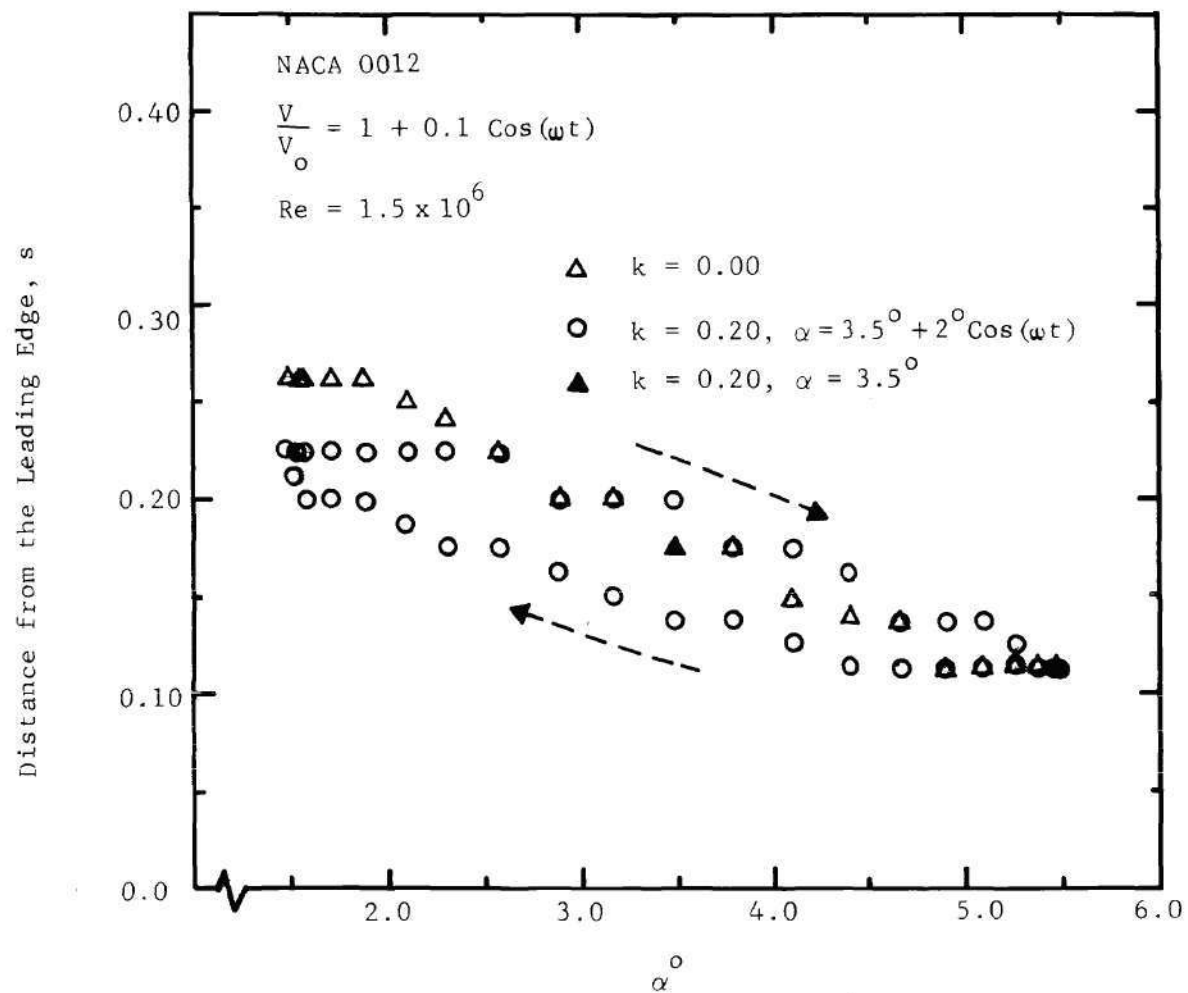


Figure 23. Transition Point Variations - Upper Surface

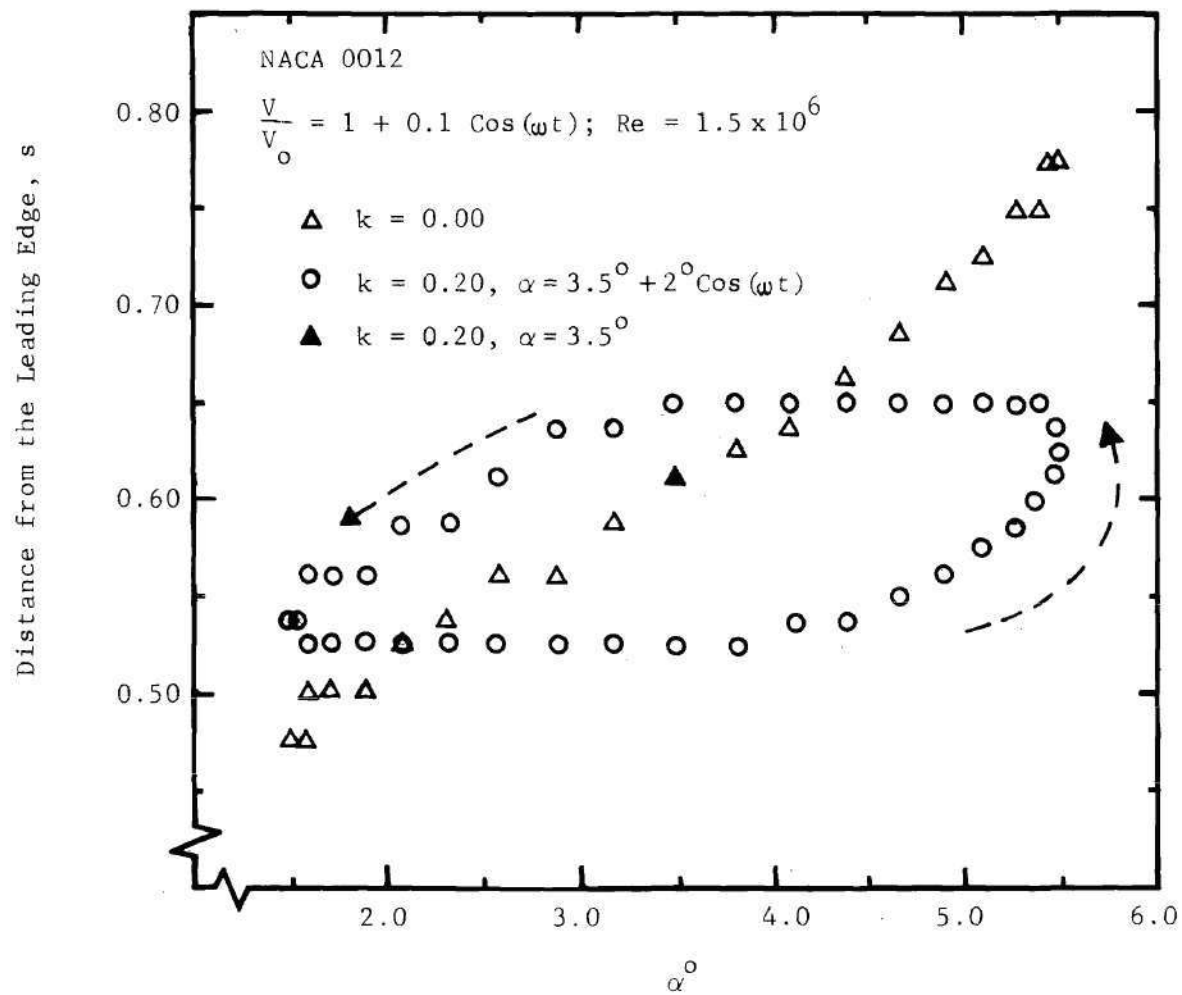


Figure 24. Transition Point Variations - Lower Surface

tage reduction in the total travel of the lower location is greater than that of the upper transition point. The effect of this difference would be to diminish the influence of the lower transition point movement. The higher amplitude of the drag fluctuations for the  $\alpha = 3.5^\circ + 2^\circ \cos(\omega t)$  case, Figure 22, then implies that at  $k = 0.20$  it is the upper location movement that has a greater influence on the drag changes.

The opposite effects of the two movements cause a deviation from a harmonic drag variation. For  $k = 0.00$  the curves are symmetrical about  $\omega t = \pi$ , Figure 21, and have a zero phase with respect to the free stream velocity. Note that for the  $\alpha = 3.5^\circ$  case the transition points are stationary and the variation is very nearly harmonic. For  $\alpha = 3.5^\circ + 2^\circ \cos(\omega t)$  the hysteresis type of behavior, Figures 23 and 24, introduced by a non-zero reduced frequency causes an asymmetry in the drag about  $\omega t = \pi$  and increases the deviation from a harmonic variation, Figure 22. For the  $\alpha = 3.5^\circ$  condition at  $k = 0.20$  the transition points are still stationary and the curve is again very nearly harmonic though a phase shift is present due to the non-zero reduced frequency. These observations are of course confirmed by the least squares fit results presented in succeeding sections.

#### Reduced Frequency Effects

For the oscillating airfoil the increase in the amplitude of the drag fluctuations with increasing reduced frequency are apparent in Figure 25. The phase shift changes, however, are not so clearly discernible.

The phase and amplitude ratio variations with reduced frequency are presented in Figures 26 and 27. Note the expanded scales for both



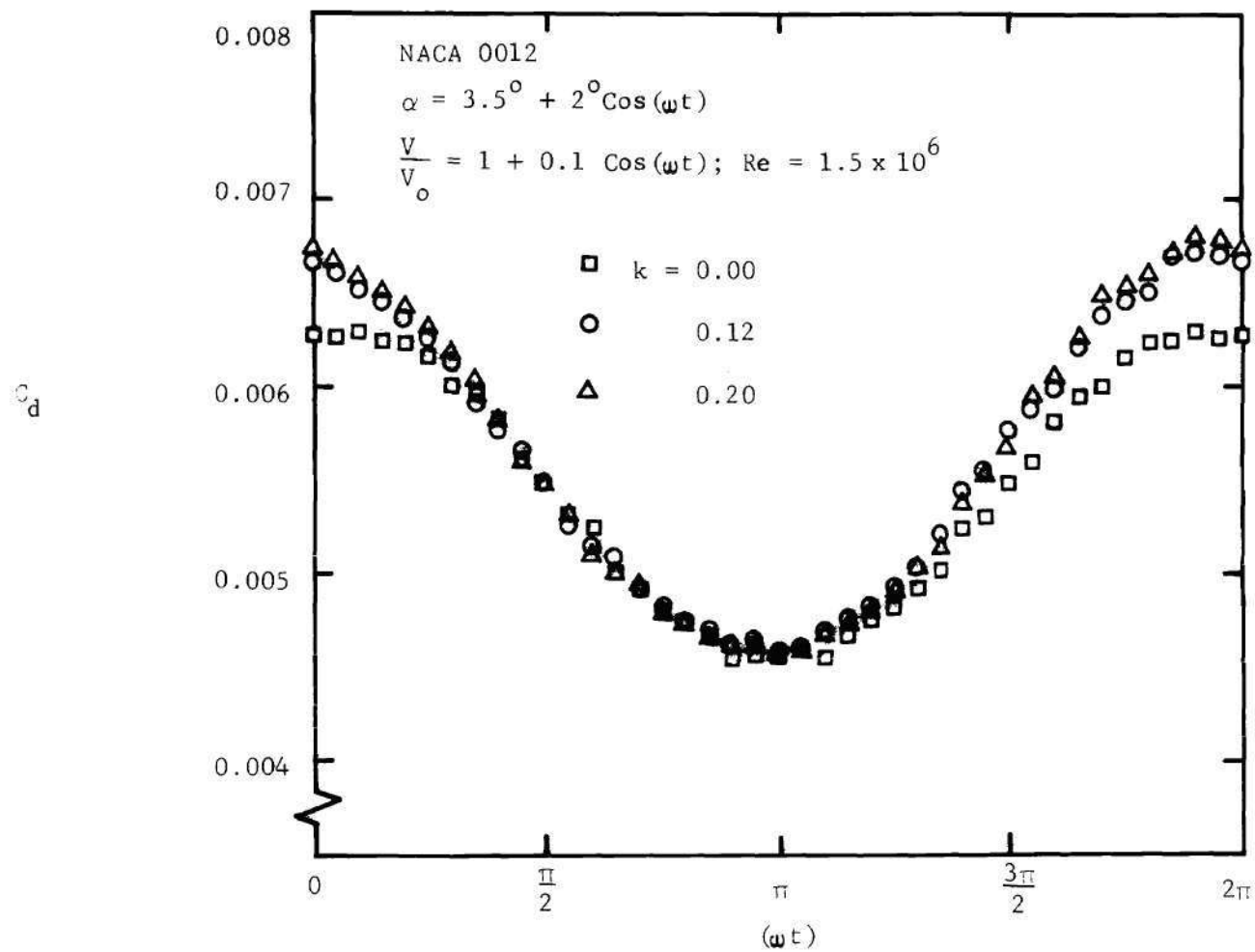


Figure 25. Variation of Drag with Time, Effect of Reduced Frequency,  $k$

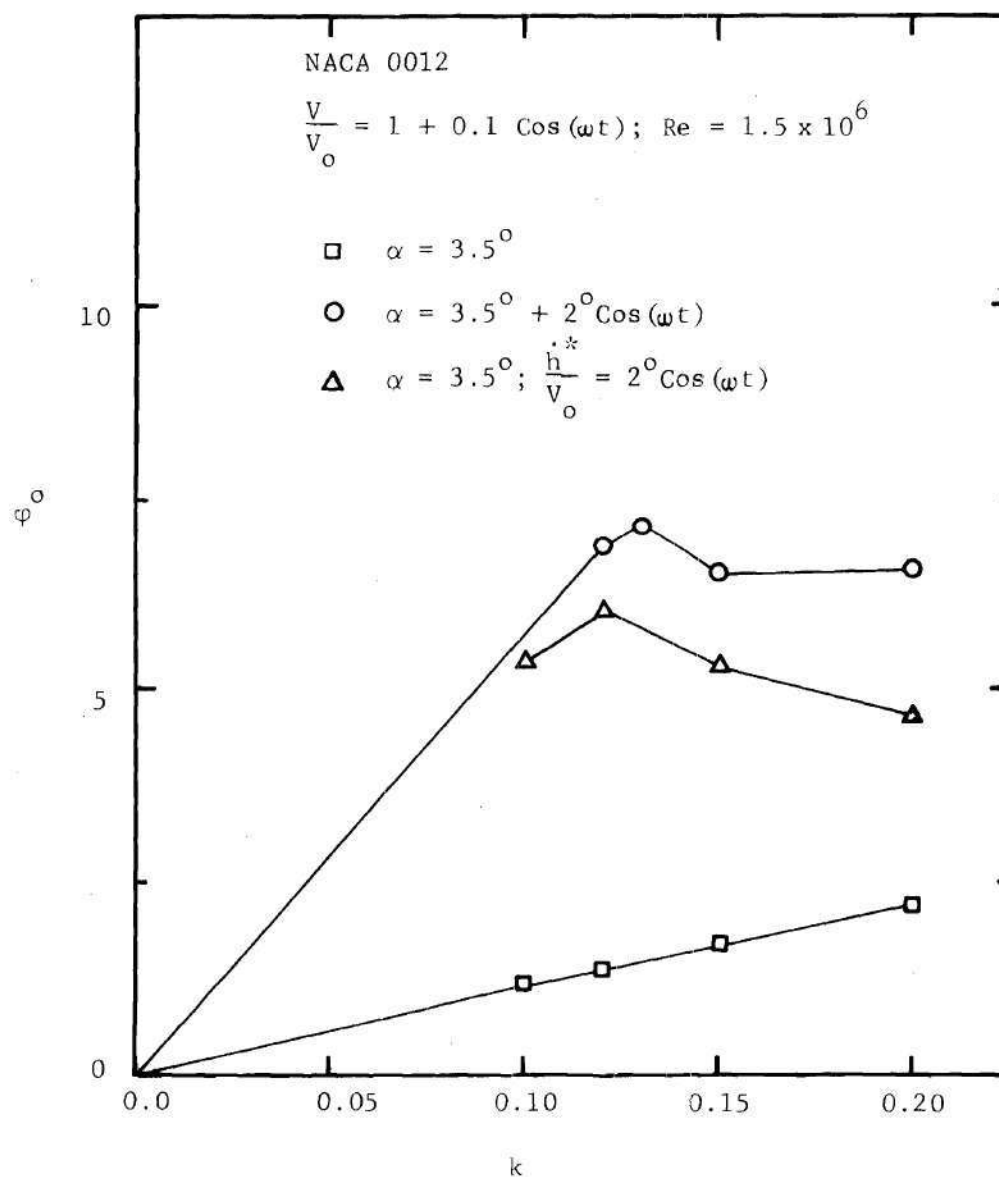


Figure 26. Variation of Phase,  $\phi$ , with Reduced Frequency,  $k$

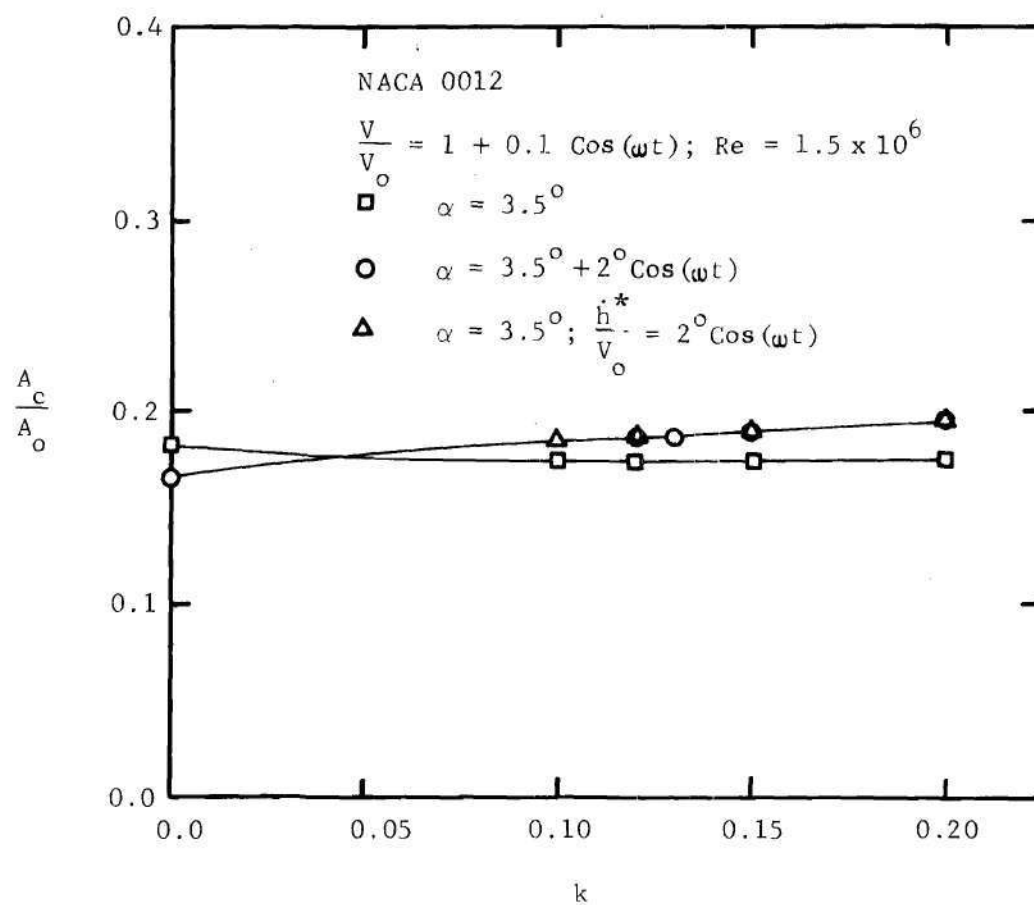


Figure 27. Variation of Amplitude Ratio,  $A_c/A_o$ , with Reduced Frequency,  $k$

$\varphi$  and  $k$ , over those employed for the laminar flow results. Three cases were investigated:  $\alpha = 3.5^\circ$ ,  $\alpha = 3.5^\circ + 2^\circ \cos(\omega t)$ , and  $\alpha = 3.5^\circ$  with  $\dot{h}^*/V_0 = 2^\circ \cos(\omega t)$ . The free stream was specified as  $V/V_0 = 1 + 0.1 \cos(\omega t)$  and  $Re$  was equal to  $1.5 \times 10^6$ . The range of investigation for the reduced frequency was 0.00 to 0.20. The constant  $A_0$  was found to be nearly the same for all the cases, the maximum difference from 0.005549 being 1.7%. For each condition the ratio  $A_c/A_0$  was obtained by using the respective  $A_0$ .

It can be seen from Figure 26 that the turbulent phase advance is quite small and, in general, much less than the laminar phase, Figure 15. This is in agreement with McCroskey and Philippe's [30] results for the flat plate at zero incidence. For the  $\alpha = 3.5^\circ$  case the phase increases linearly with the reduced frequency. Recall that the transition points are stationary for this condition. Hence, this linear increase is purely due to the effect of unsteadiness ( $k$ ) on the combined laminar and turbulent skin frictions. The non-stationary airfoil results are considered now. Both cases show a higher phase compared to the constant incidence condition. The presumable causes for this behavior have been discussed in the previous section: the opposite effects and the hysteresis type movement of the two transition points. The phase variation is not as definite as in the completely laminar condition. There appears to be a leveling off trend in the phase. Recall that at  $k = 0.20$  the upper transition point movement appeared to have greater influence compared to the lower one. The former movement brings about changes in the drag that are always in phase with the angle of attack variation which, in the present case is of

the same type as the free stream variation,  $\cos(\omega t)$ . This would lead to a reduction in the phase,  $\varphi$ , and might explain the above leveling off.

Figure 27 shows that for the  $\alpha = 3.5^\circ$  condition the amplitude ratio is almost independent of the reduced frequency. This is in agreement with the flat plate skin friction results of McCroskey and Philippe [30]. For the non-stationary airfoil cases the amplitude ratio increases with the reduced frequency. Note that at  $k = 0.00$ ,  $A_c/A_o$  for  $\alpha = 3.5^\circ$  is larger than that for  $\alpha = 3.5^\circ + 2^\circ \cos(\omega t)$ . The reverse is true at  $k = 0.20$ . Recall that a detailed discussion of these trends was presented in the previous section. A comparison of Figures 16 and 27 shows that the laminar amplitude ratio is less than the turbulent ratio for the range of reduced frequency considered. For values of the local reduced frequency,  $\omega d/V_o$ , less than 0.5, McCroskey and Phillippe's flat plate skin friction amplitude ratios also have the same behavior.

Finally, as Figures 26 and 27 show, the variations for the oscillating angle of attack and translating airfoils are very similar to each other. Reference should be made to the section on laminar flow results for details regarding the difference in the respective downwashes.

#### Effects due to the Amplitude of Free Stream Fluctuations

Presented in Figure 28 is a set of drag variations with time and  $\sigma$  for the oscillating angle of attack airfoil. For  $\sigma = 0.00$  the drag appears to be almost unvarying with time. This is quite unlike the behavior of the  $\sigma = 0.00$  curve in Figure 11a for the laminar case. Recall that the rather significant variation in the laminar drag was largely

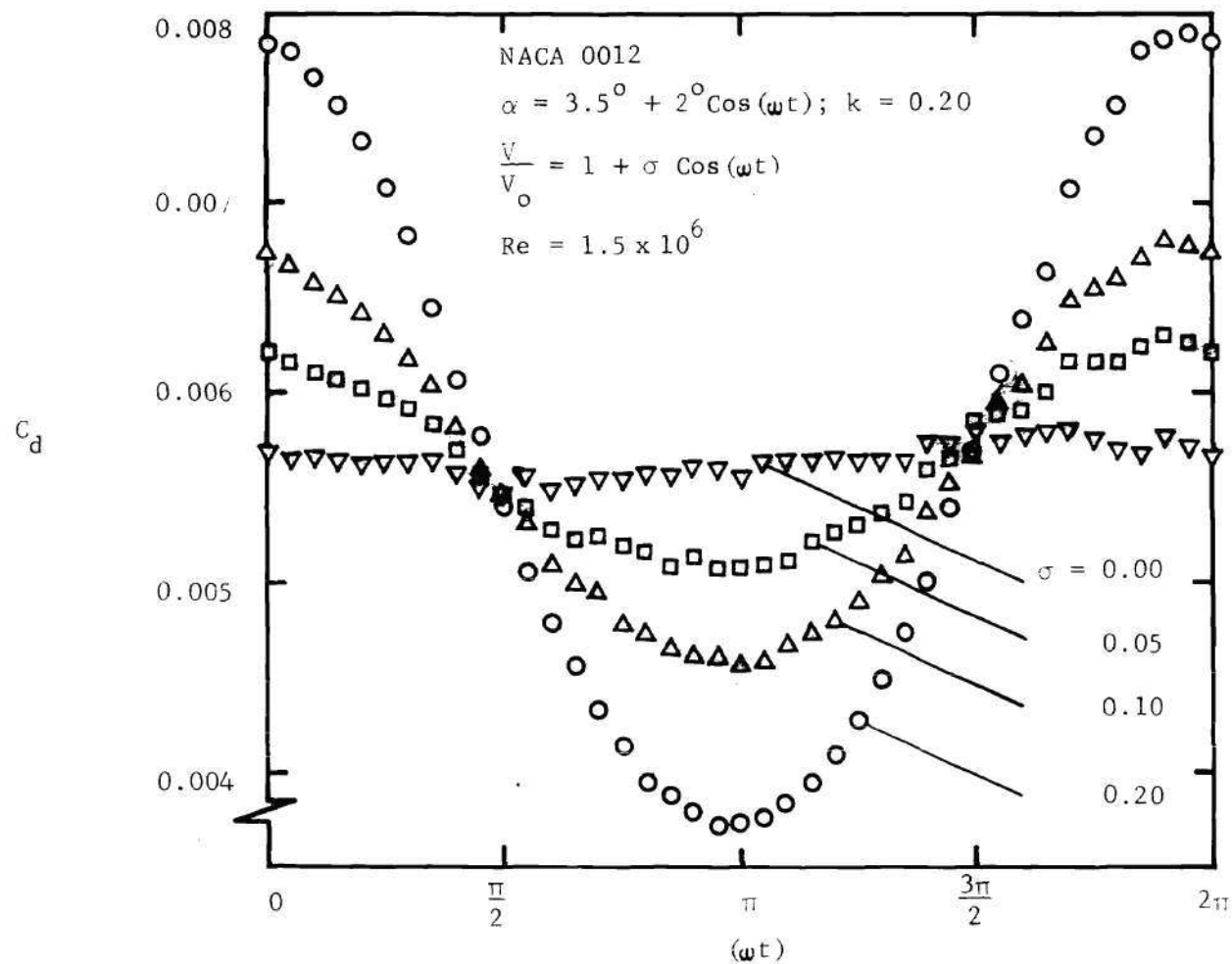


Figure 28. Variation of Drag with Time, Effect of  $\sigma$

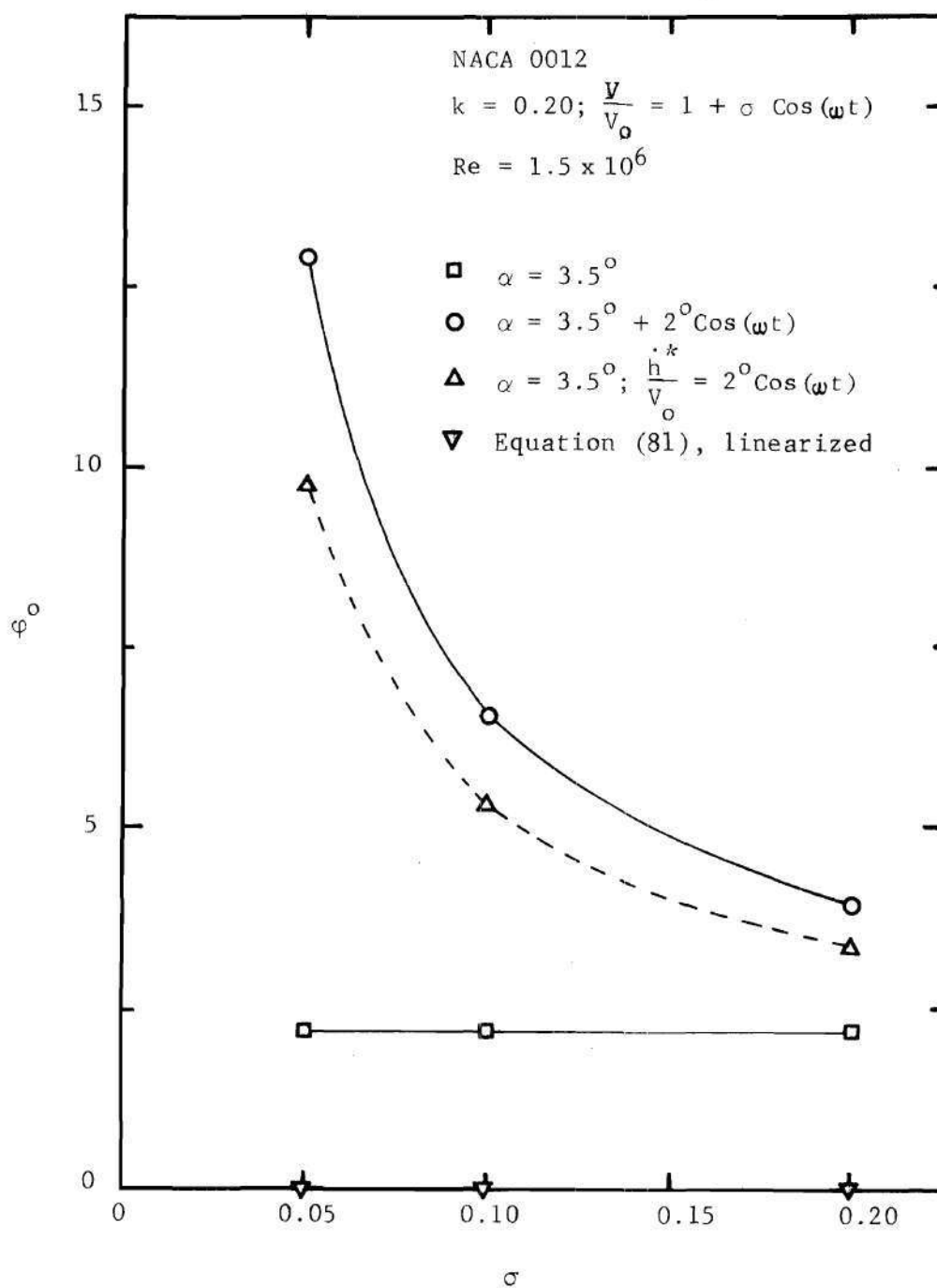


Figure 29. Variation of Phase,  $\phi$ , with  $\sigma$

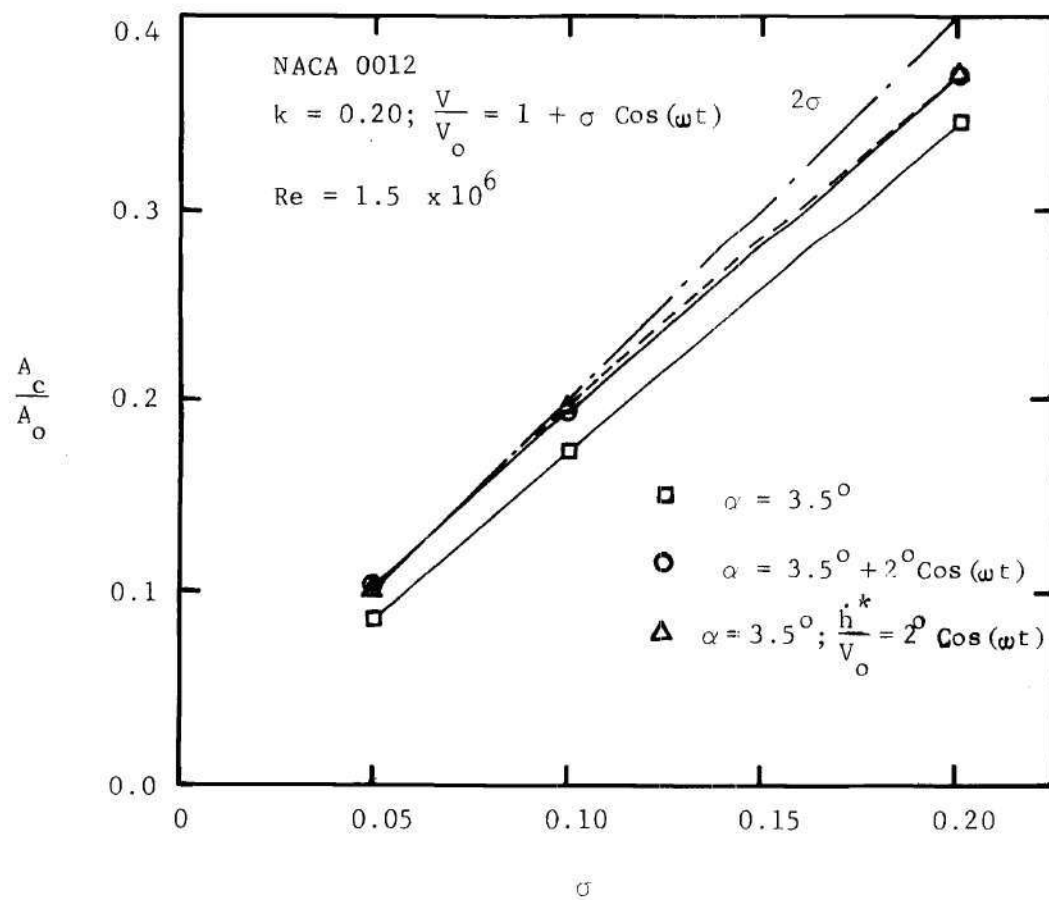


Figure 30. Variation of Amplitude Ratio,  $A_c/A_o$ , with  $\sigma$



due to the movement of the upper surface zero wall shear location. However, as pointed out during the preliminary discussion the turbulent wall shear is never zero and both upper and lower transition point movements are important, and have opposite effects on the drag changes. Presumably, for  $\sigma = 0.00$  they almost cancel each other out.

All the variations in Figure 28 appear to intersect each other twice, very near  $\omega t = \pi/2$  and  $3\pi/2$ . At these times  $V/V_0 = 1.0$  and the drag irrespective of  $\sigma$ , takes on a value corresponding to that of the constant free stream case. This behavior was observed for the completely laminar condition also. It is evident from the figure that the amplitude of the drag fluctuation increases with increasing  $\sigma$ . The effect of  $\sigma$  on the phase is not so clearly discernible.

Figures 29 and 30 show the phase and amplitude ratio variations with  $\sigma$  for three cases:  $\alpha = 3.5^\circ$ ,  $\alpha = 3.5^\circ + 2^\circ \cos(\omega t)$ , and  $\alpha = 3.5^\circ$  with  $\dot{h}^*/V_0 = 2^\circ \cos(\omega t)$ . The free stream velocity was  $V/V_0 = 1 + \sigma \cos(\omega t)$  and the values of  $\sigma$  investigated were: 0.05, 0.10, and 0.20. The reduced frequency was equal to 0.20 and the Reynolds number was specified as  $1.5 \times 10^6$ . For all conditions the constant  $A_0$  was within 2.2% of 0.005592. The ratio  $A_c/A_0$  for each case was obtained by using the respective  $A_0$ .

The phase advance for the  $\alpha = 3.5^\circ$  condition is independent of  $\sigma$  and is approximately equal to  $2.2^\circ$  as can be observed from Figure 29. Recall that transition points for this case are stationary. The phase advances for the other two cases in the figure are greater, and the presumable reasons for this have been noted in the previous section. The non-stationary airfoil phases decrease with increasing  $\sigma$  and appear to

approach  $2.2^\circ$ . This behavior can be explained by a consideration of the transition point curves (similar to Figures 23 and 24). It was observed from the computations that an increase in  $\sigma$  causes a general reduction in the area enclosed by the transition curves, i.e. the total travels decrease. The effect of this "tightening" is to diminish the respective differences between the stationary locations for the  $\alpha = 3.5^\circ$  condition and the corresponding points for the other two cases in Figure 29. Hence, with regard to the phase only, an increase in  $\sigma$  tends to suppress the effects of the angle of attack oscillations (and translations). Recall that the completely laminar case also showed a similar behavior, though the basic reason was different.

As can be seen from Figure 30 the amplitude ratio is linearly dependent on  $\sigma$ . For the non-stationary airfoil cases the ratios are higher than the value for the constant incidence condition. This behavior has been considered in detail during the preliminary discussion.

Both Figures 29 and 30 show that the variations for the translating airfoil are very similar to the ones for the oscillating angle of attack airfoil. Reference should be made to the section on laminar flow results for details regarding the difference in the respective downwashes.

Also presented in Figures 29 and 30 are the phase and amplitude ratio variations obtained from the linearized form of Equation (81), which assumes a constant drag coefficient. As noted earlier, with regard to Figures 12 and 13, this approximation gives the phase to be always zero and the amplitude ratio to be  $2\sigma$ . That the phase is not at all predicted by this representation can be seen from Figure 29. The

amplitude ratio variation,  $2\sigma$ , differs considerably, by approximately 15%, from the curve for the stationary airfoil, Figure 30. However, for  $\sigma \lesssim 0.10$  the variation for the non-stationary airfoil is close to the  $2\sigma$  representation.

### Effects due to Phase Difference Between Stream Fluctuations and Airfoil Oscillations

Figures 31 and 32 show the effect of  $\psi$  on the phase and amplitude ratio for three values of the reduced frequency. The free stream velocity was specified as  $V/V_0 = 1 + 0.1 \cos(\omega t)$  with an angle of attack variation of  $\alpha = 3.5^\circ + 2^\circ \cos(\omega t + \psi)$ , and  $Re = 1.5 \times 10^6$ . Computations were performed for  $\psi = 0, \pi/2, \pi$ , and  $3\pi/2$ . For each  $\psi$  the following values of the reduced frequency were investigated: 0.00, 0.12, and 0.20. For all cases, the constant  $A_0$  was within 2% of 0.005557, the respective  $A_0$  being used to obtain  $A_c/A_0$  in each case.

Figure 31 shows that the turbulent phase is greatly influenced by variations in  $\psi$ . The phase undergoes not only large percentage changes in magnitude but also a change in sign, i.e. the drag can either lead or lag the free stream velocity. It is important to note that for values of  $\psi = \pi$  and  $3\pi/2$ , an increase in the reduced frequency can increase the phase lag (or decrease the lead). This is quite unlike the behavior for the laminar condition where an increase in the reduced frequency makes the phase more positive for all values of  $\psi$ , Figure 17.

Note that the  $k = 0.00$  variations of Figures 17 and 31 are similar to each other, although of course these variations arise due to entirely different reasons. For the laminar curve, the interpretation was based on a consideration of the movement of the zero wall shear

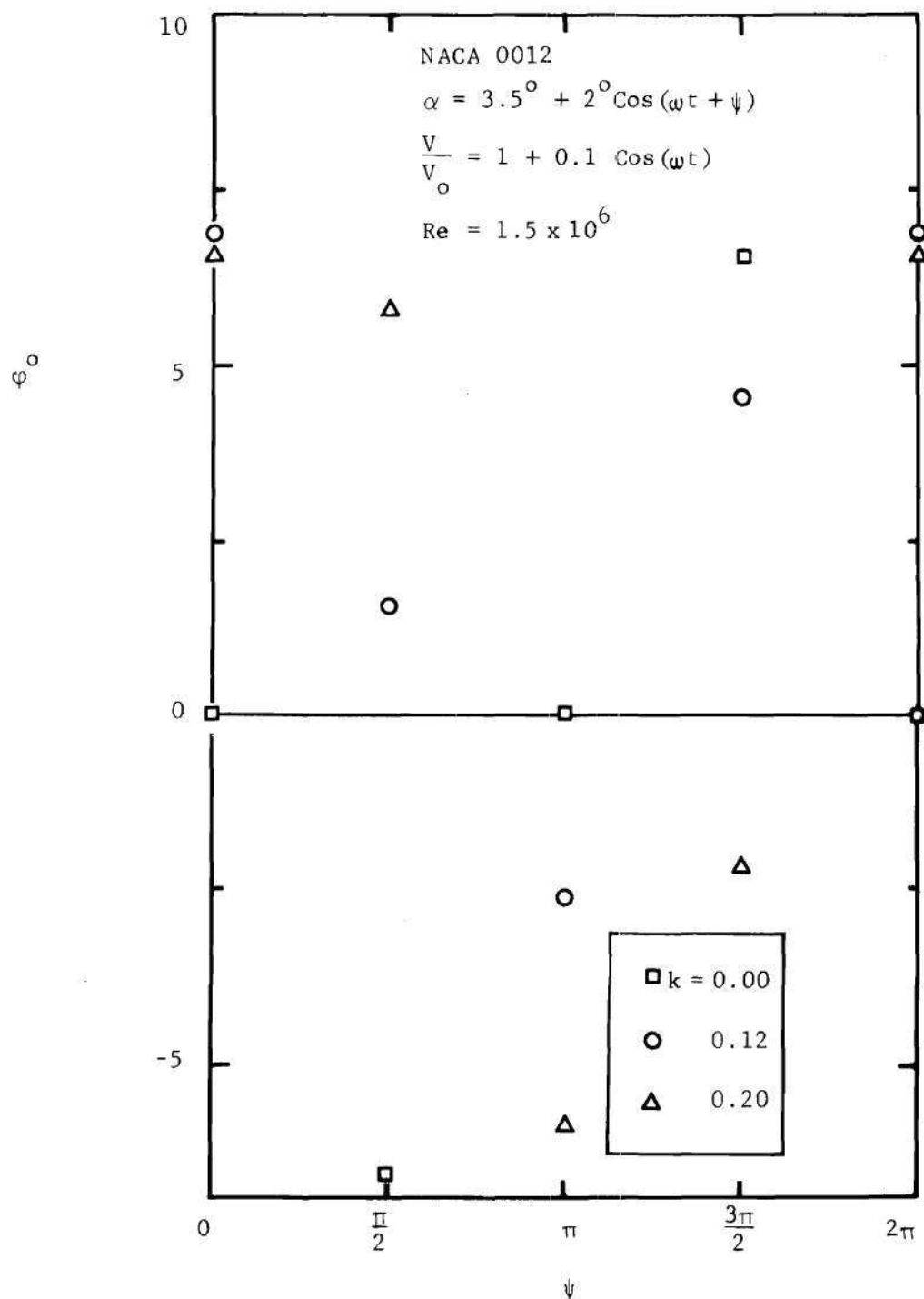


Figure 31. Variation of Phase,  $\phi$ , with Phase Difference,  $\psi$ , and Reduced Frequency,  $k$

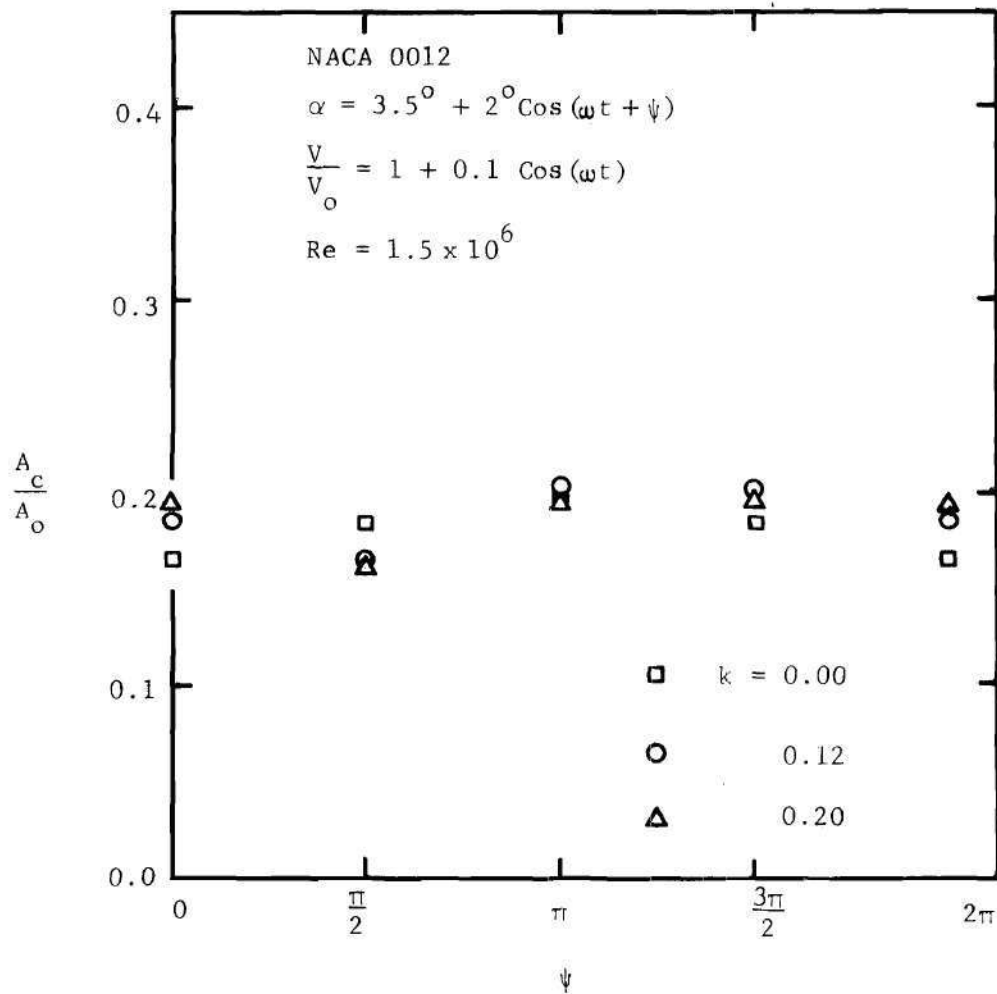


Figure 32. Variation of Amplitude Ratio,  $A_c/A_o$ , with Phase Difference,  $\psi$ , and Reduced Frequency,  $k$

location. For an interpretation of the turbulent variation one must consider the movements of the two transition points, as follows. It can be shown that when  $k = 0.00$  and  $\sigma = 0.00$  the contribution of the lower transition point location movement is such that, at  $\psi = 0, \pi/2, \pi$ , and  $3\pi/2$ ,  $\phi$  is equal to  $180^\circ, -90^\circ, 0^\circ$ , and  $90^\circ$ , respectively; the upper contribution is  $0^\circ, 90^\circ, 180^\circ$ , and  $-90^\circ$ . The introduction of a non-zero  $\sigma$  would impose a quasi-steady variation (zero phase). For a sufficiently large  $\sigma$  the  $180^\circ$  shifts would be overcome completely resulting in zero phase shifts, and, the magnitudes of the other ( $90^\circ$ ) shifts would be reduced, the sign being unchanged. Thus, the phase lag at  $\psi = \pi/2$  and the lead at  $\psi = 3\pi/2$  implies that, for all values of  $\psi$ , at  $k = 0.00$  the lower surface transition point movement is the dominant one. Recall that in the preliminary discussion,  $\psi = 0$ , the same conclusion was reached from an argument that is basically the same as the above. For some other value of the reduced frequency, say 0.20, the upper location movement exerts a greater influence, resulting in a phase lead at  $\psi = \pi/2$  and a lag at  $\psi = 3\pi/2$ , a reversal of the behavior at  $k = 0.00$ .

The  $A_c/A_o$  variation of Figure 32 is considered now. In general, the percentage changes are less compared to the laminar case, Figure 18. For  $k = 0.00$  the maxima and minima at  $\psi = \pi$  and 0, respectively, can be explained by the same considerations as those employed for Figure 31. At non-zero reduced frequencies there appears to be a rightward shift of the maxima, similar to that of the laminar case.

The variations of  $\phi$  and  $A_c/A_o$  with  $\psi$  and  $\sigma$  are considered now. Figures 33 and 34 show these effects for four values of  $\psi$  and three

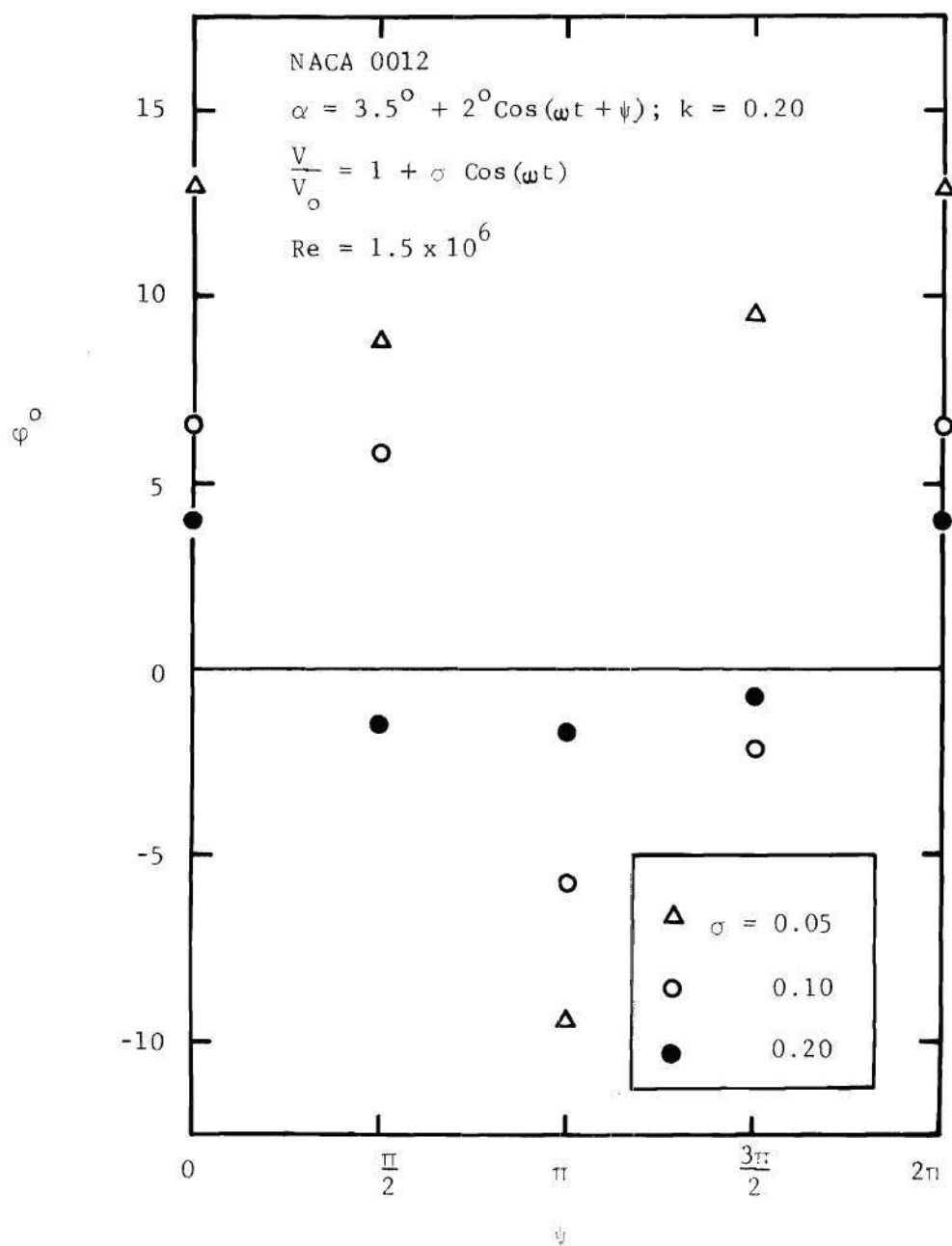


Figure 33. Variation of Phase,  $\phi$ , with Phase Difference,  $\psi$ , and  $\sigma$

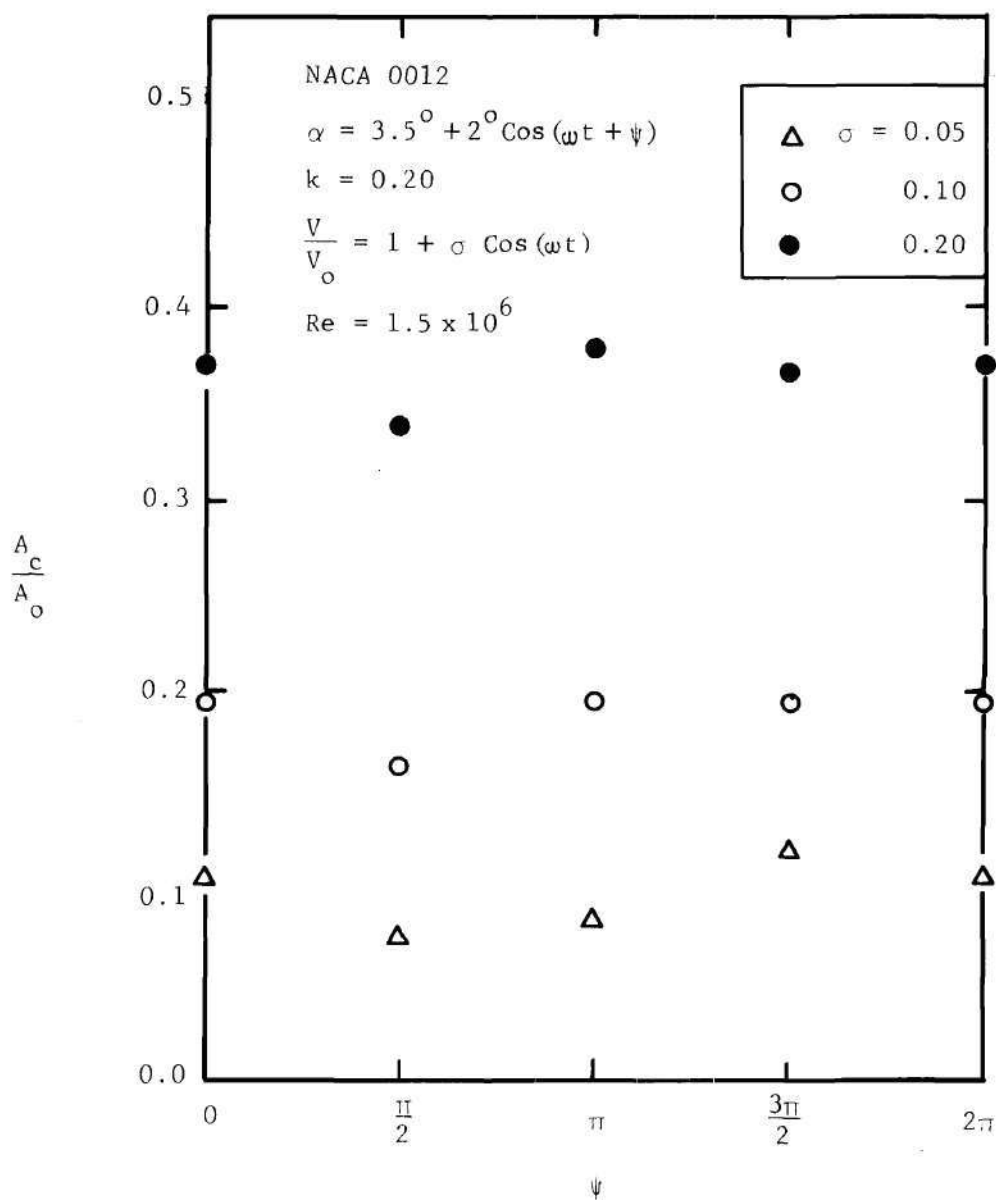


Figure 34. Variation of Amplitude Ratio,  $A_c/A_o$ , with Phase Difference,  $\psi$ , and  $\sigma$



different  $\sigma$ 's. The reduced frequency and Reynolds number were equal to 0.20 and  $1.5 \times 10^6$ , respectively. For all cases, the constant  $A_0$  was within 2% of 0.005636, the respective  $A_0$  being used to obtain  $A_c/A_0$ .

Figure 33 shows that an increase in  $\sigma$  smoothens out the variations in  $\varphi$  with respect to  $\psi$ . Recall that a "limit"  $\varphi$  was introduced in the laminar case. The corresponding turbulent "limit"  $\varphi$  appears to be close to  $0^\circ$  for  $k = 0.20$  and would be  $0^\circ$  for  $k = 0.00$ . Note that in the  $\alpha = 3.5^\circ$  case,  $\varphi = 2.2^\circ$  for  $k = 0.20$ , Figure 29. Therefore, the same conclusion as in the laminar case can be derived from these observations. Namely, as the amplitude of the free stream fluctuations increases the tendency for all values of  $\psi$ , is to suppress the phase effects of the angle of attack oscillations, and only the airfoil at a constant incidence is "seen" by the free stream.

Recall that for  $\psi = 0$  the amplitude ratio varied linearly with  $\sigma$ , Figure 30. The same dependency appears to hold for all values of  $\psi$ , as can be seen from Figure 34.

#### Remarks about Drag Superposition

In an attempt to superpose the drag in a manner similar to that for the laminar case the following three cases were considered: 1)  $\alpha = 3.5^\circ$  with  $V/V_0 = 1 + \sigma \cos(\omega t)$ , 2)  $\alpha = 3.5^\circ + 2^\circ \cos(\omega t + \psi)$  with  $V/V_0 = 1$ , and 3)  $\alpha = 3.5^\circ + 2^\circ \cos(\omega t + \psi)$  with  $V/V_0 = 1 + \sigma \cos(\omega t)$ . Recall that in the laminar case the drag corresponding to the third case could be obtained by a superposition of the other two drags.

It was found that such an approach for the turbulent condition results in large errors, especially in the values for the phase. Seve-

ral conditions were investigated:  $Re = 1.5 \times 10^6$ ,  $0.05 \leq \sigma \leq 0.20$ ,  $0.00 \leq k \leq 0.20$ , and  $0 \leq \psi \leq 2\pi$ . The maximum errors in  $A_c/A_o$  and  $\varphi$  were, respectively, 18% and 48%. The fact that the above approach was successful under laminar conditions implied some kind of a linear behavior for drag. The same cannot be said when the flow is turbulent.

### Reynolds Number Dependency

Three values of  $Re$  were investigated:  $10^6$ ,  $1.5 \times 10^6$ , and  $2 \times 10^6$ , with  $k = 0.20$  and  $V/V_o = 1 + 0.1 \cos(\omega t)$ . Both the constant,  $\alpha = 3.5^\circ$ , and varying,  $\alpha = 3.5^\circ + 2^\circ \cos(\omega t)$ , incidences were considered. The results are presented in Table 2. The phase shows a definite dependency on the Reynolds number. The amplitude ratio varies slightly with  $Re$  but a definite trend is absent. Note that for  $\alpha = 3.5^\circ$  the phase decreases with increasing Reynolds number, a trend that is reverse of the one shown for  $\alpha = 3.5^\circ + 2^\circ \cos(\omega t)$ . The above dependencies are not unexpected since the transition points and the eddy viscosity are functions of the Reynolds number. Finally, it is noted that McCroskey and Philippe's [30] flat plate skin friction phase and amplitude ratio distribution also have a Reynolds number dependency.

Table 2. Drag Dependency on Reynolds Number

	$Re = 10^6$	$1.5 \times 10^6$	$2 \times 10^6$	
$A_o$	0.005715	0.005483	0.005417	$\left[ \begin{array}{l} \alpha = 3.5^\circ \\ k = 0.20 \\ \frac{v}{v_o} = 1 + 0.1 \cos(\omega t) \end{array} \right.$
$A_c/A_o$	0.173	0.174	0.175	
$\varphi^\circ$	2.6	2.2	2.0	
$A_o$	0.005874	0.005628	0.005465	$\left[ \begin{array}{l} \alpha = 3.5^\circ + 2^\circ \cos(\omega t) \\ k = 0.20 \\ \frac{v}{v_o} = 1 + 0.1 \cos(\omega t) \end{array} \right.$
$A_c/A_o$	0.194	0.195	0.188	
$\varphi^\circ$	6.2	6.6	8.0	

## CHAPTER V

### CONCLUSIONS AND RECOMMENDATIONS

An analytical investigation regarding the unsteady skin friction drag of an oscillating airfoil in a fluctuating free stream has been performed. First, an approximate unsteady potential flow analysis for an airfoil that pitches and/or flaps in a fluctuating free stream was developed. The flow was considered to be incompressible and two-dimensional. Further, all oscillations and fluctuations were assumed to be small, simple harmonic in time, and to have the same frequency. Next, using the resulting pressure distribution the time-dependent boundary layer was analyzed with the method of finite differences. The analysis allowed for both laminar and turbulent conditions. The skin friction thus obtained was then integrated to get the drag. Lastly, several parameters associated with the flow problem were varied systematically so that their influence on the unsteady drag could be determined.

#### Conclusions

The results of the study indicate that the following conclusions can be drawn.

1. The introduction of fluctuations in the free stream velocity alters the skin friction drag considerably by causing significant fluctuations in the drag. Further,

- i) For the range of conditions investigated, the amplitude of the drag fluctuations increases linearly with the amplitude of

the free stream fluctuations.

ii) The phase lead, over the free stream velocity fluctuations, of the drag fluctuations is almost independent of the amplitude of free stream fluctuations for the constant incidence airfoil. For the airfoil undergoing oscillations about a mean angle of attack, even the nature of the phase (of the drag fluctuations) variation with the amplitude of free stream fluctuations is a strong function of the phase difference between the free stream fluctuations and airfoil oscillations. An increase in the amplitude of the free stream fluctuations suppresses the variations in the phase (of the drag fluctuations) that occur due to the changes in the phase difference between the free stream fluctuations and airfoil oscillations. The result of such a smoothing is, apparently, to reduce the difference between the drag phases of the constant incidence airfoil and the one undergoing oscillations about the same constant angle of attack.

2. In general, a variation in the reduced frequency causes a greater percentage change in the phase of the drag fluctuations than in their amplitude. Further, for the range of conditions investigated:

i) For the constant incidence airfoil under laminar conditions, Reynolds number  $\sim 10^5$ , the amplitude of the drag fluctuations increases with the reduced frequency. However, the amplitude of the drag fluctuations decreases slightly with an increase in the reduced frequency when the constant incidence airfoil is under laminar-turbulent conditions, Reynolds number  $\sim 10^6$ . For the airfoil undergoing oscillations about a mean angle of attack, even the nature of the amplitude (of the drag fluctuations) variation with the reduced frequency

is a strong function of the phase difference between the free stream fluctuations and airfoil oscillations.

ii) Under laminar conditions, an increase in the reduced frequency tends to make the phase of the drag fluctuations more positive. It increases the phase lead over the free stream or diminishes the phase lag, if there is a lag to start with. For the laminar-turbulent condition, the phase lead of the drag fluctuations increases with the reduced frequency when the airfoil incidence is constant. Also in the high Reynolds number case, for an airfoil undergoing oscillations about a mean angle of attack, even the nature of the phase (of the drag fluctuations) variation with the reduced frequency is a strong function of the phase difference between the free stream fluctuations and airfoil oscillations.

3. For the range of conditions investigated, there is a significant difference in the phase and amplitude of the drag fluctuations for the constant incidence airfoil and the one undergoing oscillations about the same constant angle of attack.

4. For the airfoil undergoing oscillations about a mean incidence, both phase and amplitude of the drag fluctuations are a strong function of the phase difference between the free stream fluctuations and airfoil oscillations. Depending on the values of this phase difference, reduced frequency, and amplitude of free stream fluctuations, the drag can either lead or lag the free stream velocity.

5. For the range of conditions investigated, in general, the magnitude of the phase of drag fluctuations under laminar conditions, Reynolds number  $\sim 10^5$ , is considerably higher than the value under

laminar-turbulent conditions, Reynolds number  $\sim 10^6$ . The reverse is true for the amplitude of the drag fluctuations, the laminar values being lower than those under laminar-turbulent conditions.

6. Consider the following three cases: i)  $\alpha = 2^\circ$  with  $\left(\frac{V}{V_0}\right) = 1 + \sigma \cos(\omega t)$ , ii)  $\alpha = 2^\circ + 2^\circ \cos(\omega t + \psi)$  with  $\left(\frac{V}{V_0}\right) = 1$ , and iii)  $\alpha = 2^\circ + 2^\circ \cos(\omega t + \psi)$  with  $\left(\frac{V}{V_0}\right) = 1 + \sigma \cos(\omega t)$ . Under laminar conditions, Reynolds number  $\sim 10^5$ , for the range of conditions investigated, a superposition of the perturbation skin friction drag of the first two cases gives the perturbation drag of the third case to within two percent.

7. Consider the following three cases: i)  $\alpha = 3.5^\circ$  with  $\left(\frac{V}{V_0}\right) = 1 + \sigma \cos(\omega t)$ , ii)  $\alpha = 3.5^\circ + 2^\circ \cos(\omega t + \psi)$  with  $\left(\frac{V}{V_0}\right) = 1$ , and iii)  $\alpha = 3.5^\circ + 2^\circ \cos(\omega t + \psi)$  with  $\left(\frac{V}{V_0}\right) = 1 + \sigma \cos(\omega t)$ . Under laminar-turbulent conditions, Reynolds number  $\sim 10^6$ , for the range of conditions investigated, the skin friction drag in the third case cannot be obtained by a superposition of the other two cases without incurring large errors, approximately 20%.

8. For the laminar-turbulent condition, Reynolds number  $\sim 10^6$ , both phase and amplitude ratio of the drag fluctuations show a dependency on the Reynolds number. This is unlike the behavior for the laminar case, Reynolds number  $\sim 10^5$ , where the phase and amplitude ratio of the drag fluctuations are independent of the Reynolds number.

9. For all practical purposes, the mean drag coefficient is a function of only the Reynolds number.

10. In general, the effects on the drag of angle of attack oscillations and vertical translations are very similar to each other

when the mean incidences and the equivalent oscillatory variations are the same for both types of motion.

11. The amplitude ratio of the drag fluctuations obtained from the linearized form of Equation (81) differs considerably, by at least 25%, from the actual value under laminar conditions, Reynolds number  $\sim 10^5$ . For the laminar-turbulent condition, Reynolds number  $\sim 10^6$ , the agreement is better. For the constant incidence airfoil the difference is approximately 15%. However, for the airfoil undergoing oscillations about a mean angle of attack, in the higher Reynolds number case the two variations are close to each other for  $\sigma \lesssim 0.10$ . In any case, the phase of the drag fluctuations is not at all predicted by the linearized form of Equation (81).

#### Recommendations

1. Most importantly, the results of the present study should be employed in an existing rotor blade stability analysis to determine the effect of unsteady drag on the stability of in-plane oscillations.

2. Probably one of the greatest needs is a comprehensive experimental program to investigate airfoil drag under time-dependent conditions. Such a program would serve to corroborate the results of the present analytical study.



## APPENDIX A

FINITE DIFFERENCE REPRESENTATIONS AND  
DIFFERENCE EQUATIONS

This appendix contains the difference representations and the final difference equations corresponding to the momentum and continuity equations. The Crank-Nicolson method is employed for the laminar case and a fully implicit scheme is used for the turbulent case. In both cases the resulting set of difference equations have a tridiagonal matrix form.

Difference Representations

Let  $i, j$  and  $m$  be the indices for  $\xi$ ,  $\eta$  and  $\tau$ , respectively. In the following relations the constants  $c$  and  $d$  are such that, for the laminar case  $c = d = \frac{1}{2}$  and for the turbulent case  $c = 1$ ,  $d = 0$ .

$$g = cg_{i+1,j}^m + dg_{i,j}^m$$

$$\frac{\partial g}{\partial \xi} = \frac{(g_{i+1,j}^m - g_{i,j}^m)}{\Delta \xi_i}$$

$$\frac{\partial g}{\partial \eta} = \frac{1}{(1+r)\Delta \eta_j} \left[ c(g_{i+1,j+1}^m - g_{i+1,j-1}^m) + d(g_{i,j+1}^m - g_{i,j-1}^m) \right]$$

$$\frac{\partial^2 g}{\partial \eta^2} = \frac{2}{r(1+r)} (\Delta \eta_j)^2 \left[ c \left( g_{i+1,j+1}^m - (1+r) g_{i+1,j}^m + r g_{i+1,j-1}^m \right) \right. \\ \left. + d \left( g_{i,j+1}^m - (1+r) g_{i,j}^m + r g_{i,j-1}^m \right) \right]$$

$$\frac{\partial g}{\partial \tau} = \frac{1}{\Delta \tau_m} \left[ c \left( g_{i+1,j}^m - g_{i+1,j}^{m-1} \right) + d \left( g_{i,j}^m - g_{i,j}^{m-1} \right) \right]$$

where

$$\Delta \xi_i = \xi_{i+1} - \xi_i$$

$$\Delta \eta_j = \eta_j - \eta_{j-1}$$

$$r = \frac{\Delta \eta_{j+1}}{\Delta \eta_j} \quad (=1 \text{ for the laminar case})$$

$$\Delta \tau_m = \tau_m - \tau_{m-1}$$

### Difference Equations

In both cases the nonlinear terms are linearized by the use of previous  $\xi$  values. For the laminar case this is found to be adequate, whereas, an iterative process is required for updating the turbulent transport properties. In the laminar case (Crank-Nicolson scheme) the independent variable  $\xi$  is evaluated at station  $(i + \frac{1}{2})$ . For the turbulent case this evaluation is done at station  $(i + 1)$ . With the preceding difference representations the momentum equation (71) then takes the following tridiagonal form

$$A_j g_{i+1,j+1}^m + B_j g_{i+1,j}^m + C_j g_{i+1,j-1}^m = D_j \quad (j=2 \text{ to } N-1)$$

where  $j=1$  and  $j=N$  are the indices for the wall and the boundary layer edge, respectively. For the laminar case the coefficients  $A_j$ ,  $B_j$ ,  $C_j$  and  $D_j$  are given by

$$A_j = \frac{\Delta \xi_i}{4\Delta\eta} \left( h_{i,j}^m - \frac{1}{\Delta\eta} \right)$$

$$B_j = \left( \frac{k\xi}{2U_e} \right) \frac{\Delta \xi_i}{\Delta\tau_m} + \left( \xi + \frac{1}{2} \beta_x \Delta \xi_i \right) g_{i,j}^m + \frac{1}{2} \beta_t \Delta \xi_i + \frac{\Delta \xi_i}{2(\Delta\eta)^2}$$

$$C_j = \frac{-\Delta \xi_i}{4\Delta\eta} \left( h_{i,j}^m + \frac{1}{\Delta\eta} \right)$$

$$D_j = \left( \frac{k\xi}{2U_e} \right) \frac{\Delta \xi_i}{\Delta\tau_m} \left( g_{i+1,j}^{m-1} + g_{i,j}^{m-1} \right) + \frac{\Delta \xi_i}{4\Delta\eta} \left( -h_{i,j}^m + \frac{1}{\Delta\eta} \right) g_{i,j+1}^m$$

$$- \frac{1}{2} \Delta \xi_i \left( \frac{k\xi}{U_e} + \frac{1}{\Delta\tau_m} + \beta_t + \frac{1}{(\Delta\eta)^2} \right) g_{i,j}^m$$

$$+ \frac{\Delta \xi_i}{4\Delta\eta} \left( h_{i,j}^m + \frac{1}{\Delta\eta} \right) g_{i,j-1}^m + \left( \xi - \frac{1}{2} \beta_x \Delta \xi_i \right) \left( g_{i,j}^m \right)^2$$

$$+ \Delta \xi_i \left( \beta_t + \beta_x \right)$$

where  $U_e$ ,  $\beta_x$  and  $\beta_t$  are evaluated at  $\xi = \xi_i$  and  $\tau = \tau_m$ .

For turbulent flow the coefficients are given by

$$A_j = \frac{\Delta \xi_i}{(1+r)\Delta \eta_j} \left[ h_{i,j}^m - \frac{\ell_{i+1,j}^m}{r\Delta \eta_j} - \frac{1}{2(1+r)\Delta \eta_j} (\ell_{i+1,j+1}^m - \ell_{i+1,j-1}^m) \right]$$

$$B_j = \left( \frac{k\xi}{U_e} \right) \frac{\Delta \xi_i}{\Delta \tau_m} + \left( \xi + \beta_x \Delta \xi_i \right) g_{i,j}^m + \beta_t \Delta \xi_i + \frac{\Delta \xi_i}{r(\Delta \eta_n)^2} \ell_{i+1,j}^m$$

$$C_j = \frac{-\Delta \xi_i}{(1+r)\Delta \eta_j} \left[ h_{i,j}^m + \frac{\ell_{i+1,j}^m}{\Delta \eta_j} - \frac{1}{2(1+r)\Delta \eta_j} (\ell_{i+1,j+1}^m - \ell_{i+1,j-1}^m) \right]$$

$$D_j = \left( \frac{k\xi}{U_e} \right) \frac{\Delta \xi_i}{\Delta \tau_m} g_{i+1,j}^{m-1} + \xi (g_{i,j}^m)^2 + \Delta \xi_i (\beta_t + \beta_x)$$

where  $U_e$ ,  $\beta_x$  and  $\beta_t$  are evaluated at  $\xi = \xi_i$  and  $\tau = \tau_m$ .

### Continuity Equation

A straightforward central difference (at station  $j$ ) representation for  $\left( \frac{\partial h}{\partial \eta} \right)$  in Equation (70) would give  $h$  at odd or even points (in the  $j$  direction) but not both. This problem is taken care of by applying the central difference formula at station  $(j + \frac{1}{2})$  instead. Representing Equation (70) in finite difference form at station  $(i + \frac{1}{2})$ ,  $(j + \frac{1}{2})$  gives

$$h_{i+1,j+1}^m = \left( h_{i+1,j}^m - h_{i,j+1}^m + h_{i,j}^m \right) + \beta_t \Delta \eta_{j+1}$$

$$- \frac{1}{4} (\beta_x + 1) \Delta \eta_{j+1} (g_{i+1,j+1}^m + g_{i+1,j}^m + g_{i,j+1}^m + g_{i,j}^m)$$

$$- \xi \frac{\Delta \eta_{j+1}}{\Delta \xi_i} (g_{i+1,j+1}^m - g_{i,j+1}^m + g_{i+1,j}^m - g_{i,j}^m)$$

where  $\xi$ ,  $\beta_x$  and  $\beta_t$  are evaluated at station  $(i + \frac{1}{2})$  and  $\tau = \tau_m$ .

## APPENDIX B

## STAGNATION POINT FINITE DIFFERENCE EQUATIONS

This appendix contains the difference equations corresponding to Equations (77) and (76). The finite difference formulae used are given in Appendix A.

The following tridiagonal form is obtained for Equation (77)

$$A_j g_{j+1}^m + B_j g_j^m + C_j g_{j-1}^m = D_j \quad (j=2 \text{ to } N-1)$$

where  $j=1$  and  $j=N$  are the indices for the wall and the boundary layer edge, respectively. The coefficients  $A_j$ ,  $B_j$ ,  $C_j$  and  $D_j$  are given by

$$A_j = \frac{1}{2\Delta\eta} \left( h_j^m - \frac{1}{\Delta\eta} \right)$$

$$B_j = \frac{k}{A\Delta\tau_m} + \left( \beta_t \right)_o + g_j^m + \frac{1}{(\Delta\eta)^2}$$

$$C_j = - \frac{1}{2\Delta\eta} \left( h_j^m + \frac{1}{\Delta\eta} \right)$$

$$D_j = \frac{k}{A\Delta\tau_m} g_j^{m-1} + \left( \beta_t \right)_o + 1$$

where  $A$  and  $\left( \beta_t \right)_o$  are defined by Equations (74) and (75), respectively.

The continuity equation (76) with central difference at station

$(j + \frac{1}{2})$  gives

$$h_{j+1}^m = h_j^m + \Delta\eta \left[ \frac{1}{2} \left( \rho_t \right)_0 - g_j^m \right]$$

## REFERENCES

1. Ormiston, R. A., and Hodges, D. H., "Linear Flap-Lag Dynamics of Hingeless Helicopter Rotor Blades in Hover," Journal of the American Helicopter Society, Vol. 17, April 1972, pp. 2-14.
2. Friedmann, P., and Tong, P., "Dynamic Nonlinear Elastic Stability of Helicopter Rotor Blades in Hover and in Forward Flight," NASA CR-114485, May 1972; also MIT ASRL 166-3.
3. Hodges, D. H., and Ormiston, R. A., "Stability of Elastic Bending and Torsion of Uniform Cantilevered Rotor Blades in Hover," AIAA, ASME, SAE 14th Structures, Structural Dynamics and Materials Conference, AIAA Paper 73-405, March 1973.
4. Hodges, D. H., and Ormiston, R. A., "Stability of Elastic Bending and Torsion of Uniform Cantilever Rotor Blades in Hover with Variable Structural Coupling," NASA TN D-8192, April 1976.
5. Friedmann, P., "Influence of Modeling and Blade Parameters on the Aeroelastic Stability of a Cantilevered Rotor," AIAA Journal, Vol. 15, No. 2, February 1977, pp. 149-158.
6. Ormiston, R. A., "Comparison of Several Methods for Predicting Loads on a Hypothetical Helicopter Rotor," Presented at the AHS/NASA-Ames Specialists Meeting on Rotorcraft Dynamics, Moffett Field, California, February 1974.
7. Harris, F. D., Tarzanin, F. J., Jr., and Fisher, R. K., Jr., "Rotor High Speed Performance, Theory vs. Test," Journal of the American Helicopter Society, Vol. 15, No. 3, July 1970, pp. 35-44.
8. Jenkins, J. L., Jr., "A Numerical Method for Studying the Transient Blade Motions of Rotor with Flapping and Lead-lag Degrees of Freedom," NASA TN D-4195, October 1967.
9. Ormiston, R. A., and Bousman, W. G., "A Theoretical and Experimental Investigation of Flap-Lag Stability of Hingeless Helicopter Rotor Blades," NASA TM X-62179, August 1972.
10. Chou, P. C., "Pitch-Lag Instability of Helicopter Rotors," Journal of the American Helicopter Society, Vol. 3, No. 3, July 1958, pp. 30-39.
11. Ormiston, R. A., and Bousman, W. G., "A Study of Stall-Induced Flap-lag Instability of Hingeless Rotors," AHS Preprint No. 730, 29th Annual National Forum of the American Helicopter Society, Washington, D. C., May 1973.



12. Bellinger, E. D., "Analytical Investigation of the Effects of Blade Flexibility, Unsteady Aerodynamics, and Variable Inflow on Helicopter Rotor Stall Characteristics," NASA CR-1769, September 1971.
13. Philippe, J. J., and Sagner, M., "Calcul et Mesure des Forces Aerodynamiques sur un Profil Oscillant avec et sans Decrochage," AGARD Conference Proceedings No. 111 on Aerodynamics of Rotary Wings, Paper 11, September 1972.
14. Valensi, J., and Rebont, J., "Efforts Aerodynamiques sur un Profil D'Aile anime d'un Mouvement Harmonique Parallele a L'Ecoulement 'Mouvement de Tamis'," AGARD Conference Proceedings No. 111 on Aerodynamics of Rotary Wings, Paper 12, September 1972.
15. Kunz, D. L., "Unsteady Drag and Dynamic Stall as Simulated in a Varying Freestream," Ph.D. Thesis, Georgia Institute of Technology, Department of Aerospace Engineering, March 1976.
16. Isaacs, R., "Airfoil Theory for Flows with Variable Velocity," Journal of the Aeronautical Sciences, Vol. 12, No. 1, January 1945, pp. 113-117.
17. Isaacs, R., "Airfoil Theory for Rotary Wing Aircraft," Journal of the Aeronautical Sciences, Vol. 13, No. 4, April 1946, pp. 218-220.
18. Greenberg, J. M., "Airfoil in Sinusoidal Motion in a Pulsating Stream," NACA Technical Note No. 1326, June 1947.
19. Theodorsen, T., "General Theory of Aerodynamic Instability and the Mechanism of Flutter," NACA Report No. 496, 1935.
20. Randall, D. G., "Forces on Aerofoils with Both Incidence and Forward Speed Varying," ARC R&M 3414, 1965.
21. Robinson, A., and Laurmann, J. A., Wing Theory, Cambridge University Press, Cambridge, 1956.
22. Bisplinghoff, R. L., Ashley, H., and Halfman, R. L., Aeroelasticity, Addison-Wesley, Cambridge, Massachusetts, 1955.
23. Dwyer, H. A., "Calculation of Unsteady and Three-Dimensional Boundary Layer Flows," AIAA Journal, Vol. 11, No. 6, June 1973, pp. 773-774.
24. Dwyer, H. A., Doss, E. D., and Goldman, A. L., "A Computer Program for the Calculation of Laminar and Turbulent Boundary Layer Flows," NASA CR-114366, 1970.
25. Ames, W. F., Nonlinear Partial Differential Equations in Engineering, Academic Press, New York, 1965.

26. Cebeci, T., Smith, A. M. O., and Mosinkis, G., "Calculation of Compressible Adiabatic Turbulent Boundary Layers," AIAA Journal, Vol. 8, No. 11, November 1970, pp. 1974-1982.
27. Michel, R., "Determination of Transition Point and Calculation of Drag of Wing Sections in Incompressible Flow," ONERA Publication 58, 1952.
28. Lighthill, M. J., "The Response of Laminar Skin Friction and Heat Transfer to Fluctuations in the Stream Velocity," Proceedings of the Royal Society, Ser. A, Vol. 224, June 1954, pp. 1-23.
29. Nickerson, R. J., "The Effect of Free Stream Oscillations on the Laminar Boundary Layers on a Flat Plate," Sc.D. Thesis, Massachusetts Institute of Technology, Department of Mechanical Engineering, 1957.
30. McCroskey, W. J., and Philippe, J. J., "Unsteady Viscous Flow on Oscillating Airfoils," AIAA Journal, Vol. 13, No. 1, January 1975, pp. 71-79.
31. Hill, P. G., and Stenning, A. H., "Laminar Boundary Layers in Oscillatory Flow," ASME Transactions: Journal of Basic Engineering, Vol. 82, September 1960, pp. 593-608.
32. Lamb, H., Hydrodynamics, Dover Publications, New York, 1945.
33. Van Dyke, M. D., "Second Order Subsonic Airfoil Theory Including Edge Effects," NACA Report 1274, 1956.
34. Lighthill, M. J., "A New Approach to Thin Airfoil Theory," Aeronautical Quarterly, Vol. 3, November 1951, pp. 193-210.
35. Sneddon, I. N., Elements of Partial Differential Equations, McGraw-Hill Book Company, New York, 1957.
36. Karamcheti, K., Principles of Ideal-Fluid Aerodynamics, John Wiley and Sons, Inc., New York, 1966.
37. Carnahan, B., Luther, H. A., and Wilkes, J. O., Applied Numerical Methods, John Wiley & Sons, Inc., New York, 1969.
38. Schuh, H., "Calculation of Unsteady Boundary Layers in Two-dimensional Laminar Flow," Zeitschrift fur Flugwissenschaften, Vol. 1, 1953, pp. 122-131.
39. Rozin, L. A., "An Approximation Method for the Integration of the Equations of a Nonstationary Laminar Boundary Layer in an Incompressible Fluid," NASA Technical Translation 22 (1960).
40. Presz, W. M., and Heiser, W. H., "Unsteady Boundary Layer Analysis for Two-dimensional Laminar Flow," Zeitschrift fur Flugwissenschaften, Vol. 16, No. 2, February 1968, pp. 33-39.

41. McDonald, H., and Shamroth, S. J., "An Analysis and Application of the Time-Dependent Turbulent Boundary-Layer Equations," AIAA Journal, Vol. 9, No. 8, August 1971, pp. 1553-1560.
42. Crimi, P., and Reeves, B. L., "A Method for Analyzing Dynamic Stall of Helicopter Rotor Blades," NASA CR-2009, May 1972.
43. Scruggs, R. M., Nash, J. F., and Singleton, R. E., "Analysis of Dynamic Stall Using Unsteady Boundary Layer Theory," NASA CR-2462, October 1974.
44. Dwyer, H. A., and McCroskey, W. J., "Crossflow and Unsteady Boundary-Layer Effects on Rotating Blades," AIAA Journal, Vol. 9, No. 8, August 1971, pp. 1498-1505.
45. Schlichting, H., Boundary Layer Theory, 6th ed., McGraw-Hill Book Company, New York, 1968.
46. Cebeci, T., and Smith, A. M. O., Analysis of Turbulent Boundary Layers, Academic Press, New York, 1974.
47. Hairston, D. E., "Survey and Evaluation of Current Boundary Layer Transition Prediction Techniques," AIAA Paper 71-985, Washington, D. C., 1971.
48. Cebeci, T., and Smith, A. M. O., "Calculation of Profile Drag of Airfoils at Low Mach Numbers," Jour. of Aircraft, Vol. 5, No. 6, Nov. - Dec. 1968, pp. 536.
49. Rotta, J. C., "Turbulent Boundary Layers in Incompressible Flow," Progress in Aeronautical Sciences, Vol. 2, Pergamon Press, Oxford, 1962, pp. 1-219.
50. Goldstein, S., Modern Developments in Fluid Dynamics, Vol. 2, Dover Publications, Inc., New York, 1965.
51. Abbott, D. E., and Cebeci, T., "The General Analysis of Unsteady Boundary Layers-Laminar and Turbulent," Project SQUID Symposium on Fluid Dynamics of Unsteady, Three-Dimensional and Separated Flows, Atlanta, GA, June 1971.
52. Telionis, D. P., and Tsahalis, D. Th., "Unsteady Turbulent Boundary Layers and Separation," AIAA Journal, Vol. 14, No. 4, April 1976, pp. 468-474.
53. Windsor, R. I., "Measurement of Aerodynamic Forces on an Oscillating Airfoil," TR 69-98, March 1970, U.S. Army Aviation Material Lab., Ft. Eustis, VA.
54. Ashley, H., Moser, H. H., and Dugundji, J., "Investigation of Rotor Response to Vibratory Aerodynamic Inputs," Part III. "Three-Dimensional Effects on Unsteady Flow Through a Helicopter Rotor,"

U.S. Air Force, Air Research and Development Command, WADC TR 58-87, AD 203392, October 1958.

55. von Doenhoff, A. E., "Investigation of the Boundary Layer about a Symmetrical Airfoil in a Wind Tunnel of Low Turbulence," NACA Wartime Report L-507, 1940.
56. Newman, B. G., "Some Contributions to the Study of the Turbulent Boundary Layer Near Separation," Australian Department of Supply Report, ACA-53, 1951.

## VITA

Kottapalli Sesi Bhushan Rao was born on July 7, 1951 in Guntur, Andhra Pradesh, India and graduated from the Delhi Public School, New Delhi in 1967. He received the Bachelor of Technology degree in Aeronautical Engineering from the Indian Institute of Technology, Kanpur in 1972. In the fall of 1972 he joined the Georgia Institute of Technology, Atlanta as a graduate student and received the degree of Master of Science in Aerospace Engineering in December 1973.